Characterisation of photovoltaic devices using large area light beam induced current measurements

By

Michael OKULLO

Submitted in fulfilment of the requirements for the degree of

PHILOSOPHIAE DOCTOR

in the Faculty of Science

at the Nelson Mandela Metropolitan University

Promoter: Dr F.J. Vorster
Co-Promoter: Prof E.E. van Dyk
Co-Promoter: Dr W. Okullo

April 2017

Declaration

Full names: Michael Okullo

Student number: 214229785

Qualification: PHILOSOPHIAE DOCTOR

Thesis title: Characterisation of photovoltaic devices using large area light beam induced current measurements

In accordance with Rule G4.6.3, I hereby declare that the above-mentioned thesis is my own work and that it has not previously been submitted for assessment to another University or for another qualification.

Signature:.....

Date:.....

Dedication

This thesis is dedicated to my parents, Stephen Otim and Juspenina Otim for making my education a priority.

Acknowledgements

First and foremost I wish to express my gratitude to my promoters, Dr F. J. Vorster, Prof E. E. van Dyk and Dr W. Okullo for accepting to offer their time and technical knowledge to steer this research in the right direction. Their constructive criticism was a big motivation to me which kept me on my toes all the time.

I would like to thank Dr Betty Kibirige for accepting to lend me her PV modules from which I was able to get exciting results.

I am indebted to Mr Len Compton for the technical assistance that he was always willing to offer whenever I approached him.

I am deeply grateful to Ms Jualine Ferreira for her compassion, hospitality and always being more than willing to help when it comes to administrative issues.

I wish to thank Dr Jacqueline Crozier for helping with electroluminescence imaging, Dr Denis Okello for introducing me to Lyx, which I found very useful in writing my thesis, Dr Nicholas Kwarikunda for assistance in Labview and Mr Lucian Bezuidenhout for always making time for me whenever I had questions concerning Matlab. My friends, Valentine, Enoch, Duncan and Georgie, thank you for the moral support.

I am grateful to African Laser Centre (ALC) and Kyambogo University for the financial support rendered to me, which made it possible to pursue this PhD course.

Finally, I am grateful to my wife Margaret and my children Oscar, Frankie, Allan, Norman, Juliet and Louis for keeping the family intact during my absence.

Contents

List of Figures

List of Tables

Symbols and Abbreviations

a-Si	Amorphous silicon
ARC	Anti-reflective coating
CdTe	Cadmium Teluride
CIGS	Copper indium gallium diselenide
CIS	Copper indium diselenide
CPV	Concentrator photovoltaic
CREST	Centre for Renewable Energy Systems Technology
c-Si	Mono-crystalline silicon
EBIC	Electron beam induced current
EL	Electroluminescence
FF	Fill factor
I_m	Current at maximum power point
I_{ph}	Photo-generated current
I_{sc}	Short circuit current
I_{sh}	Shunt current
LA-LBIC	Large area light beam induced current
LBIC	Light beam induced current
li-LBIC	Limited light beam induced current
mc-Si	Multicrystalline silicon
MJ	Multi-junction
NREL	National Renewable Energy Laboratory
POE	Primary optical element
PV	Photovoltaic
PVPM	Photovoltaic power measurement
R_s	Series resistance
R_{sh}	Shunt resistance

S-LBIC Solar light beam induced current

SMU Source measurement unit

SOE Secondary optical element

STC Standard test condition

SWE Staebler Wronski Effect

TCO Transparent conducting oxide

V_m Voltage at maximum power point

V_{oc} Open circuit voltage

XBIC X-ray beam induced current

Abstract

Photovoltaic (PV) modules are made by connecting PV cells in series in order to generate a reasonable voltage that can be used for any productive work. Inaccuracy in cell sorting during crystalline silicon module construction, or non-uniform deposition of PV material and laser scribing during thin film module construction, may introduce current mismatch in the module. Current mismatch is a consequence of connecting module cells which have non-identical electrical characteristics. When current mismatch occurs in a module, it is the cell generating the lowest current that determines the module output current and this leads to a decrease in the output power and lifespan of the module. Investigation of current uniformity and the different current reducing features in PV modules, which are potential sources of current mismatch, is therefore critical in optimising the performance of PV modules.

In this study, a large area light beam induced current (LA-LBIC) measurement system was developed. This non-destructive technique was used to characterise crystalline silicon PV modules (mono-crystalline and multi-crystalline), thin film PV modules (amorphous silicon and copper indium diselenide) and a combined concentrator photovoltaic (CPV) module. A light source mounted onto a motorised x-y scanning stage was used to illuminate a PV module, or the Fresnel lens of a CPV module, point-by-point, while measuring the module output current. The measured current was mapped as a function of position and presented as an LBIC image.

The point-illuminated circuit model of a PV module was designed and used to explain the variation in current between and within module cells in the LA-LBIC maps. Application of the model to crystalline silicon modules attributes the variation in photo-generated current between cells mainly to current mismatch between series connected cells. Current variation within cells is attributed to individual cell shunts. In the thin film modules, the model attributes the variation in photo-generated current mainly to differences in local cell shunts and series resistances originating from the scribing procedure during cell formation in the manufacturing process.

In the PV modules studied, variation in photo-generated current was found to exist both between and within cells. The variation was more pronounced between cells than within cells. Module point I-V curves at different points of the module were measured in order to extract short circuit current, to quantify the variations between and within cells. A striation ring defect, causing a drop in short circuit current of 38%, was detected in the mono-crystalline module. Investigation of the striation ring defect indicated that the defect is active in the bulk (p-type) but inactive in the top (n-type) layer. Further characterisation

of the defect revealed that a higher percentage loss in short circuit current occurs at lower light intensities. In the multi-crystalline silicon module, cracks were detected and found to electrically isolate the module cells into two parts, causing them to operate in parallel and consequently introducing current mismatch in the module. The I-V curve of the module at standard test condition (STC) revealed a step below the knee, which is a manifestation of current mismatch in the module. High currents, as a consequence of diffuse reflection, leading to multiple reflections by the top glass were also observed at localised points on the bus bar and cell separations. In the a-Si module, the variation in photo-current within some cells, was found to be substantial. In the copper indium diselenide (CIS) module, an electrical disconnection across the module cells was identified. A disconnection in the form of a triangular shape was also identified in this module, which completely disconnected the front contact of this area from the module. This unique disconnection feature caused current in the module to flow in a reverse direction when the light spot was incident within the boundary of the disconnection. Scans performed under different forward voltage biases were useful in identifying severely shunted module cells. A severely shunted cell was found to generate a higher photo-current than a good cell at the same forward bias voltage. This unique observation was explored further using point-illuminated module I-V measurements, and was found to be due to the crossing over of the I-V curves of the two cells.

In order to explore the relationship between cell photo-current and cell shunt resistance, a method to determine the shunt resistances of the cells in an encapsulated module was devised. The method involves measuring the I-V curves of a fully illuminated module and a partially illuminated module when one of its cells is shaded and the I-V curves used to determine the short circuit current and the shunt resistance of the shaded cell. A strong correlation was found to exist between the short circuit current of the shaded cell and the cell shunt resistance, as well as between the short circuit current of the shaded cell and dark LBIC.

The LA-LBIC technique was further applied to characterise a combine CPV module. Results showed that the Fresnel lens facets close to the centre generate a higher photo-current at the receiver than those towards the edges. The reduced photo-current towards the edges was attributed to losses due to diffraction, dielectric reflection and internal reflection. About 65% of the area of the Fresnel lenses were found to be effective in light collection in terms of the photo-current generated at the receiver. Abrasions and scratches on the Fresnel lenses were identified as some of the current limiting features in a CPV module.

The LA-LBIC technique used in this study has demonstrated the potential to investigate current mismatch, current limiting and current enhancing features in PV modules. The

capacity to further characterise current limiting features in order to investigate their effects on photo-current under different wavelengths and light intensities was also demonstrated. Extending the LA-LBIC technique to characterise a combined CPV module is a great achievement of this work.

Chapter 1

Introduction

1.1 Background

The provision of appropriate/usable energy is crucial to economic development of any country. The world's energy requirement is continually growing in response to the growing human population. The world population is predicted to increase from 7.3 billion in 2015 to 8.5 billion in 2030 [1]. This predicted increase in population will cause a substantial increase in energy demand, especially in developing countries. There is therefore a great need to increase the world's energy supply to address this issue. Fossil fuels, which are the major traditional sources of energy, are at risk of being depleted, and have unfriendly environmental effects arising from carbon dioxide emissions. Renewable energy resources are seen as better substitutes for unsustainable fossil fuels. The renewable energy share of the global electricity generation is expected to reach 26% in the year 2020, from 22% in 2012 [2]. Solar energy is the largest exploitable resource compared to other renewable energy sources and solar insolation on the earth's surface per hour is more than the energy consumed by all human activities in one year [3]. Due to its abundance and environmental friendliness, solar energy utilisation in electricity generation is becoming increasingly important.

Solar energy can be harvested using photovoltaic (PV) modules which consist of individual photovoltaic cells connected in series to produce a higher voltage. Photovoltaic cells are capable of generating current when photons of sufficient energy are incident on them. The PV share of global electricity production is expected to reach 16% in 2050, from 11% in 2010 [4]. Research to increase the efficiency of PV cells and reduce the cost of modules is being carried out so that PV technology remains competitive. The cost of PV modules has continued to drop and the number of those who can afford to purchase PV modules has

maintained a rising trend. The cost of PV modules has reduced by 80% in the last six years in most markets, while the cost of full PV systems has been reduced by almost 30% [4].

Photovoltaic module performance is affected by inhomogeneity in the photo-response of the constituting cells. For optimum module performance, the module should be made up of cells which have identical electrical characteristics. This is important because it enables the module to operate as a homogeneous device, free of current mismatch, which lowers the module performance and lifespan. Current mismatch occurs when the PV cells in a module generate different currents [5] and in such a circumstance the module output current is determined by the cell with the lowest photo-response [6]. Current mismatch in a module is caused by mismatch in the resistances of the series-connected cells. Semiconductor materials used to make PV cells may contain defects [7] which lower the cell performance and subsequently the module performance. Performance limiting defects may also occur during the production process [8, 9, 10] or after production [11]. Investigation of homogeneity in photo-current and current limiting features in PV modules using a non-destructive technique is required in order to evaluate and monitor the quality of modules over time. Quality assurance and monitoring of PV modules are critical to ensure that the modules perform as expected and live up to the predicted lifespan.

In this study, a large area light beam induced current (LA-LBIC) measurement system was developed and used to characterise PV modules and a combined concentrator photovoltaic (CPV) module. In the investigation, a PV module and the Fresnel lens of a CPV module, is scanned point-by-point with a light spot, and the photo-generated current at each point is measured. By mapping the photo-current as a function of position, the photo-response map of the device can be obtained. The photo-response map reveals the level of homogeneity of the photo-current and identifies current limiting features in the device, which is vital information that can be used by manufacturers to identify gaps in the manufacturing process and devise new strategies for improvement. Due to its non-destructive nature, the technique can be used to investigate a PV device, re-deploy it and perform a similar investigation after a period of time, in order to determine performance changes that occur in the device over time. Since the major loss to photo-generated current in PV modules is the shunt leakage path, a method to determine the shunt resistance of individual cells in a PV module was devised. The method involves measuring the current-voltage (I-V) characteristics of a fully illuminated module, and then determining the I-V curves with each cell shaded. The resulting I-V curves are then used to determine the shunt resistance of the shaded cell.

1.2 General objective

The main objective of the study was to characterise photovoltaic devices using large area light beam induced current measurements.

1.2.1 Specific objectives

1. To investigate homogeneity in photo-current and current limiting features in PV modules using LA-LBIC mapping.
2. To study the effect of changing bias voltage, light wavelength and intensity on the photo-current generated by the different module cells and at the current limiting features.
3. To determine the shunt resistance of module cells by using the method of individual cell shading.
4. To characterise a combined concentrator photovoltaic module using LA-LBIC mapping technique.

1.3 Significance of the study

With the PV market undergoing a period of rapid growth with many different technologies competing for the market share, characterisation of photovoltaic modules from different technologies becomes crucial. The use of LA-LBIC mapping technique to characterise PV modules provides a deeper understanding of the different current limiting and current enhancing features and their effects on the performance of the modules. By using the technique, where the entire module is illuminated while each cell is shaded one at a time, the shunt resistances of the module cells can be determined. Knowledge of the different current limiting features and their origin, provides valuable information to both the manufacturers and users of PV modules, where the manufacturers can improve on their production process while the users can protect their modules from current limiting features which develop after the production process.

1.4 Content outline

The content of this work is organised as outlined below:

Chapter 2: The historical background of LBIC and LA-LBIC, including the improvements that have been made on them over time, are reviewed. The LBIC principle, showing how current is generated in a point-illuminated PV module, is illustrated. The different LBIC losses which occur during PV module scanning are discussed. The single and the double diode models of solar cells are presented and are used to design an equivalent circuit model of a point-illuminated PV module. The equivalent circuit model of a point-illuminated PV module is useful in explaining the variations in photo-current that occur in the LA-LBIC maps. The I-V characteristics of a point-illuminated and a partially illuminated PV module are presented and discussed by use of equivalent circuit models. The effect of applying a constant forward bias voltage to a PV module during scanning is also discussed.

Chapter 3: This chapter gives a brief introduction to the PV module technologies investigated in this study. The manufacturing processes for mono-crystalline silicon and multi-crystalline silicon solar cells are reviewed and the defects arising mainly through the manufacturing process are discussed. The structure of thin film solar cells and the module manufacturing process for monolithically integrated modules are presented. The current status of selected thin film technology, namely a-Si and CI(G)S solar cells and modules, in terms of their efficiencies and annual production, are reviewed.

Chapter 4: This chapter describes how the LA-LBIC measurement system was developed. The different system components and the role played by each of them are explained. The set-up for scanning PV modules is presented, and a description of how the system is used to take measurements is given.

Chapter 5: Other techniques used for PV module characterisation, more specifically I-V characterisation and electroluminescence (EL) are reviewed. The use of more than one method for PV module investigation provides more reliable results, as a feature which may not be observed when using one method, can be visible when another method is used, or may be unclear in one but more prominent in the other. The theory of I-V characterisation is reviewed and the I-V curve measurement using photovoltaic power measurement (PVPM) device is described. The EL imaging principle is reviewed and the measurement procedure is described.

Chapter 6: Results for PV modules of different technologies are presented and discussed. Crystalline silicon PV modules, namely c-Si and mc-Si, and thin film PV modules, namely a-Si and CIS, are considered. The results focus on LA-LBIC scans to map the performance distribution in the modules. Scans are also performed at various constant forward bias voltages to study changes in the photo-response of the module cells under different bias conditions. A striation ring feature is characterised and the performance of different module

cells under different light wavelengths and intensities are presented and discussed. Module point I-V measurements are performed to quantify the short circuit current at different points on the module. Module I-V characterisation and electroluminescence imaging results are also presented and discussed in relation to the LA-LBIC results to establish if they correlate in the identification of current limiting features in PV modules. Finally, a technique to measure the shunt resistances of cells in a PV module, that involves single cell shading, is presented.

Chapter 7: An introduction to CPV module technology, and the current efficiencies for both cells and modules, are given. The design and working principles of the CPV system are described. The different optical losses that occur in Fresnel lenses are also discussed. The LA-LBIC set-up used to investigate a combined CPV module is described. Results for optical performance mapping of a combined CPV module are presented and discussed.

Chapter 8: Conclusions are made based on the results obtained during this study. The challenges involved in the use of the LA-LBIC measurement technique are presented. A proposal for future work is made in view of addressing the challenges encountered, as well as extending the use of the LA-LBIC measurement system beyond the scope for which it has been used in this particular research work.

Chapter 2

Theory of light beam induced current (LBIC) measurements in photovoltaic devices

2.1 Brief historical background of LBIC and LA-LBIC

Several improvements have been made to the LBIC system hardware components as well as to the data collection techniques (biasing, reducing spot size, applying limiting condition), to enable it be used extensively for solar cell characterisation [12, 13, 6]. The LBIC system has remained a valuable non-destructive, performance analysis tool in the PV field. Several different excitation sources have been used to generate current in PV cells. These excitation sources are light, electrons and X-rays, hence the name LBIC, EBIC and XBIC respectively.

Research using the LBIC technique for solar cell material analysis began in the 1980s. In 1980, a laser scanning instrument for solar cells was developed by Plunkett [14]. This system consisted of two mirror galvanometers arranged to scan in orthogonal directions. The mirror galvanometers were used to focus the laser beam on the solar cell by a focusing lens. The moving light spot was then scanned on the PV device and the photo-generated current as a function of the spot position could be displayed in several modes. In the same year, Sawyer introduced the technique of forward biasing the cell by using either a steady-state light source or an external current during scanning [12]. In his system, two lasers whose beams were guided to the PV cell by vertical and horizontal deflection mirrors, were used. A sliding mirror was used to choose the laser output to be used with the scanner. By scanning the laser spot on the cell, the resultant photo-response could be amplified and displayed on the

screen of a cathode ray tube. The technique was able to detect cracks and areas of poor metallisation.

In 1996, Ribes [15] developed a confocal scanning beam Macroscope/Microscope, capable of imaging specimens up to 7 cm x 7 cm in area using reflected light, photoluminescence and optical beam induced current (OBIC). The Macroscope could focus the light spot diameter to 10 µm at various wavelengths and when used together with the conventional confocal scanning laser microscope, the spot diameter could be reduced to the sub-micron level. LBIC designs advanced with the introduction of stepper motors and potential/current source meters. In 2000, Hiltner introduced a high resolution and a high sensitivity laser LBIC system for the characterisation of grain boundaries and defects in polycrystalline solar cells [13]. The system had a spatial resolution of 1 µm and could therefore be used to probe single grains in polycrystalline solar cell materials, since grain sizes vary from about 1 µm to 10 µm. With the integration of a computer-controlled fibre-based attenuator, the intensity of the scanning laser could be varied.

In 2003, an advanced LBIC measurement system was developed by Carstensen [16]. This system used an infrared laser for scanning while a potentiostat or galvanostat was used to set the voltage or current of the solar cell. Halogen lamps were used to provide background light biasing in the system during scanning. The system could allow for measurements of the cell's local parameters, especially the local series and shunt resistances and could also identify material- and process-induced defects. The use of concentrated solar light for point-by-point scanning of solar cells was introduced in 2007 by Vorster [17]. This system was referred to as solar LBIC (S-LBIC) and was able to scan a cell area of 6.2 mm x 6.2 mm in 42 minutes. The cell could be dynamically biased between reverse to beyond the open circuit voltage during scanning. This technique gave the opportunity to study a PV cell's bias dependent defects under concentrated solar illumination. The use of LBIC for PV cell characterisation has been widely reported [18, 19, 20, 21, 22, 23, 24, 25]. However, cells are built up into PV modules and the extension of the LBIC system to accommodate module characterisation, commonly referred to as LA-LBIC, is required.

A large-scale laser scanner used to scan both PV cells and large modules was developed at the National Renewable Energy Laboratory (NREL) in 1994 by Matson [26]. The system was used to scan device areas of 1 cm^2 – 4 m^2 using spot resolutions of 50 µm to 1 mm. Computer controlled scanning mirrors were used to scan the laser spot on the device under investigation, while current measurements were taken using a computer. Light and voltage bias could also be applied to the device during the scanning process. In 2004, the large area laser scanning system (CREST LBIC) was developed at the Centre for Renewable Energy

Systems Technology (CREST) by Michel [27]. The scanning laser was guided on the cell under investigation by SCANgine 14 (deflecting mirror) and varioSCAN 20 (focusing system), and measurements were performed using a lock-in amplifier. Background illumination in the system was provided by a set of halogen lamps. Scans could be performed on module areas up to 1.2 m x 1.2 m. The CREST LBIC system was upgraded in 2011 to a limited laser beam induced current (li-LBIC) system by Vorasayan [6].

2.2 The LBIC principle

The LBIC measurement technique involves scanning a beam of light across a semiconductor and the photo-generated current flowing in the external circuit is measured. When the illumination point is within several minority carrier diffusion lengths of the pn junction, photo-current is generated, while illumination at a point further than several minority carrier diffusion lengths leads to no photo-current, as the excess carriers merely diffuse and eventually recombine [28]. The distribution of minority charge carriers generated at the laser spot is described by the continuity equation [29]:

$$D_p \Delta p(r) - \frac{1}{\tau} p(r) = -g(r) \tag{2.1}$$

where D_p is the minority carrier diffusion constant, $p(r)$ is the minority carrier density at point r, τ is the minority carrier lifetime and $g(r)$ is the volume generation function.

The description is based on the assumption that generation and recombination of charge carriers in the emitter and depletion region are negligible. With light absorption following an exponential law, Donolato [30] expresses the generation rate as:

$$g(z) = \phi_o \alpha exp(-\alpha z) \tag{2.2}$$

where ϕ_o is the number of incident photons per s.cm^2 and α is the absorption coefficient of light in the semiconductor material.

The generated minority carriers migrate by diffusion process to the junction and the drift effect of the built-in electric field helps to collect them. The collected current at a depth z is given by [30]:

$$I_0 = \int_0^\infty g(z) exp(-z/L) dz \tag{2.3}$$

where $L = (D\tau)^{\frac{1}{2}}$ is the diffusion length of the minority charge carriers.

When a photovoltaic (PV) cell or module has a shunt, part of the photo-generated current gets lost to the shunt, hence, the measured current at the cell or module output (I_{LBIC}) is lower than the photo-generated current. Shunts usually develop during the manufacturing process or field exposure of PV modules and they are responsible for the loss in module efficiency [31]. The effect of the shunt resistance, R_{sh}, on the photo-generated current depends strongly on the incident beam position. The closer the beam is to the shunt, the higher the shunt loss and the further the beam is from the shunt, the smaller the effect the shunt has on the photo-generated current [32], I_{ph}. Figure 2.1 shows how part of the photo-generated current is lost to a shunt, leading to a reduced I_{LBIC} at the module output.

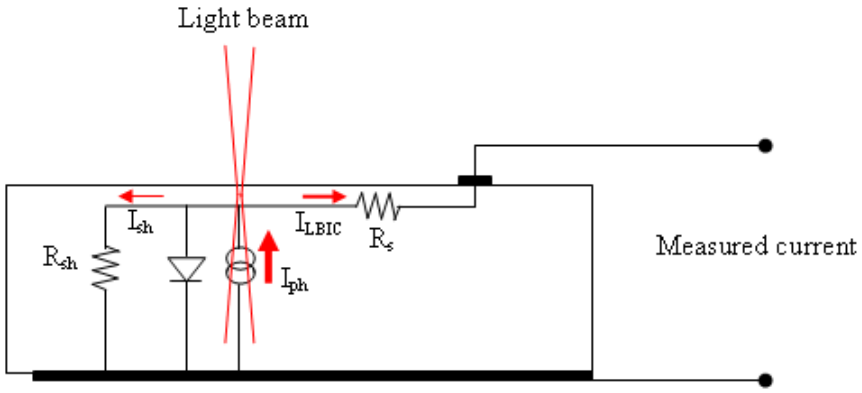

Figure 2.1: Equivalent circuit of local photo-current generation in the vicinity of a shunt in a solar cell [32].

The shunt and series resistances (R_{sh} and R_s), are in parallel and their effective resistance, R_{eff}, is given by:

$$R_{eff} = \left[\frac{R_s R_{sh}}{R_s + R_{sh}}\right] \tag{2.4}$$

The total voltage (V_T) across the two resistances is therefore:

$$V_T = I_{ph}\left[\frac{R_s R_{sh}}{R_s + R_{sh}}\right] \tag{2.5}$$

where I_{ph} is the photo-generated current.

Applying Ohm's law:

$$I_{sh} = I_{ph}\left[\frac{R_s}{R_s + R_{sh}}\right], \tag{2.6}$$

and

$$I_{LBIC} = I_{ph}\left[\frac{R_{sh}}{R_s + R_{sh}}\right] \tag{2.7}$$

It can be seen from equation 2.7 that when R_{sh} is high, the term in the square bracket tends to 1, and $I_{LBIC} \rightarrow I_{ph}$. However, when R_{sh} is low, R_s becomes significant and the term in the square bracket becomes less than 1 and I_{ph} is reduced further, leading to a low I_{LBIC}.

The LBIC contrast around a parasitic shunt in the photo-response map therefore appears different from the other parts of the cell or module which are free of shunts. The LBIC contrast, C, at any point is determined by the short circuit current at the defect, I_{def}, and the short circuit current at the region free of defects, I_{sc}, from the expression [20]:

$$C = \frac{I_{sc} - I_{def}}{I_{sc}} \tag{2.8}$$

When the LBIC investigation is applied to modules, the photo-generated current has to flow through the rest of the module cells before being measured at the module output and this complicates interpretation of LBIC data.

The series connection of cells in a module dictates that equal current flows through the module cells and therefore the cells in the dark are forced to operate in the reverse bias region, to allow more current flow through them and consequently forcing the cell being scanned into forward bias, so that less current flows through it. The voltage shifts vary from cell to cell, depending on the effective series resistances of the cells in the dark, which majorly come from their shunt resistances, forming the current path. When the scan points are restricted within a cell, the effect of the non-illuminated cells remain constant and variation in current within the same cell can therefore be reliably compared. For cell to cell investigation, these non uniform shifts in voltage during scanning make it difficult to accurately quantify the current generated by the different module cells, as it is not possible to control the operating voltage of the cell being scanned. However, by changing the pre-set module bias voltage between scans and comparing the LBIC signals between cells, valuable insight may be gained regarding the operating point of scanned cells, as well as the origin of LBIC features. Figure 2.2 shows the I-V curves of three series-connected module cells, illustrating how the voltages of the module cells shift to allow the same current to flow through the cells during module scanning. When the module cells have identical electrical properties, the shifts in voltage of all the illuminated cells remain constant. However, when the cells have non-identical electrical properties, the voltage shifts vary from cell to cell. It should, however, be noted that the overall dark I-V

curve remains unchanged, although the operating point keeps changing during scanning from cell to cell. Despite the shifts in individual cell voltages, the module voltage, V_{mod}, remains constant and equals the sum of individual operating cell voltages:

$$V_{mod} = V_1 + V_2 + V_3 \tag{2.9}$$

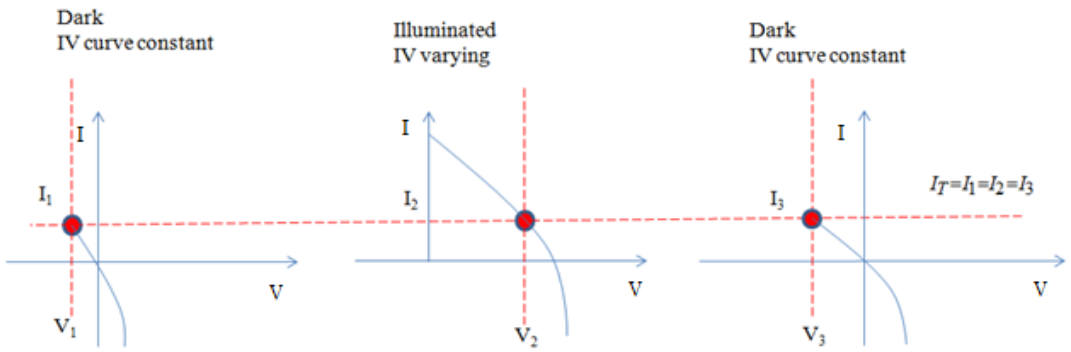

Figure 2.2: Voltage shifts of module cells during scanning.

External factors, particularly those inherent in the light source used, like the type, power and wavelength, also affect the magnitude of the light beam induced current.

A white light source contains different light wavelengths and can therefore excite electrons in various depths of the cell material, leading to the generation of a large number of charge carriers and hence a high photo-current. Laser light, on the other hand, is monochromatic and photo-current generation is hence restricted to a particular depth of the cell material.

The power of the light source used to illuminate a PV cell also determines the magnitude of the photo-current. When the power of the light source is high, more photons are produced and hence more charge carriers are released.

The wavelength of the light source used to illuminate a PV cell determines the depth of the cell to which the electrons are to be excited. For short wavelength light, electrons are generated close to the top surface and many electrons may not escape surface recombination, leading to a reduction in photo-current. Electrons generated far away from the junction have a long way to move to reach the junction, hence they may recombine before collection. Similarly, electrons generated close to the rear surface may suffer rear surface recombination and bulk recombination, as they have to move a long way to the junction before collection. However, charges generated at or close to the junction, have a high collection probability.

2.3 LBIC losses during PV module scanning

The energy of the incident photons is never wholly converted into current in photovoltaic cells or modules, due to losses inherent in the device. These losses can be categorised as optical losses, resistive losses and recombination losses.

2.3.1 Optical losses

Reflection can occur from the surface of the cell material, but this is usually mitigated by the use of an anti-reflective coating (ARC). In CIGS solar cell, reflection losses were reduced from 9.2% to 1.9% using ARCs [33]. When reflection of the light incident on a PV cell or module occurs, photons are reflected rather than absorbed, leading to a low photo-generated current. Contact fingers and bus bars, especially in crystalline silicon solar cells, are also major contributors to optical losses, as these reflect or block the incident light from reaching the cell material. Contact fingers cover about 7% of the total area of the cell [34]. Optical blockages may also result from inclusion during the manufacturing process, or even from opaque objects on the surface of the module. Optical blockages can be easily identified from their characteristic sharp edge definition in LBIC maps [18].

2.3.2 Resistive losses

The dissipation of power in the PV cell resistances reduces the cell efficiency. The cell series resistance arises from the resistances of the emitter and base of the cell, resistance of the contact between metal and silicon and the resistance of the top, rear metal contacts and fingers. The power loss from the series resistance caused by cell-to-module interconnection of 156 mm x 156 mm of crystalline silicon solar cells has been computed using the equation [35]:

$$P_{loss,itc} = I_m^2 \times R_{s,itc} \tag{2.10}$$

where $P_{loss,ict}$ is the power loss in module due to module interconnection, I_m is the current at maximum power point (MPP) and $R_{s,itc}$ is the series resistance from module interconnection and is given by:

$$R_{s,itc} = l \times \left[R_{s,string} + \frac{m}{n} \left(R_{s,contact} + R_{s,tab} \right) \right] \tag{2.11}$$

where $R_{s,string}$ is the series resistance due to the string interconnect, $R_{s,contact}$ is the series resistance of the contact between the cell and the tab, $R_{s,tab}$ is the resistance due to the cell interconnect ribbons, l is the number of strings in the module, m is the number of cells per string and n the number of bus bars per cell. Figure 2.3 shows a circuit model of the different series resistances in one string of a PV module consisting of two solar cells, with three bus bars. Interconnect ribbons are used to connect the front side of the solar cell with the rear side of the adjacent cell. Strings of solar cells are then connected together using the string interconnects.

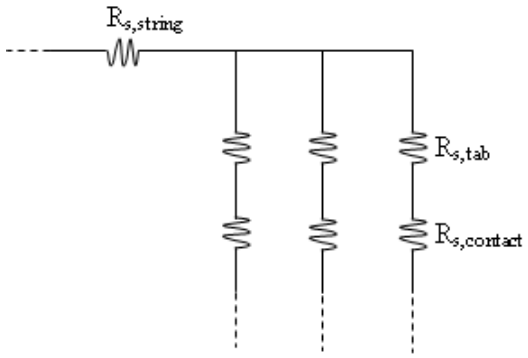

Figure 2.3: Equivalent circuit model of the various series resistances in a single string of a PV module consisting of two solar cells, with three busbars [35].

2.3.3 Recombination losses

When the charge carriers in a PV cell are generated in the vicinity of a recombination centre such as a defect or grain boundary, charges recombine [36]. Recombination of charge carriers lowers the short circuit current and also leads to a reduction in open circuit voltage [37]. Recombination is named according to the region of the cell where it occurs, namely surface recombination, bulk recombination and depletion layer recombination. The surface of a PV cell acts like a defect due to the disruption of the crystal lattice, therefore facilitating recombination. Bulk recombination dominates in the bulk of the PV cell where defects and impurities act as traps for charge carriers. The electric field in the depletion region helps to quickly separate the charges once they are produced and this makes recombination in this region less common.

2.4 Diode models of a solar cell and point-illuminated PV module

In this section, the single and the double diode models of a solar cell are presented and discussed. The single diode model is then used to construct the equivalent circuit model of a point-illuminated PV module.

An ideal solar cell is modeled as a large area diode in parallel with a current source. In practice, however, solar cell materials and the manufacturing process introduce current loss mechanisms which are accounted for by including a series resistance, R_s, and a parallel resistance, R_{sh}, in the ideal solar cell model. This model is referred to as the single diode model and is shown in Figure 2.4. The series resistance results from the metal contacts and resistance in the semiconductor material layers, fingers and bus bars, parallel resistance originates from defects in the semiconductor material [38].

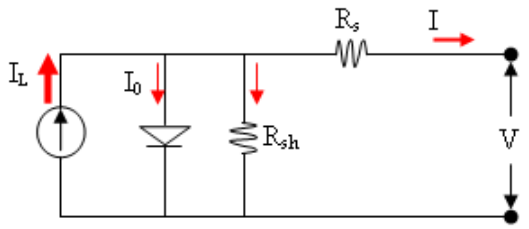

Figure 2.4: Single diode model of a PV cell.

The mathematical description of the I-V characteristics of the single diode model is given by the equation 2.12 [39]:

$$I = I_L - I_0 \left[exp\left(\frac{q(V + IR_s)}{nkT} \right) - 1 \right] - \frac{(V + IR_s)}{R_{sh}} \tag{2.12}$$

where I_L is the current generated by light, I_0 is the dark saturation current of the diode, q is the elementary charge, n is the diode ideality factor, T is the temperature of the pn junction, k is the Boltzmann constant and V is the applied voltage.

The single diode model is based on the assumption that the value of the ideality factor n remains constant. The ideality factor of the device, however, is voltage dependent and varies from 1 to 2. Surface and bulk recombination become dominant at higher voltages and the ideality factor tends to 1, while at lower voltages the ideality factor approaches 2, when junction recombination dominates. In order to model junction recombination, an additional diode is added in parallel to the first one, as shown in Figure 2.5, where D1

and D2 represent the recombination currents in the quasi-neutral and space charge regions, respectively [40, 41]. The two diode model has been reported to be superior to the single diode model, especially when subjected to irradiance and temperature variations [42].

The I-V characteristics of the two diode model can be described by the equation 2.13:

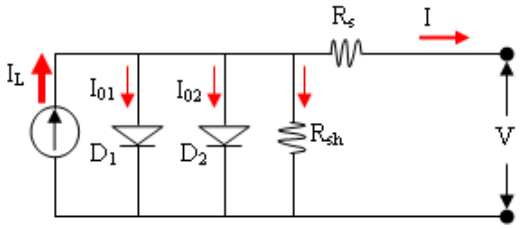

Figure 2.5: Double diode model of a PV cell.

$$I = I_L - I_{01}\left[exp\left(\frac{q(V+IR_s)}{n_1 kT}\right) - 1\right] - I_{02}\left[exp\left(\frac{q(V+IR_s)}{n_2 kT}\right) - 1\right] - \frac{(V+IR_s)}{R_{sh}} \quad (2.13)$$

The voltage generated by a photovoltaic cell, which is dependent on the band gap of the cell material, is usually small and cannot be utilised for any productive work. To generate a higher voltage, the cells are connected in series to form a PV module. It is required that the cells used for module construction should have identical electrical characteristics so that the module does not experience current mismatch, which has a negative impact on module performance.

In the LBIC investigation of modules, only a tiny part of the module is illuminated while the rest is kept in the dark, as shown in the equivalent circuit model in Figure 2.6.

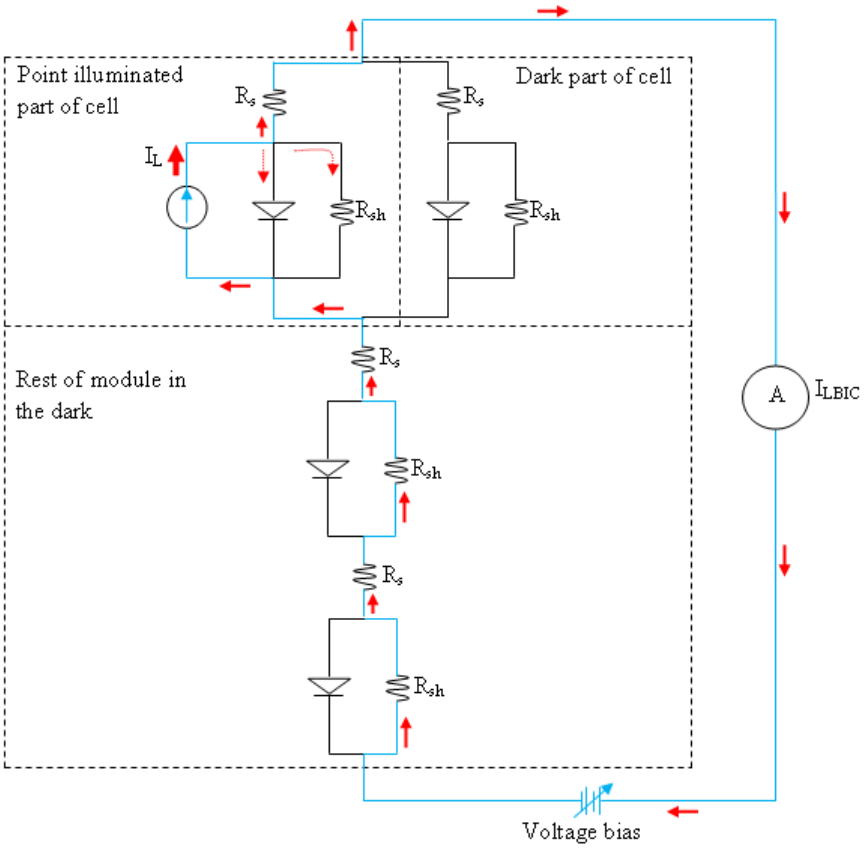

Figure 2.6: Equivalent circuit model of a point illuminated PV module.

The blue line shows the path of photo-generated current, I_L, in the module. Part of I_L is lost to the shunt resistance of the illuminated cell, R_{sh}, while the rest flows through the shunt and series resistances of the non-illuminated cells as shown in Figure 2.6.

When a module cell is spot-illuminated, the shunt resistance of the illuminated portion of the cell gets activated as a leakage path, while that of the portion in the dark, including the rest of the module cells in the dark are activated as series resistance. When the shunt resistances of the non-illuminated cells becomes active series resistances, the resistance along the current path as illustrated in Figure 2.6, is greatly increased and as a consequence, the measured I_{LBIC} is less than the photo-generated current I_L. The current generated as a result of the point-illumination has to flow through the cell where it is generated and then to all the other cells in the module before it exits the module output terminal. If the illuminated cell has a weak diode, or is shunted, then this reduces the photo-generated current, as shown in Figure 2.6. A weak diode creates a leakage path whose effect covers a large area of the solar cell [18].

The current flowing from the neighbouring cell into the spot-illuminated cell, takes the path

of least resistance, which is the illuminated path as shown in Figure 2.6. Since the resistances of the two paths are in parallel, the current will divide as shown by equations 2.6 and 2.7. When the illumination spot size is as big as the cell, the cell shunt resistance is fully activated and all the current takes the illuminated path. However, when the non-illuminated portion of the cell increases as the illumination spot size is reduced, the current through the dark path of the cell increases and reaches a maximum when the entire cell is in darkness.

The current flowing through the non-illuminated cells has no option but to flow through the cells' shunt resistances, thereby encountering high voltage drops due to the high values of the shunt resistances. The drop in photo-generated current during LBIC scanning arises from the effective shunt resistance of the cells in the dark. If the cell being scanned has a relatively high shunt resistance, the voltage drop arising from the shunt resistance of the remaining cells in the dark will be low, hence a high LBIC signal. Similarly, if the spot-illuminated cell has a low shunt resistance compared to the shunt resistances of the rest of the module cells, a high voltage drop occurs across the dark cells, leading to a low LBIC signal. The variation in LBIC signal from cell to cell is therefore mainly a result of these differences in shunt resistances [43, 44]. Therefore, the LBIC signals of the cells in a module can be used to compare the shunt resistances of the module cells.

2.5 Current-voltage characteristics of point-illuminated and partially shaded PV modules

I-V characteristics graphically represent how a solar cell or module operates and shows how the current relates to voltage under specified conditions of irradiance and temperature. Performance parameters such as open circuit voltage, short circuit current, maximum power current, maximum power voltage, series resistance and shunt resistance can be extracted from the I-V curve. Figure 2.7 shows a typical I-V curve of a fully illuminated PV module.

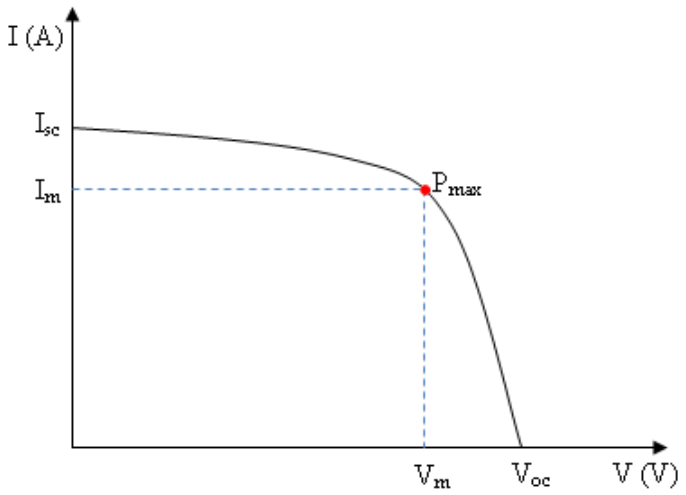

Figure 2.7: Typical I-V curve of a real PV module.

I_{sc} is the current at 0 V bias, V_{oc} is the voltage when no current flows through the module, I_m and V_m are the maximum current and voltage at maximum power point, P_{max}, respectively.

2.5.1 I-V curve of a point-illuminated PV module

The flow of current in a point-illuminated PV module is illustrated in Figure 2.8(a), while Figure 2.8(b) shows how current flows in a fully illuminated PV module. The blue line shows the current path in the module.

When the module is point-illuminated the current generated at the laser spot has to flow through the non-illuminated cells of the module.

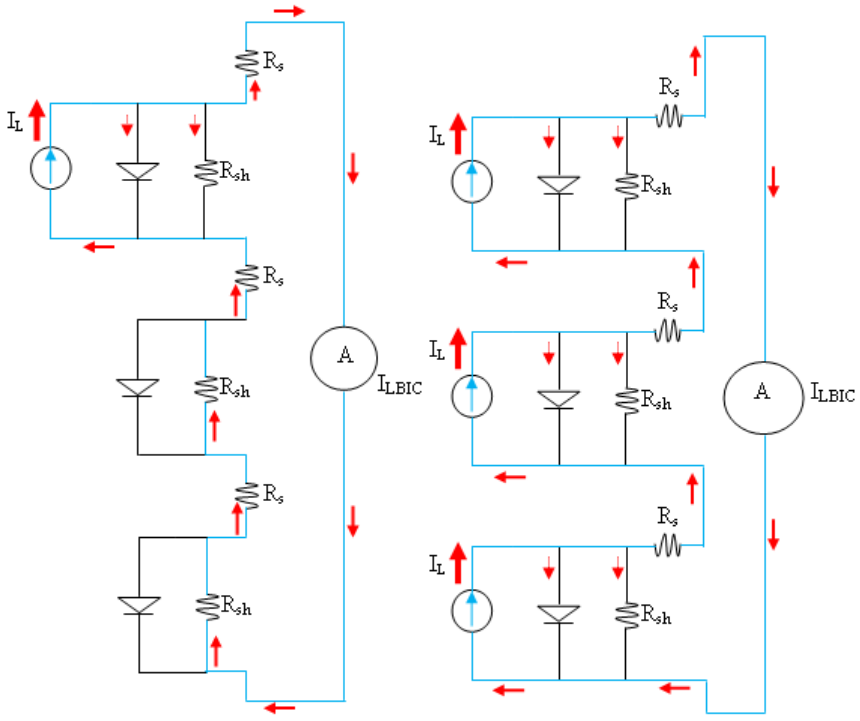

(a) Point illumination. **(b)** Full illumination.

Figure 2.8: Flow of current in a PV module under light illumination.

It can be seen that the shunt resistances of the non-illuminated cells add to the resistance along the current path, thereby leading to a tremendous increase in the module series resistance. The high series resistance developed in the current path leads to a large voltage drop that greatly reduces the photo-generated current. The response of the module I-V curve to this reduction in current is a decrease in the slope at V_{oc}. Figure 2.9(a) shows a typical point-illuminated module I-V curve of a copper indium diselenide module consisting of 34 cells, under a bias voltage range of -3 V to 4 V. Figure 2.9(b) is a magnified view of the region indicated by green dotted lines in Figure 2.9(a), highlighting the linear shape of the IV curve in the first quadrant.

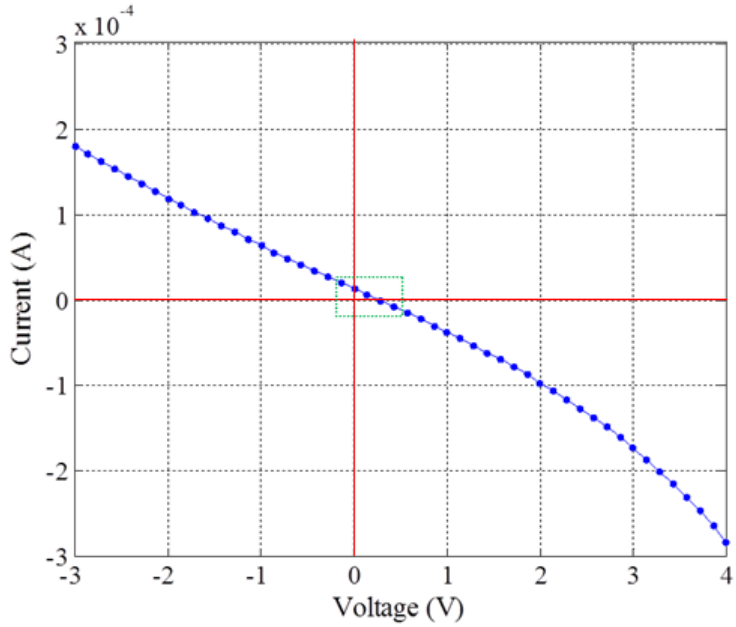

(a)

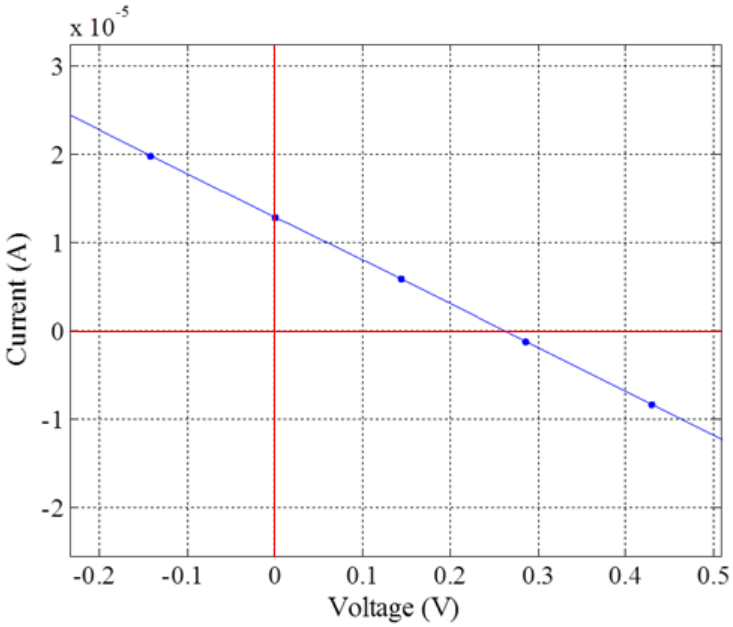

(b)

Figure 2.9: Point-illuminated module I-V curve of a CIS module at a bias of (a) -3V to 4V (b) -0.2 V to 0.5 V, obtained by magnifying the region indicated by green dotted lines in (a).

In Figure 2.10, the black and the red curves represent the ideal and the real I-V curves of a PV module. Changes in the parasitic resistances of a module result in distortion of the shape of the I-V curve. When the module's series resistance increases, the slope at V_{oc} reduces

as shown in Figure 2.10(a), and a decrease in the module's shunt resistance increases the slope at I_{sc}, as shown in Figure 2.10(b). In the case of point-illumination, the dark part of the module leads to a substantial increase in series resistance and hence the part of the I-V curve in the first quadrant changes from exponential to almost linear, as seen in Figure 2.9.

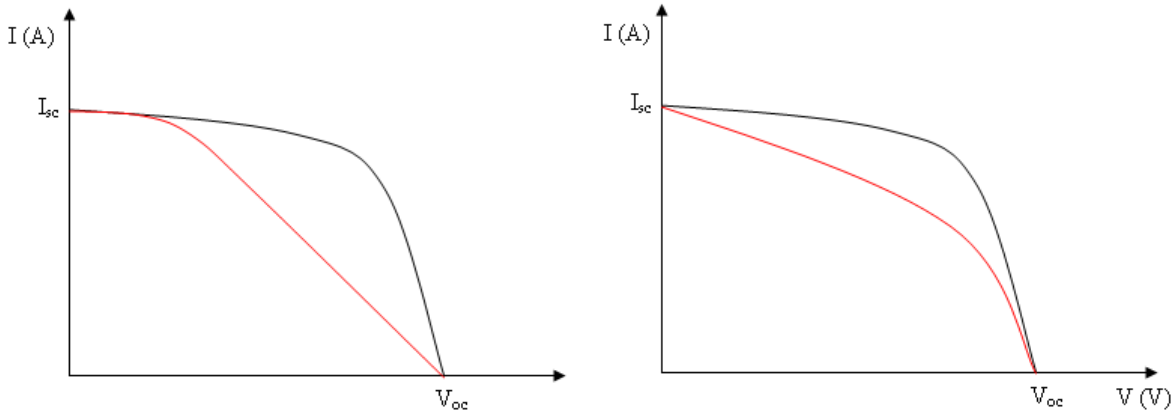

Figure 2.10: Effect of (a) high series resistance and (b) low shunt resistance, on the I-V curve of a PV module.

When the whole module is illuminated, as shown in Figure 2.8(b), the shunt resistances of the module cells don't contribute to the module series resistance, therefore the I-V curve tends to the ideal (black) curve. In this case the module series resistance is low and the shunt resistance is high.

2.5.2 I-V curve of a partially shaded PV module

When the module is partially shaded, for instance by shading a single cell, a drop in current results [45] and the I-V curve deviates from the fully illuminated one. For a fully illuminated PV module, as shown in Figure 2.11(b), the shunt resistances of the cells do not contribute to the module series resistance. When a single cell of the module is shaded as shown in Figure 2.11(a), shunt loss through its shunt resistance does not occur, but the shunt resistance contributes to the module series resistance, loading the circuit and causing a decrease in module output current.

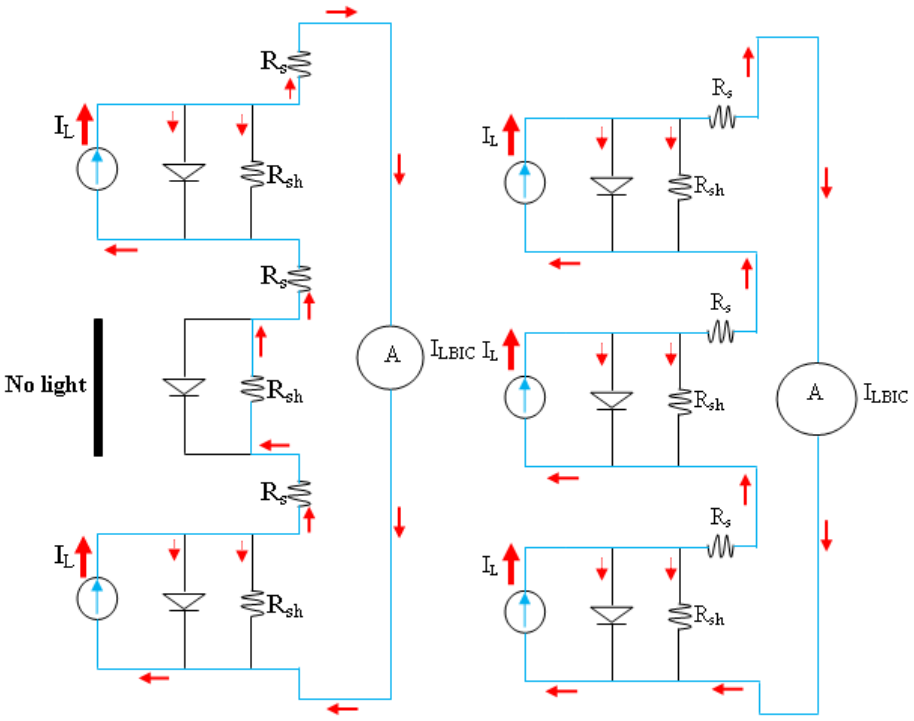

(a) Partial shading. **(b)** Full illumination.

Figure 2.11: PV module under partial shading and full illumination.

Under partial shading, the module series resistance can be increased substantially if the shaded cell is a good one (high shunt resistance), or is insignificantly changed if the cell is a weak one (low shunt resistance). The cell with a high shunt resistance therefore causes a large voltage drop that greatly reduces the current compared to the one with a low shunt resistance. The impact of shading a module cell is therefore reflected on the module I-V curve by a decrease in the slope at V_{oc} and as a consequence, the maximum power point is displaced to a lower voltage value on the module I-V curve [46]. It should, however, be noted that for the case of partial shading of a module, only the shunt resistance of the shaded cell contributes to the module series resistance, while for point illumination, the shunt resistances of all the non-illuminated cells add to the module series resistance, causing the point-illuminated module current to drop greatly. Figure 2.12 shows the I-V curves of a partially and fully illuminated PV module. It can be seen that, the slope of the I-V curve at V_{oc} is more reduced by shading a good cell, than a weak one. This is because the high shunt resistance of the good cell contributes to the module series resistance, as illustrated in Figure 2.11. The reduction in the slope of the I-V curve, at V_{oc} is indicative of an increase in module series resistance [47] resulting from shading. Shading a module cell with a high shunt resistance has a greater distortion effect on the module I-V curve than when a cell

with a low shunt resistance is shaded [48].

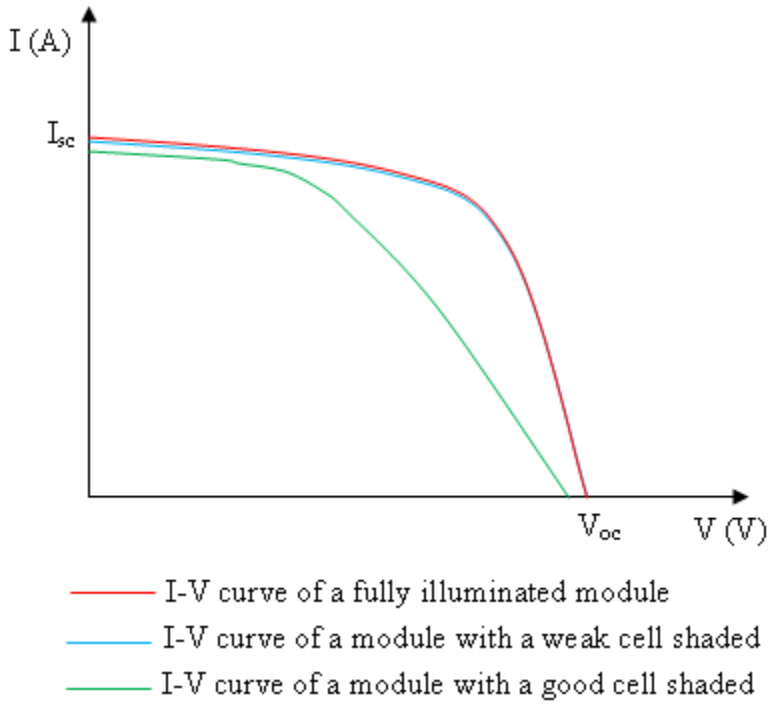

Figure 2.12: Effect of shading on module I-V curve.

2.6 A PV module under forward voltage bias

When an illuminated PV module is forward biased by a voltage source, a forward current that opposes the photo-generated current is generated. By increasing the forward bias, the module I_{sc} drops and reaches zero at V_{oc}, when the two opposing currents balance each other. When the forward bias current exceeds the photo-generated current, then the current direction in the module is changed, as shown by the part of the I-V curve in the fourth quadrant in Figure 2.13. Forward biasing of the module while measuring the module output current during LBIC scanning has been found useful for identification of severely shunted cells in the module [49]. Shunted cells at a forward bias voltage show a higher photo-response than the good cells. The current of the severely shunted cells is higher than those of good cells at the same forward bias voltage due to the crossing over of the I-V curves in the fourth quadrant.

Figure 2.13 shows how the I-V curves of a weak and a good cell cross at forward bias voltage V_1, where the current of the weak cell, I_1, becomes greater than that of the good cell, I_2. As can be seen in Figure 2.8 (a), point illumination of a module causes shunt current to flow

in the illuminated cell while no shunting occurs in the non-illuminated cells, as their shunt resistances contribute to the module series resistance. Shunting of the module I-V curve under point illumination is therefore dependent on R_{sh} of the point illuminated cell. When the point illuminated cell has a high R_{sh} (good cell), the increase in slope of the I-V curve at I_{sc} is lower compared to when the point illuminated cell has a low R_{sh} (weak cell). It can be seen that, by point-illuminating a weak and a good cell of a module, the I-V curves obtained have different slopes at I_{sc} and hence they cross over at some forward bias voltage. Beyond the cross over point, the weak cell begins to generate a higher current than the good cell. This concept is used in the analysis of results.

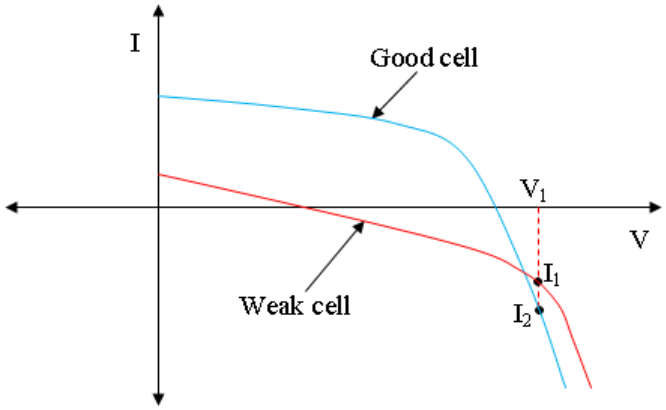

Figure 2.13: Crossing over of the I-V curves of a weak and a good cell during module forward bias.

2.7 Conclusion

In this chapter, a brief historical background of LBIC and LA-LBIC, including the various improvements that have taken place over time on the system hardware and additional new measurement techniques that have been incorporated to obtain reliable LBIC data, have been presented. The LBIC principle, illustrating how the photo-generated current varies with position from a defect, how shunts reduce the LBIC signal and how the operating point voltage of the cell being scanned shifts during scanning in the dark, were discussed. The different types of LBIC losses that occur during PV module scanning have also been discussed. The diode models of a solar cell were reviewed and the equivalent circuit model of a point-illuminated module was designed, to help in explaining the variations in photo-current that occur in LA-LBIC maps. The I-V characteristics of a point-illuminated and partially shaded module were presented and discussed using equivalent circuit models. The effect of

forward voltage bias on module photo-generated current, and how it can be used to identify severely shunted cells in the module, was discussed.

Chapter 3

Brief introduction to the photovoltaic cell technologies used in this study

In this work a literature review for both crystalline silicon and thin film technologies, is presented.

3.1 Crystalline silicon technology

Photovoltaic cells made from crystalline silicon fall into two groups, namely mono-crystalline silicon and multi-crystalline silicon. Mono-crystalline silicon solar cells are expensive to manufacture but have higher efficiencies than their multi-crystalline silicon counterparts which are less costly to produce but have a lower efficiency. Crystalline silicon photovoltaic cells are still widely used in commercial PV module production. The cells are well known for their high efficiencies and have demonstrated long-term stability for decades [50]. Photovoltaic modules made from crystalline silicon solar cells have a higher efficiency than any other technology, except for concentrator technology [51]. Without light concentration, crystalline silicon solar cells with a thickness of about 100 µm have a theoretical efficiency just under 30% [52] and efficiencies of 24-25% have been achieved by the best laboratory and commercial silicon PV cells [51].

3.1.1 Crystalline silicon solar cell manufacturing process

Silicon used for solar cell manufacture is obtained from silicon dioxide (SiO_2), occurring in sand, by reduction with carbon at 2 000$^{\circ}C$ according to equation:

$$SiO_{2\,(s)} + 2C_{(g)} \rightarrow Si_{(l)} + 2CO_{(g)}$$

The reaction is carried out in an electric furnace where the liquid silicon collects at the bottom of the furnace. The liquid silicon is drained and cooled and is called metallurgic-grade silicon (MG-Si), with a purity of about 98% [53]

The MG-Si is purified further to obtain polycrystalline silicon, which can be used as a raw material for making both polycrystalline and mono-crystalline silicon solar cells.

Polycrystalline silicon solar cells are made by melting the polycrystalline silicon in a quartz crucible and cooling it in a graphite crucible. Under controlled cooling, polycrystalline silicon block as large as 30 cm x 30 cm can be obtained, which is then used to produce silicon wafers. The merit of crystallising molten polycrystalline silicon in a graphite crucible is that, unlike the Czochralski process used to manufacture mono-crystalline silicon ingots, it does not contain critical quantities of oxygen that degrade solar cell performance, although residual impurities from the crucible walls are incorporated [36]. Using a diffusion process, the silicon wafers are doped to create the *pn* junction. For instance, if the wafer is p-type, then n-doping is required. Contact formation, tabbing and stringing can then be done by soldering to make modules. The cross section of a typical PV module, where the cells are connected by wiring, is shown in Figure 3.1.

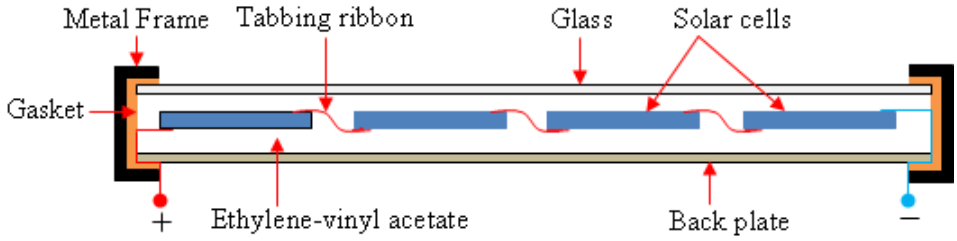

Figure 3.1: Cross-section of a PV module where the cells are wired in series [53].

Photovoltaic modules made from polycrystalline or mono-crystalline PV cells can easily be identified merely by their appearance [53]. Figure 3.2 shows photographs of mono-crystalline and polycrystalline silicon PV modules.

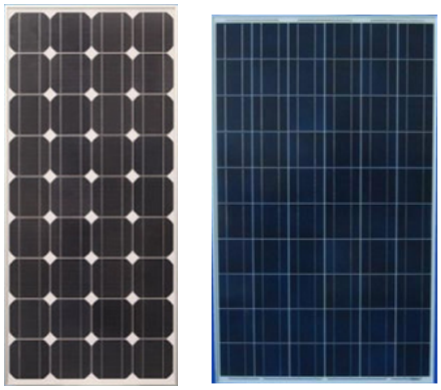

(a) (b)

Figure 3.2: Photographs showing the appearance of (a) Monocrystalline and (b) Polycrystalline silicon PV modules.

Mono-crystalline silicon solar cells are commonly made using the Czochralski process, where the polycrystalline silicon is melted in a quartz crucible and a seed crystal is dipped in the solution. A large crystal grows onto the seed crystal, which can be pulled out perpendicular to the melt surface. During the pulling process, the crucible and the seed crystal are rotated in opposite directions to minimise convection effects in the melt and also to enable the ingot to have a round shape. Balancing both movements and precisely controlling the temperature of the melt enables the growing crystal diameter to be adjusted. In order to obtain a large ingot of single crystal, the rate of pulling and the temperature of the melt should be controlled. The limitation of the Czochralski process is its inability to produce square wafers which can be used to make a highly efficient PV module [54]. The ingot, which can be 30 cm in diameter and 2 metres long, is then sliced into thin silicon wafers which are used to make solar cells using the same process as described for polycrystalline silicon. The problem associated with growing crystals in a quartz crucible, is that the crucible dissolves in the melt, releasing oxygen atoms which act as recombination centres for charge carriers in solar cells [36].

3.1.2 Defects in crystalline silicon solar cells

The introduction of defects into solar cells or modules may occur during the production process, during transportation or in the field. A defect, by definition, is anything in a PV cell or module that makes the cell or module different from what it is expected to be [55]. Common defects in crystalline silicon solar cells and modules include cracks, black core or striation ring features and grain boundaries.

Cracks are more common in crystalline silicon modules than their thin film counterparts

because of the fragile nature of the crystalline silicon material. Cracks in PV cells or modules cause electrical disconnection, resulting in the two isolated sections having completely different electrical characteristics. A 2 µm wide crack in a solar cell may partly disconnect the finger whereas a 7 µm wide crack disconnects it completely [56]. Cracks lead to current mismatch in the module and consequently lower the module output current. The soldering process during module manufacture may lead to crack formation as a result of the thermal stress developed during the process [57, 58, 59]. The heat during soldering causes both the cells and the tabs to heat up and the consequent differential contraction after cooling when the heat is removed, with the tabs contracting more than the silicon, causes thermo-mechanical stress to build up, which may cause cracks in the silicon [60]. Crack formation on the bus bar of crystalline silicon solar cells, caused by mechanical stress, has also been reported [61]. Cracks may also form during the cutting of ingots [62]. Cracks which develop parallel to the bus bar are more detrimental to the module performance than those which are perpendicular [63]. A crack which is parallel to the bus bar disconnects many fingers, as it is perpendicular to the fingers, while a crack perpendicular to the bus bar hardly affects the fingers. A crack in the silicon appears with an irregular shape, while that on a finger is seen as a dark rectangular pattern in an electroluminescence image [10] . Cracks lead to a remarkable increase in the series resistance of solar cells [64]. Cracks in PV modules have been investigated using different techniques which include EL [65, 60, 59, 66, 67], UV fluorescence [8], infrared (IR) reflectance imaging [68] and electronic speckle pattern interferometry (ESPI) [69].

Defects in solar cells may also result from unintentional incorporation of impurities such as oxygen, carbon and transition metals like iron, chromiun, nickel, copper and zinc. The impurities act as traps for charge carriers, lowering the solar cell efficiency. Oxygen precipitates formed in crystalline silicon solar cells as a result of oxygen incorporation into the melt, reduce solar cell efficiency by reducing the minority carrier diffusion length [70]. The defect appears as a dark ring in both photoluminescence [9] and EL images [55], and can cause efficiency losses of up to 4% [71]. Formation of boron-oxygen [72] and iron-oxygen [73] complexes have also been reported to degrade the minority carrier lifetime in crystalline silicon solar cells.

Grain boundaries are common defects in multi-crystalline silicon solar cells and act as recombination centres for charge carriers, reducing the current that would be generated. The effect of a grain boundary is that it divides the semiconductor into regions with the minority carriers having different lifetimes [74].

3.2 Thin film PV technology

The thin film PV technologies considered here are restricted to amorphous silicon (a-Si) and copper indium diselenide. Thin film solar cells and modules are less expensive to manufacture compared to crystalline silicon solar cells because they require less material and less expensive production methods. However thin film modules require more space, have lower efficiency and their lifespan has not been proved comparable to their crystalline silicon counterparts.

3.2.1 Structure of thin film solar cells

A thin film solar cell consists of multiple thin layers of PV material stacked together and a typical structure is illustrated in Figure 3.3. The transparent conducting oxide (TCO) at the top, such as zinc oxide or tin oxide, allows the entry of light into the cell and acts as the front conducting electrode. The anti-reflection coating (e.g. silicon nitride), applied beneath the TCO, reduces surface reflection in order to maximise cell efficiency. The n-layer absorbs light from the high energy part of the spectrum while the low energy part is absorbed in the p-layer. The back contact, usually made of aluminium or molybdenum, connects the cell to the external circuit.

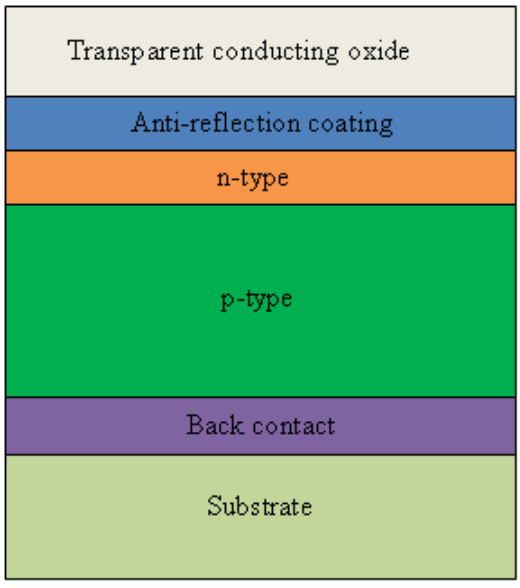

Figure 3.3: Structure of thin film solar cell.

3.2.2 Thin film PV module manufacturing process

Thin film PV modules are manufactured by depositing thin layers of PV material onto a substrate [75] made of glass, a polymer or a metal. The manufacturing process of a monolithically interconnected module begins with the cleaning of the substrate material on which the PV material is supposed to be deposited. The back contact material, usually molybdenum, is then deposited on the substrate, followed by P1 patterning, as shown in Figure 3.4, to electrically isolate the back contact of individual cells from each other.

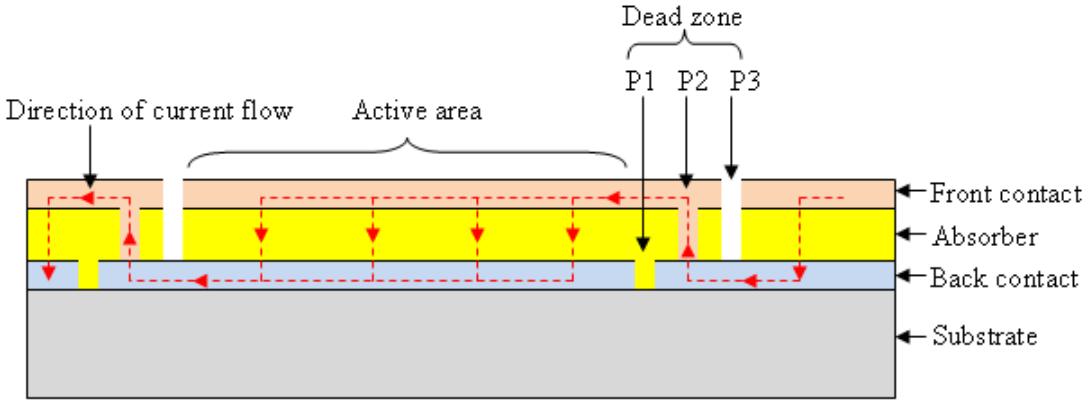

Figure 3.4: Monolithic interconnection of thin film PV module.

After depositing the back contact, the absorber layer is deposited and P2 patterning is performed in order to interconnect adjacent cells. Ideally, P2 scribing helps to connect the front contact of one cell to the back contact of the adjacent cell. Finally, the TCO layer is deposited, followed by P3 patterning to electrically isolate the adjacent cells. The patterning (scribing) process is performed using lasers in order to isolate and interconnect the cells.

The deposition of thin film of PV material over a large area during the manufacturing process makes thin film modules vulnerable to thickness variation and consequently operating as a non-homogeneous device with suboptimal performance. The effects of the absorber layer thickness on performance of solar cells have been extensively reported [76, 77, 78, 79]. The laser scribing process used to isolate and interconnect thin film module cells can also cause inhomogeneity in the module [80, 81].

3.2.3 Current status of thin film module technology

Amorphous silicon PV modules are the first of the thin film PV devices to be commercially available in the market [82]. Amorphous silicon dominated global annual thin film PV

module production until 2006 when it was out-competed by cadmium telluride technology. By 2014, the production of a-Si had dropped drastically [83], as shown in Figure 3.5. The recent conversion efficiency of a-Si triple junction cells and modules are 13.6% and 10.9%, respectively, while for single junction cells the efficiency has gradually improved from 2.4% in 1976 [84] to 10.2% in 2015 [85]. Amorphous silicon modules are unstable under outdoor conditions [86] and they have lower efficiency compared to other thin film technologies, partly because of the Staebler-Wronski Effect (SWE).

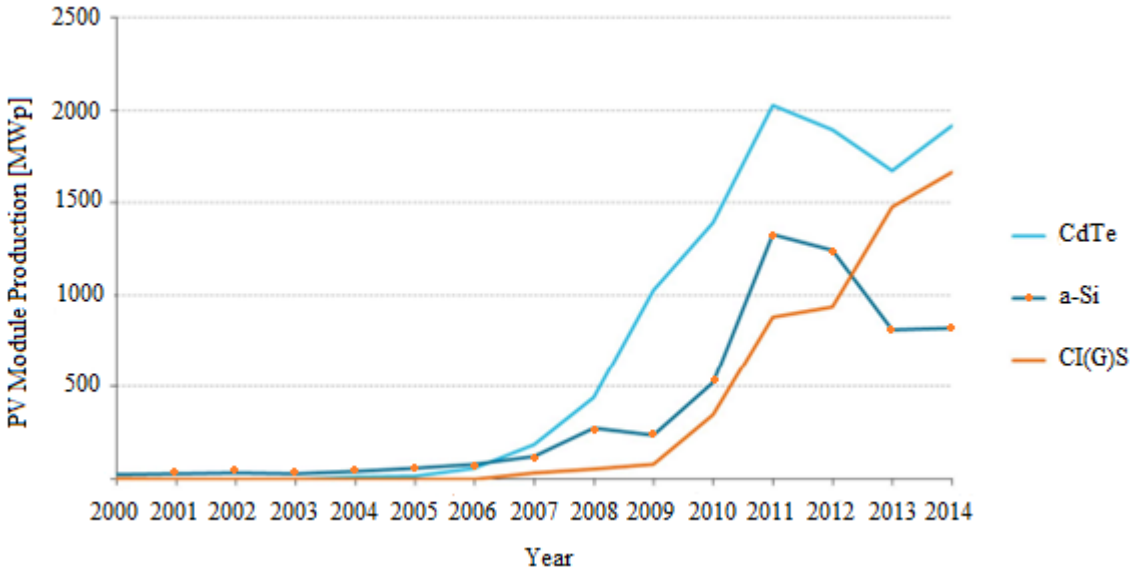

Figure 3.5: Annual global thin film PV module production [83].

Reasonable annual global production of copper indium (gallium) diselenide, CI(G)S, PV modules started in 2006 and has continued to increase, surpassing a-Si in 2013, as shown in Figure 3.5. Great advances in increasing the efficiency of CI(G)S solar cells have taken place over the years, giving a lot of hope in the use of CI(G)S cells for module construction. Efforts to increase CI(G)S solar cell efficiencies have been successful with an efficiency record of 18% for a 0.5 cm^2 cell in 2009 [87], 19.7% for a 0.5 cm^2 cell in 2013 [88] and the latest world record of 20.9% for a 0.52 cm^2 cell in 2014, achieved by Solar Frontier and confirmed by the Fraunhofer Institute of Solar Energy [89], although the record module efficiency still stands at 18.7% [90, 91]. The key challenge with CI(G)S PV modules is the degradation caused by moisture, however, enhancement of the lamination foil with edge sealing tape during the encapsulation process is found to strongly mitigate moisture ingress and degradation [92]. Photovoltaic modules, by international standards, are required to degrade by less than 20% of their original power in 20 years [93].

3.3 Conclusion

Two PV technologies namely, crystalline silicon and thin film, have been reviewed. The manufacturing process for crystalline silicon solar cells and modules was described and some of the defects which arise mainly from the manufacturing process were discussed. The structure of thin film solar cells was presented and a description of the processes involved in the manufacture of thin film modules was given. Finally the current status of thin film module technology was reviewed.

Chapter 4

LA-LBIC measurement technique for photovoltaic module characterisation

4.1 System development

The LA-LBIC measurement system used in this study was developed at the Centre for Energy Research, Physics Department, Nelson Mandela Metropolitan University. The major system hardware consists of the scanning light source, the source measurement unit (SMU) and the motion control system. The motion control system consists of the application software, motion controller, amplifier or drive, motor and the mechanical element (x-y stage). The schematic diagram and the photograph of the LA-LBIC system is presented in Figure 4.1. The maximum area which can be scanned by the system is 1.3 m x 1.3 m. In order to keep away external light during measurements, the scanner is housed in a dark enclosure.

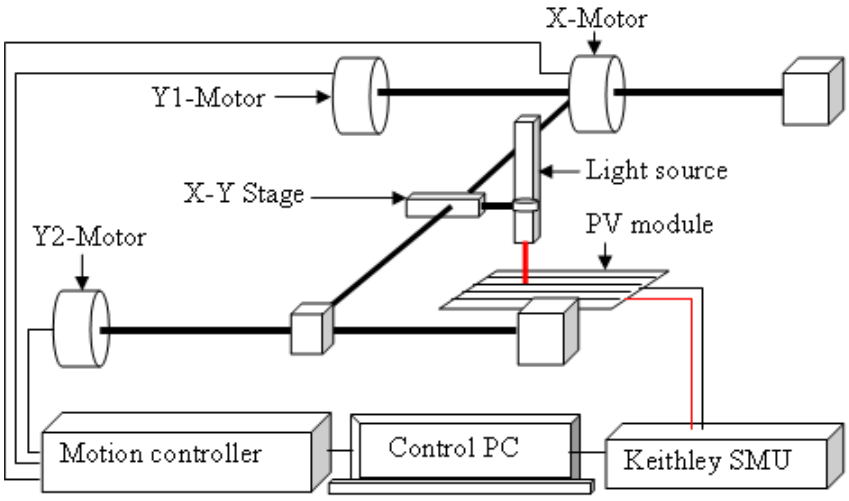

(a)

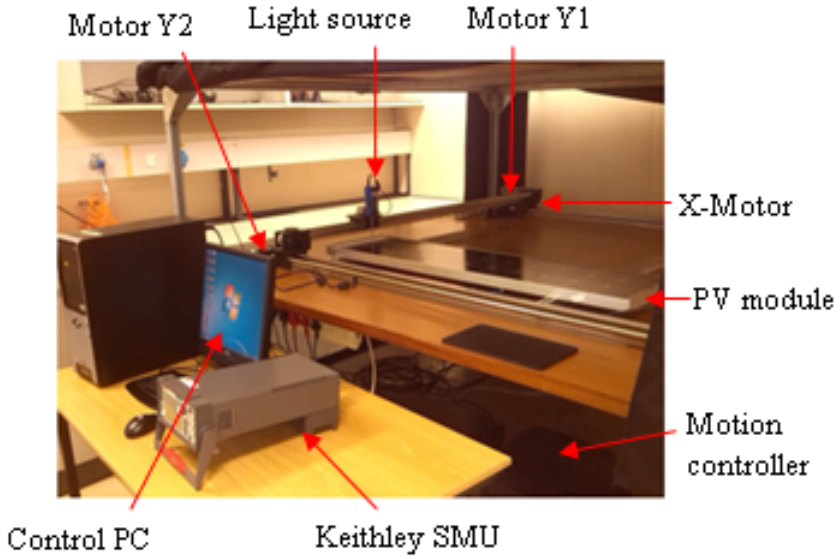

(b)

Figure 4.1: The LA-LBIC system used for PV module scanning showing (a) the schematic diagram (b) the photograph.

4.2 System components

4.2.1 Scanning light sources

Two types of light sources were used in this study to scan the PV modules, namely a white light source and a laser light source. The white light that was used has a wavelength range of 360-2 400 nm and can therefore excite electrons at various depths of the solar cell material.

The white light has a larger light spot diameter than the laser light source and this facilitated the scanning of larger modules that would otherwise require a longer time to scan with laser light. The limitation of the larger spot size is that it has a low resolution and some of the LBIC features that require high resolution scanning may not be visible. A photograph of the white light source is shown in Figure 4.2.

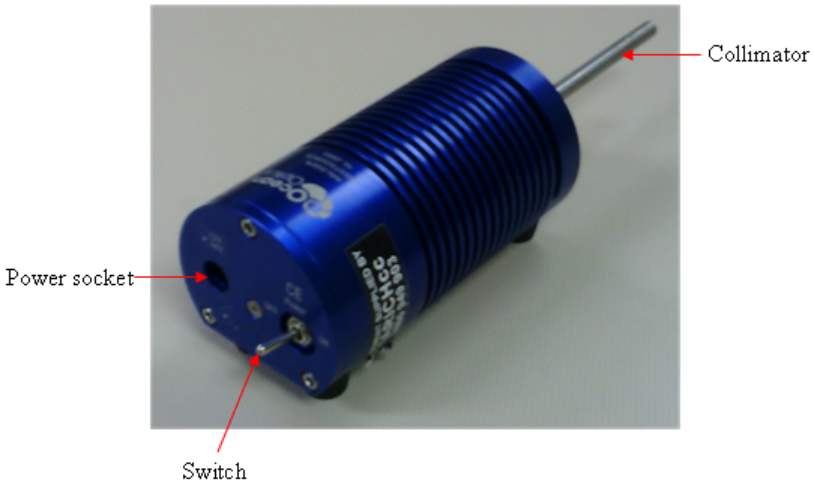

Figure 4.2: Photograph of a white light source used to scan PV modules.

The second type of light source used is the laser diode. Figure 4.3 shows a photograph of a laser diode. Laser diodes emit monochromatic light and by using different laser wavelengths, different regions of the cell material can be investigated. Scans can also be performed at different light intensities, by varying the laser power.

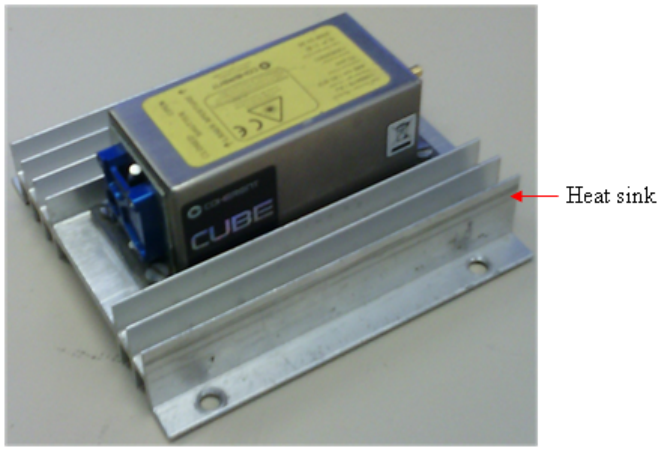

Figure 4.3: Photograph of a laser used to scan PV modules.

4.2.2 Source Measurement Unit

The source measurement unit (SMU) instrument is capable of both acting as a current or voltage source and simultaneously taking measurements (current or voltage) from the device under test (DUT). The instrument has a four-quadrant, precision source, i.e., it has the capability to source current or voltage according to the settings and measurements can extend from maximum positive output to maximum negative output without the need to change the test leads. The Keithley SMU Model 2450 used in this study has a power supply, digital multimeter, arbitrary waveform generator, voltage or current pulse generator, electronic load and trigger control. The instrument is operated through a touch screen interface or by remote control using a computer. In this investigation, the module is illuminated point-by-point while the SMU is used to bias the module at a fixed voltage and at the same time record the module output current. A photograph and the equivalent circuit diagram illustrating the working principle of the SMU are shown in Figure 4.4. The anode of the solar cell or PV module is connected to the Force HI and Sense HI terminals (Red) while the cathode is connected to the Force LO and Sense LO terminals (Black). In order to measure the module current as a function of position at a fixed bias voltage, the output of the SMU is set at that particular bias voltage. When the module is illuminated, the photo-generated current will flow into the output terminal of the instrument as illustrated in Figure 4.4. The instrument acts as an electronic load to the inflowing current, sinking it and as a result the measured current is negative. Since the PV module is a power generator, during data analysis the measured current values are therefore multiplied by -1. Measurement of the module I-V characteristic is done by specifying the voltage steps and voltage range of the measurement on the input window of the SMU. The SMU then measures current at each voltage, giving the I-V characteristic of the module.

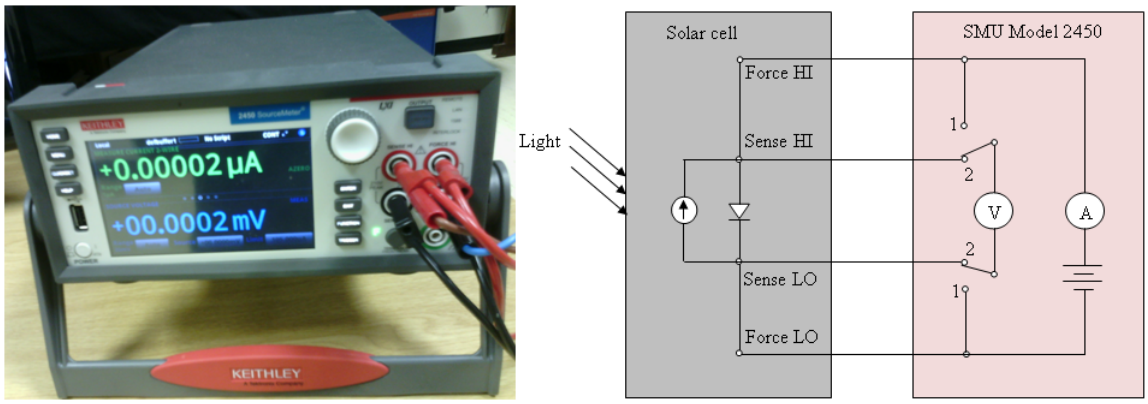

(a) (b)

Figure 4.4: Keithley SMU showing (a) photograph (b) equivalent circuit illustrating the working principle.

4.2.3 The motion control system

The motion control system consists of the application software, motion controller, amplifier or drive, motor and mechanical element (load).

4.2.3.1 Application software

The application software is used by the computer to communicate with the motion controller to move the x-y stage according to the specified motion parameters, and also to communicate with the SMU to record current measurements at each step of the point-by-point motion of the light source mounted on the stage. The program controls the scanner using the RS 232 interface and the SMU through the GPIB interface. The SMU is incorporated into the scanning program and is used to bias the module and measure the photo-generated current.

Consider the screenshot of the front panel of the labView scanning program in Figure 4.5. The light spot is positioned at the desired location on the module surface by using the "Towards" or "Away" buttons for movement of the stage along the x-axis direction and the "Right" or "Left" buttons for movement along the y-axis direction. The set spot position is made the starting point for the scan by using the "Set zero" button. The "Start scan" button opens another window as shown in Figure 4.6, which enables the user to select the desired type of scan and specify the motion parameters. For instance, by choosing the "Photo-response vs. position" scan type, the user is prompted to specify motion parameters such as the scan distance and the number of scan steps for both x and y axes. When the

scan is started through the "Start scan" button, the scan runs to the end, after which the user will be prompted to save the data and stop the program.

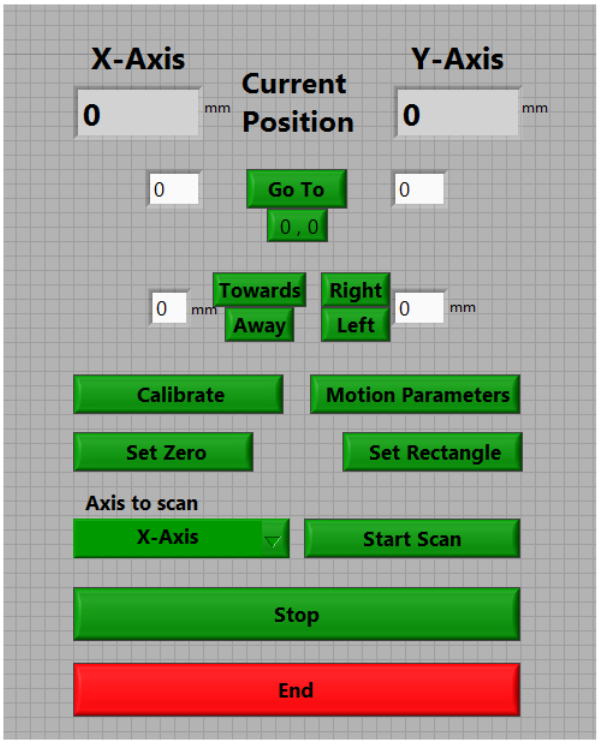

Figure 4.5: Screenshot of the front panel of the LabView scanning program.

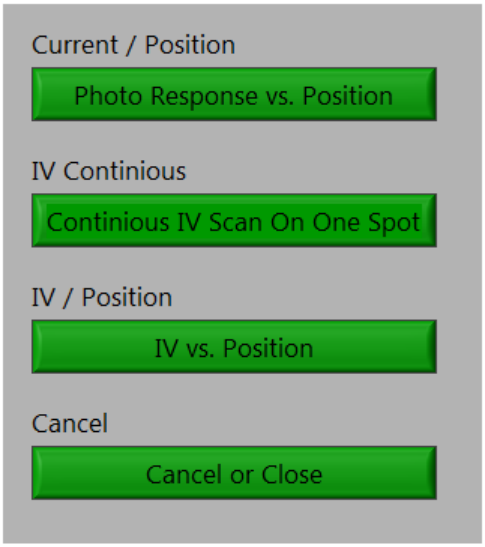

Figure 4.6: Screenshot of the front panel of the LabView scanning program showing different scan type options.

4.2.3.2 Motion controller and drive

The motion controller is the brain of the motion control system, receiving the motion parameters from the computer through the application software and deciding the appropriate command to send to the drive. The command is transmitted by outputting a voltage signal to the drive. The drive converts the voltage signal received from the motion controller into a signal with high current to drive the motor. One drive communicates with the x-motor while each of the two y-motors has a drive assigned to it.

4.2.3.3 Motors and x-y stage

Three stepper motors are used for the 2-D movement of the stage. One x-motor is linked to the scanning stage to effect motion in the x-direction, while two y-motors move the scanning stage along the y-direction.

The x-y stage is the carrier for the scanning light source and is motorised by the stepper motors. The 2-D motion of the x-y stage makes it possible to scan the entire module or an area of the module depending on the specified motion parameters. A photograph of the x-y scanning stage is shown in Figure 4.7.

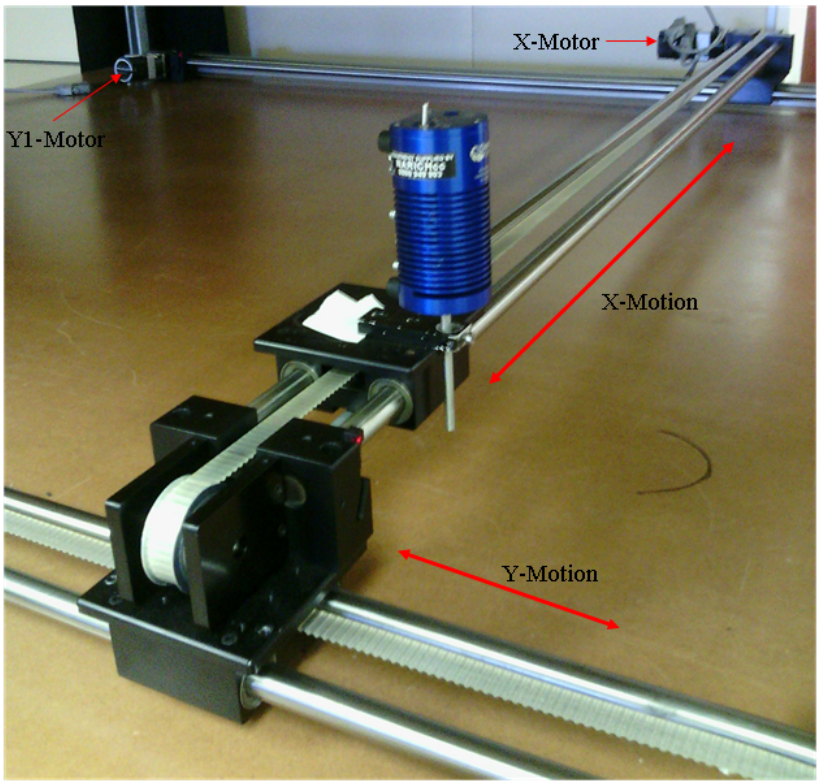

Figure 4.7: The x-y scanning stage of the LA-LBIC system.

The components of the motion control system, showing the sequence of events that take place leading to the movement of the x-y stage are summarised in the flow diagram in Figure 4.8.

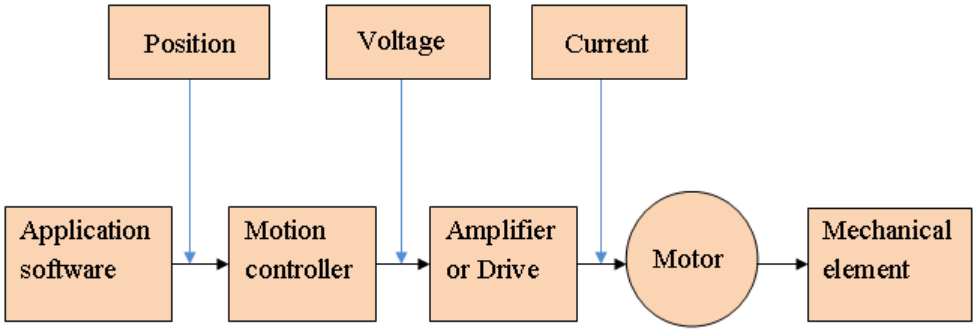

Figure 4.8: Schematic diagram showing the different components of the LA-LBIC motion control system and the linkage between the different components.

The application software is used to specify the target positions and motion profiles on the motion controller. The motion controller, by outputting a voltage signal, commands the drive to instruct the motor accordingly. The motor receives a current signal from the drive and moves the x-y stage according to the specified motion parameters.

4.3 The LA-LBIC measurements

The LA-LBIC system was set up as described previously in Figure 4.1. When scanning PV modules, unlike in the case of PV cells, it is preferred to move the laser during the scanning process while the module remains stationary. Moving the module while the laser is fixed, as is the case when investigating PV cells, presents a challenge, namely, a larger scanning space would be required to scan a module that could conveniently be scanned by the moving laser method, and also heavy modules would overload the motors and affect their efficiency. Scanning is performed using a light source, point-by-point, while measuring the photo-generated current at each point. The scanning step size is made smaller than the light spot diameter to ensure that no area of the device is left without probing. By specifying the bias voltage on the output of the SMU, modules can be scanned under different voltage bias levels. Scanning was done in a dark enclosure to ensure that there is no interference from external light.

4.4 Conclusion

The development of the LA-LBIC system used for the non-destructive characterisation of PV modules has been described. The different components used to build up the system were described. The role played by each of the system components and the linkages between them were also outlined. The LA-LBIC measurement set-up was described and the justification for moving the laser instead of the module during scanning was given. Finally, some of the techniques employed during measurements were described.

Chapter 5

Complementary techniques to LBIC Characterisation

5.1 Electrical current-voltage (I-V) characterisation

The most common and traditional method for determining the electrical performance of a PV module is by measuring its current-voltage characteristics. Electrical performance parameters can be determined from the measured I-V curve, extracted using appropriate curve fitting techniques or calculated from the extracted parameters. In this section, the theory of I-V charcterisation, I-V curve measurement and the different types of I-V curve deviations are considered.

5.1.1 Theory of I-V characterisation

Photovoltaic cells used to construct PV modules are modeled as a current source in parallel with a diode, as described in section 2.4. In the absence of light, the I-V characteristic of a PV cell is typically that of a diode. The solar cell I-V curve is a result of the superposition of the cell dark I-V curve with the illuminated one [94]. Figure 5.1 shows the dark and the illuminated solar cell I-V characteristics, where the dark I-V characteristic is shifted by the photo-generated current, I_L.

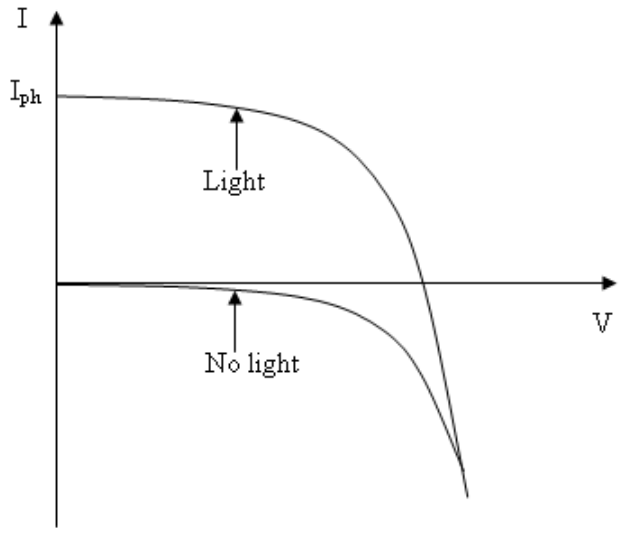

Figure 5.1: I-V characteristics of a solar cell in the dark and under illumination.

In the case of the single diode model, the I-V characteristics of a solar cell can be described by equation 2.12:

From equation 2.12, it can be seen that the I-V characteristic of a solar cell is rich in information, which when determined, can be used to evaluate the module performance. The unknown five parameters in equation 2.12 include I_L, I_0, n, R_s and R_{sh}. I_L is dependent on the irradiance and I_0 is affected by cell temperature, while n, R_s and R_{sh} remain constant [95]. These parameters can be extracted based on the single diode [96, 97, 98] and double diode models [99] using mathematical techniques. Additional parameters that can be obtained directly from the I-V curve include the short circuit current, I_{sc}, and the open circuit voltage, V_{oc}, as shown in Figure 5.2. Performance parameters that can be calculated using the extracted parameters include current (I_m) and voltage (V_m) at maximum power point, fill factor and efficiency.

I_{sc} and V_{oc} are affected by irradiance and temperature, respectively. This is illustrated in Figure 5.2. When irradiance is increased, more photons become available for absorption and I_{sc} increases. When temperature is increased, the resistance in the module circuit increases, leading to a voltage drop which consequently reduces V_{oc}.

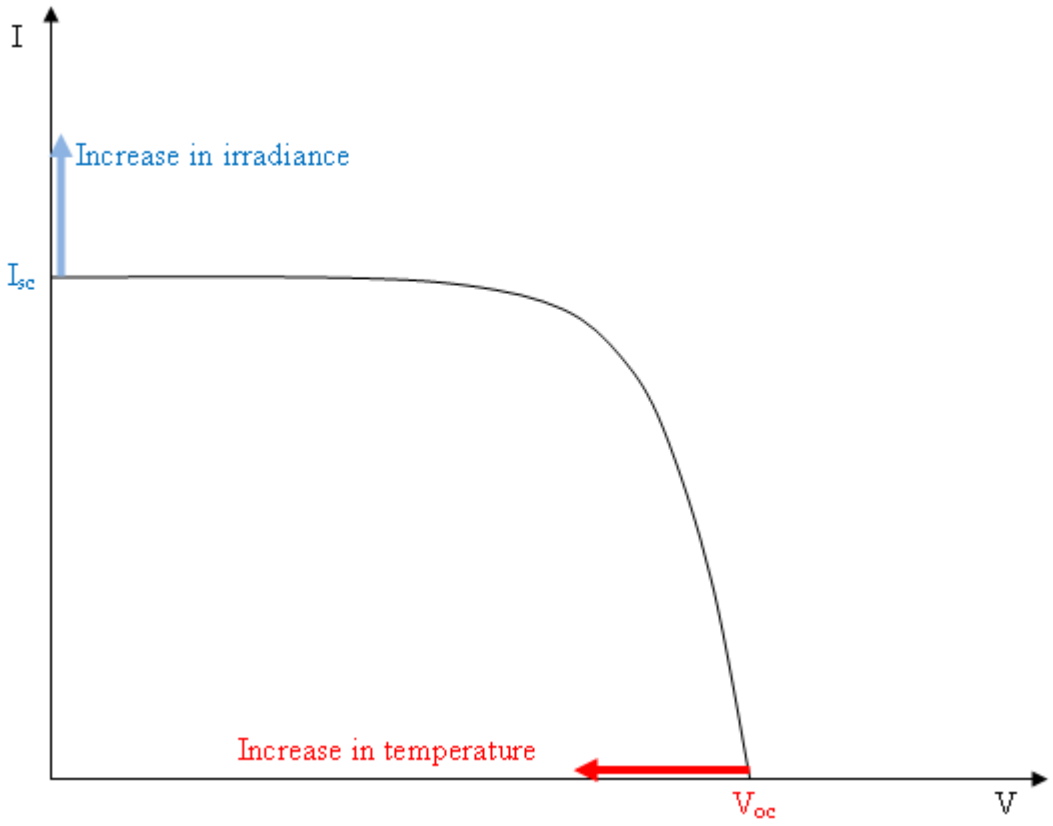

Figure 5.2: Effect of change in irradiance and temperature on I-V curves.

5.1.2 I-V curve measurement

In order to obtain the I-V characteristic of an illuminated PV module, a method of measuring the current under different bias levels is required. Different techniques have been devised to achieve this and they include using a variable load resistor [100], electronic load [101, 102] and capacitive load [103]. For measurement of the I-V curve in the power quadrant, current has to be varied from I_{sc} to zero, which consequently causes voltage to change from zero to V_{oc}. By plotting the measured current values against the corresponding voltages, an I-V characteristic of the module is obtained.

The I-V characterisation system used in this study is the one developed by PV-Engineering [104] and uses a capacitive load. The system is known as the photovoltaic power measurement (PVPM) system. The connections of the different peripheral devices to the PVPM system are shown in Figure 5.3. The peripheral devices include a USB cable for connecting the system to the computer (1), an external power supply (2), an irradiance reference sensor (3), an external RTD (Pt100) or short circuit adaptor (4), an external security switch connected between the power measurement cable and the PVPM (5) and the 4-wire measurement cable

(6).

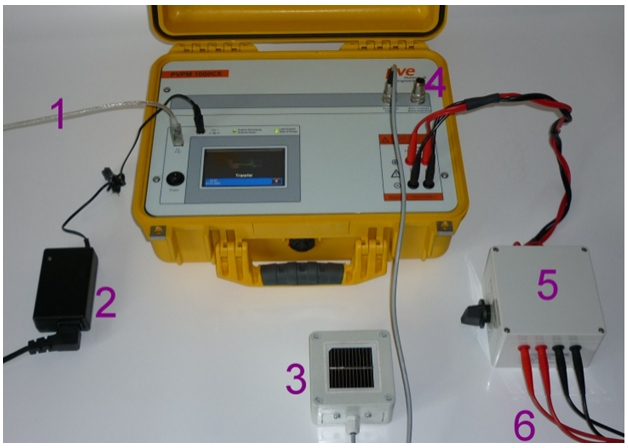

Figure 5.3: The PVPM system showing the connections of the peripheral devices.

The PVPM system is operated by use of a touch screen and an on-screen menu. Measurement can be started from the PVPM or from the connected computer. The PVPM measures the I-V characteristic of the module within 2 seconds and from the measured data it calculates the module peak power (P_{max}), series resistance (R_s), parallel resistance (R_p) and fill factor (FF). The measured and the calculated parameters, including values at STC, are displayed. When setting up for measurements, the irradiance reference cell should be mounted close to the module under investigation, with exactly the same orientation. During measurement, irradiance should be above 500 W/m^2, otherwise the results would be less precise.

5.1.3 I-V curve deviations

When the measured I-V curve deviates significantly from the predicted one, the nature of the deviation can give a hint as to the cause of the performance problem. The three most common deviations on the I-V curve are increased slope at I_{sc}, reduced slope at V_{oc} and steps appearing at the vertical leg of the I-V curve. These three I-V deviations are presented in Figure 5.4 [105].

The increase in slope at I_{sc} is a manifestation of a reduction in the module shunt resistance [48]. Low shunt resistance leads to power loss in the module by diverting part of the photo-generated current. Reduction in shunt resistance of the module is usually caused by the presence of defects which may arise from the manufacturing process [106] or from the solar cell material [107]. Decrease in slope at V_{oc}, which causes flattening of the I-V curve, indicates that the module series resistance has increased [40] and one of the possible

causes is the presence of cracks in the module [64]. Steps on the I-V curve are due to the effect of current mismatch in the module [105]. This can arise from partial shading or soiling [108, 109] and cracks in the module [65].

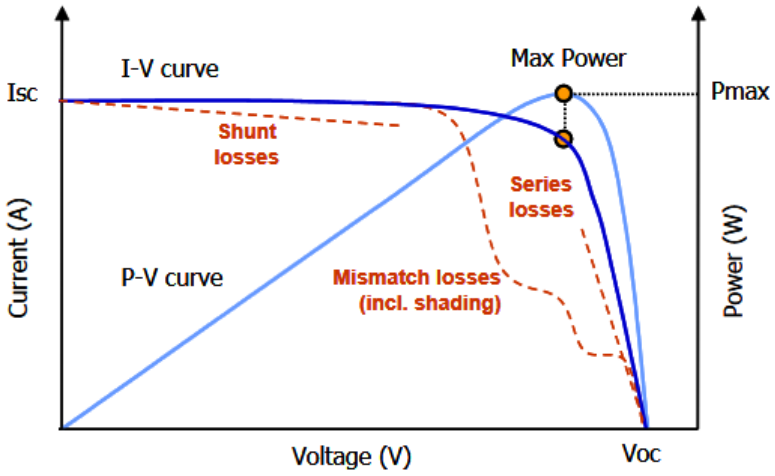

Figure 5.4: Different types of I-V curve deviations [105].

5.2 Electroluminescence (EL) imaging

Electroluminescence imaging is one of the many non-destructive characterisation techniques used to characterise photovoltaic cells and modules. The technique was introduced by Fuyuki in 2005 [110] to determine the diffusion length in solar cells. In this section, the basic principle of EL imaging is outlined. The electroluminescence imaging system is described and the procedure used to acquire an EL image of a PV module is presented.

5.2.1 Electroluminescence imaging principle

EL imaging involves forward biasing a PV module using a d.c. power supply and then measuring the induced photoemission using a CCD camera. The module is forward biased with current $\leq I_{sc}$ of the module. When a semiconductor is forward biased with current, charge carriers are excited, with electrons occupying the conduction band and holes occupying the valence band. The electrons in the conduction band are in a meta-stable state and therefore directly combine with the holes in the valence band through radiative recombination, as shown in Figure 5.5.

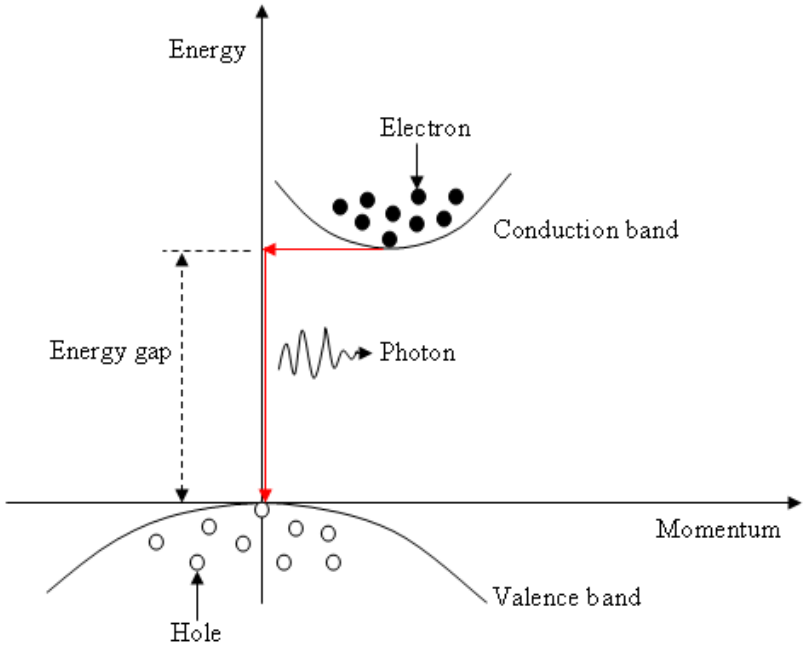

(a)

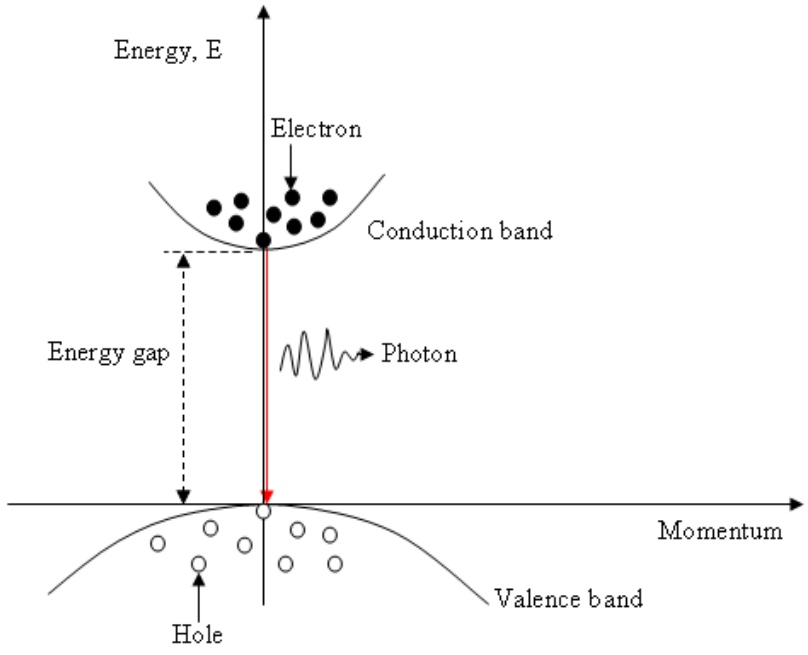

(b)

Figure 5.5: Radiative recombination of charge carriers in a material with (a) Indirect band gap (b) Direct band gap.

Radiative recombination occurs when an electron from the conduction band recombines with a hole in the valence band and the excess energy is emitted as a photon. When an electron from the conduction band recombines with a hole in the valence band, energy and momentum must be conserved. In indirect band gap material, the momentum of electron in

the conduction band and holes in the valence band are different. Therefore loss in momentum of electrons must occur before they can recombine with holes. Electrons can lose momentum when they interact with phonons. Therefore radiative recombination in indirect band gap material is a two-step process involving both momentum and energy losses. In direct band gap material, the electrons in the conduction band and holes in the valence band have the same momentum and recombination can simply occur through a one-step process, as seen in Figure 5.5(b).

The rate of radiative recombination, R, is directly related to the product of the concentration of electrons and holes, as shown in Equation 5.1 [111]:

$$R = Bnp \tag{5.1}$$

where B is the bimolecular recombination coefficient and can be calculated from the energy gap, absorption coefficient and refractive index [111], n is the concentration of electrons in the conduction band and p is the concentration of holes in the valence band.

As a consequence of radiative recombination, photons of light are emitted. The energy of the emitted photon and the band gap energy are similar and as a result very few photons are absorbed and hence must exit the semiconductor. A CCD camera is used to capture and process the emitted photons into an EL image, which shows the intensity distribution of the area under investigation. In order to improve the measurement accuracy, measurements under module forward bias and without forward bias should be taken and the one without forward bias subtracted from that with forward bias. This helps to remove the dark signal of the camera and mitigate the impact of background light on the measurements [112].

The local EL intensity at position $\mathbf{r}$, $\phi_{EL}(E, \mathbf{r})$, can be expressed as shown in equation 5.2 [113]:

$$\phi_{EL}(E, \mathbf{r}) = Q_e(E, \mathbf{r})\phi_{bb}(E)exp\left(\frac{qV_j(\mathbf{r})}{kT}\right) \tag{5.2}$$

where E is the photon energy, $V_j(\mathbf{r})$ is local junction voltage, $^{kT}/_{q}$ is the thermal voltage, $Q_e(E, \mathbf{r})$ is the local external quantum efficiency and $\phi_{bb}(E)$ is the local spectral density of a black body.

The local EL signal of each pixel detected by the camera, $S_{cam}(r)$, is expressed as [114]:

$$S_{cam}(\mathbf{r}) = \int Q_{cam}(E)\phi_{EL}(E, \mathbf{r})dE \tag{5.3}$$

where Q_{cam} is the spectral sensitivity of the camera.

The captured EL signal is processed into an EL image, where areas with defects appear dark while areas devoid of defects appear bright [115]. Defects act as traps for charge carriers and hence they appear dark in the EL image due to the low EL emission. Valuable information about the semiconductor properties can be obtained by analysing the light intensity distribution on the EL image. Current limiting features such as cracks [65, 60, 59, 66, 67] and striation ring features [116] in PV modules have been investigated using electroluminescence imaging.

5.2.2 Electroluminescence imaging system

The electroluminescence imaging system used in this study was developed by Crozier [116] and the photograph and schematic diagram are presented in Figure 5.6. The basic components of the system are the d.c power supply, CCD camera and a control computer.

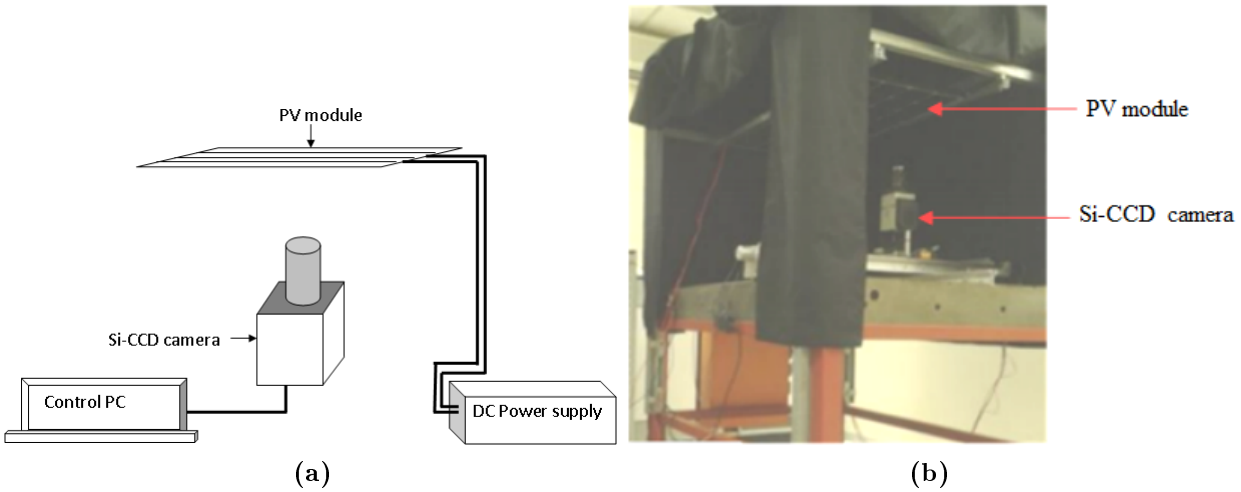

Figure 5.6: EL imaging system showing (a) Schematic diagram (b) Photograph.

The power supply is used to provide a forward bias current to the module during the imaging process. The camera is used to capture the luminescence resulting from the module forward bias effect and it is mounted on a moveable x-y stage, such that it is perpendicular to the plane of the module on a carrier above it. By moving the camera, luminescence at any location of the module can be captured. In order to mitigate the noise arising from the dark current, cooling of the CCD camera chip to a temperature 50°C below the ambient temperature is required. The camera acquires data within a period ranging from 1.5 to

2.5 seconds. A computer is interfaced with the CCD camera and a software developed by Sensovation Company is used for image processing and analysis. In order to prevent interference from external light, the entire system is placed in a dark enclosure.

5.3 Conclusion

Two non-destructive characterisation techniques, namely, electrical I-V characterisation and EL imaging, which were used to complement the LA-LBIC technique, have been discussed. The theory of I-V characterisation was outlined and I-V curve measurements using the PVPM system was described. The different types of I-V curve deviations and their causes have been discussed and their relationships with the detected LA-LBIC features explored. Finally, the EL imaging principle was outlined, the imaging system set-up was presented and a description of how the system works was given.

Chapter 6

Characterisation of crystalline silicon and thin film photovoltaic modules

6.1 Introduction

In this study, crystalline silicon (c-Si, mc-Si) and thin film (a-Si, CIS) PV modules were characterised using a large area light beam induced current (LA-LBIC) mapping system as well as various cell-shading scenarios. LA-LBIC mapping involves point-by-point scanning of a PV module, while measuring the module output current. A source measurement unit (SMU) was used to measure the photo-current as well as provide a constant voltage during scanning, as explained in chapter 4. The I-V characteristics of a fully and partially shaded module were also obtained and used to extract the shunt resistances of the cells in a module.

6.2 Equivalent circuit model

The equivalent circuit models of a spot-illuminated and partially shaded PV module were used to explain the variation in the photo-generated current in a module. Application of the model to crystalline silicon modules attributed the variations in photo-generated current between cells mainly to current mismatch between series-connected cells. Current variations within cells is attributed to individual cell shunts, which may arise from improper edge isolation, crystal defects, impurity inclusion, scratches, cracks and metallisation penetrating the emitter to form contact with the base (Schottky-type shunts) [117]. Application of the model to thin film modules attributed the variations in photo-generated current between or within cells mainly to differences in local cell shunt and series resistances originating from

the scribing procedure during cell formation in the manufacturing process. Variation in photo-current in thin film modules may also arise from deposition non-uniformity of the PV material.

6.3 Mono-crystalline silicon (c-Si) PV module

The investigated module consists of 36 cells in two series-connected strings of 18 cells each. The manufacturer's specifications under Standard Test Conditions (STC) are as shown in Table 6.1.

Table 6.1: Manufacturer's STC performance parameters for the c-Si module.

Performance parameters	P_{max}(W)	V_{mp}(V)	I_{mp}(A)	V_{oc}(V)	I_{sc}(A)
Values at STC	90	18.4	4.90	22.4	5.50

A white light source of 360-2 400 nm wavelength and 6 mW power, with a collimated spot diameter of 5 mm, was used to scan the entire module point-by-point while measuring the output current, at a constant module bias of 0 V. The measured photo-generated current at the module output is usually less than the photo-generated current at the light spot, as illustrated in Figure 2.6. This is due to the increase in module series resistance, arising from the shunt resistances of the dark cells, as well as shunt losses within the spot-illuminated cell. By plotting the photo-generated current as a function of position, the local distribution of photo-current in the module is mapped. The module point-illuminated I-V characteristics were also measured in order to quantify the short circuit current (I_{sc}) generated at different points on the module. Investigation of a striation ring feature using different laser wavelengths and light intensities was also done in order to explore the impact of the feature on photo-current under different conditions.

A photograph of the module and the corresponding LA-LBIC map are shown in Figure 6.1. There is a clear variation in photo-current produced by the different cells, as is indicated by the colour difference on the LBIC map.

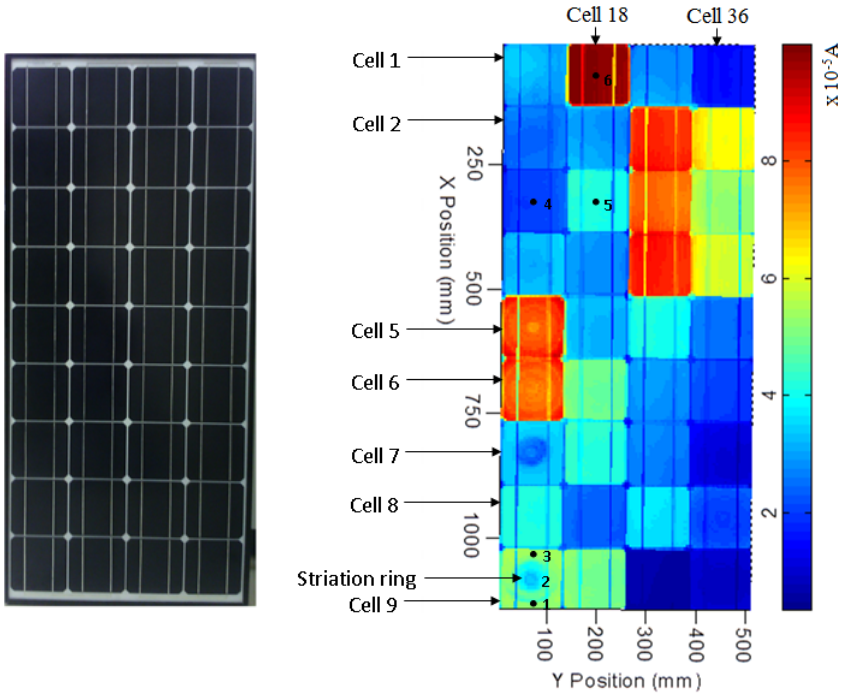

Figure 6.1: Mono-crystalline silicon PV module showing (a) Photograph (b) Short circuit LA-LBIC map under white light illumination.

6.3.1 Variations in photo-generated current

6.3.1.1 Between cells

In Figure 6.1, a variation in photo-generated current of about 100 μA is observed between the cells. Since the cells are connected in series, the current generated at a point in a cell has to flow through all the series and shunt resistances of all the other dark cells in the module before it is measured at the module output. The cells not being investigated are in the dark and are thus reverse biased, implying that current must flow through their shunt and series resistances, as shown in the point-illuminated circuit model of a PV module in Figure 6.2. It should be noted that each time the light spot is moved from cell to cell, the current continues to flow through all the series resistances of the cells as well as the shunt resistances of the non-illuminated cells, which contributes to the module series resistance.

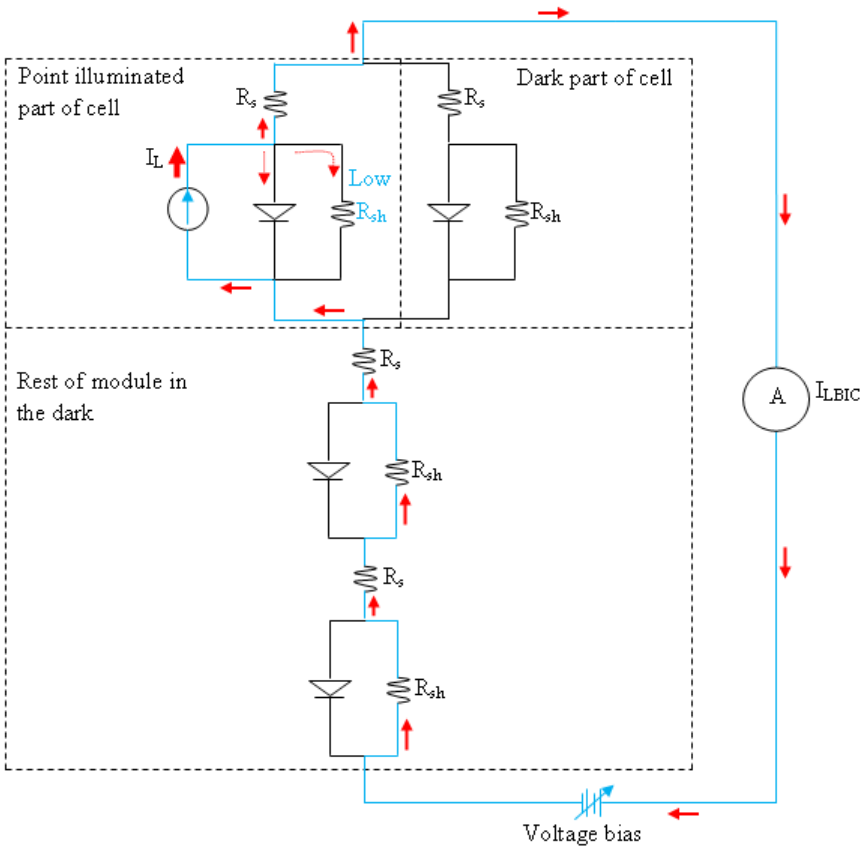

Figure 6.2: A point-illuminated circuit model of a PV module illustrating how the photo-current flows through the series-connected module cells.

The additional voltage drop in the series resistance, R_s, of the dark cells, arising from shunt resistances, R_{sh}, of the dark cells, forming the current path causes a reduction in the photo-current generated by the illuminated cell. The variation in photo-current between cells is therefore a result of the differences in the combined shunt and series resistances of the individual cells forming the module. If the shunt resistances of all cells are the same, the voltage drop of the cells in the dark would be constant irrespective of the light spot position. The manifestation of the variation of the photo-current between cells can thus be attributed to non-identical cell parasitic resistances as well as variation in the photo-current produced by individual cells.

Figure 6.2 illustrates that when the light spot is on a cell with a low shunt resistance, the measured module current will be reduced by shunting within the cell as well as series and shunt resistances of the non-illuminated cells. However, when a cell with a high shunt resistance is being scanned, the photo-generated current is mainly reduced by the effect of the series connected non-illuminated cells. Therefore, although scanning at short circuit cannot give a precise measure of the photo-current generated by individual spot-illuminated

cells in a module, it is useful for relative comparison of individual cell performances.

6.3.1.2 Across individual cells

The line scan shown in Figure 6.3 was extracted from the LA-LBIC map in Figure 6.1 at position y = 60 mm. It reveals that the photo-current across individual module cells varies significantly.

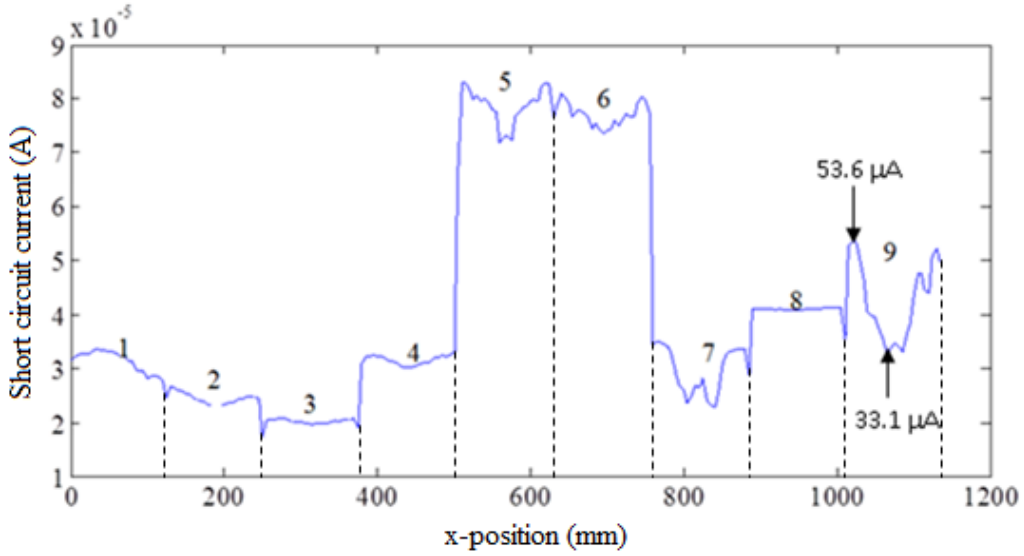

Figure 6.3: Line scan extracted from LA-LBIC map in Figure 6.1 at position y = 60 mm.

Except for cells 3 and 8 the rest of the cells show significant variations which are more pronounced in cells 5, 6, 7 and 9. For these cells, the high variation in photo-current observed is a result of the striation ring feature caused by the presence of oxygen precipitates in silicon wafers [36]. Figure 6.4 focuses on cells 7 and 9 highlighting the effect of the striation ring on photo-generated current.

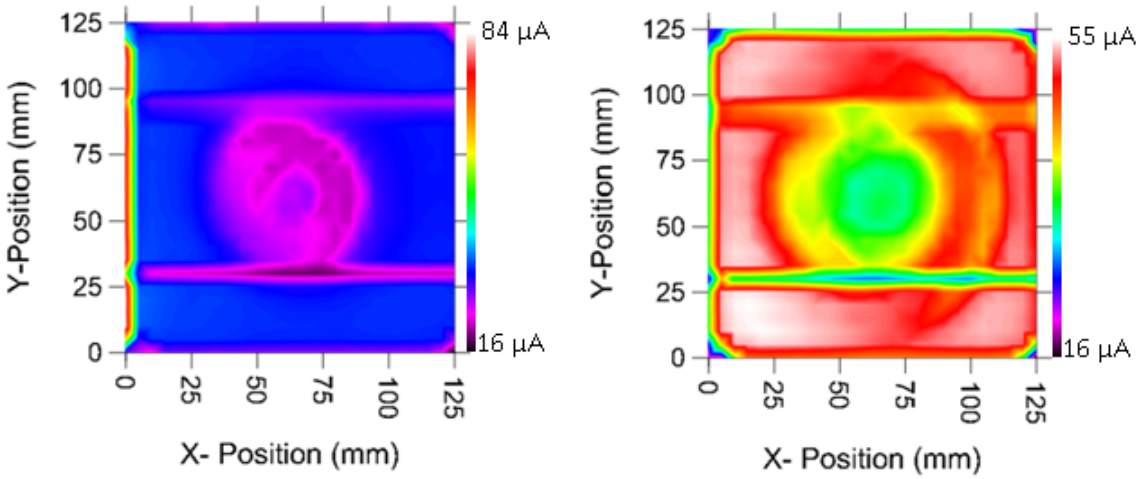

Figure 6.4: Magnified LA-LBIC map of (a) Cell 7 and (b) Cell 9 in Figure 6.1, showing the striation ring feature.

It is worth noting that the current limiting effect of the striation ring is highest at the centre of the cell and decreases radially outwards. This suggests that the concentration of the oxygen precipitate in the wafers is highest at the centre and decreases towards the edges. The counter rotation effect of the crucible and seed crystal during crystal growth appears to facilitate the movement of the oxygen dissolved from the crucible towards the centre of the growing crystal, leading to a higher concentration of oxygen at this location. Since the silicon wafers used to make solar cells still face the challenge of homogeneity in electrical properties [118], non-uniformity in photo-current within cells is likely. The striation ring feature in cell 9 resulted in a variation in the spot-illuminated module I_{sc} of 20.5 μA, as seen from the line scan in Figure 6.3.

When scanning within a cell, the effect of the series resistance of the cells in the dark remains constant and therefore any variation in photo-generated current across a cell can be imaged. The short circuit LA-LBIC photo-response map of a module cell therefore gives a true reflection of the variation in local performance within the cell.

When comparing the variation in photo-generated current between and across cells, note that the variation between cells is much higher than the variation across cells, e.g. cell 3 vs cell 6.

6.3.2 Module point I-V measurements

In order to quantify the photo-current of the module at given points, module point I-V characteristics were measured so that the I_{sc} could be determined. At each point, 50 sets of current and voltage values were measured in a period of 5 seconds. Due to the short measurement time, no significant heating of the module by the laser is expected. Consider Figure 6.1, point I-V curves were obtained from within the same cell (points 1 to 3 on the module) and from different cells (points 4 to 6 on the module). These I-V curves are presented in Figure 6.5. In both cases, it can be noted that different points within a module operate at different I_{sc} and V_{oc}. The variations in module I_{sc} and V_{oc} under point illumination between cells, were investigated in cells 3, 16 and 18 at points 4, 5 and 6, respectively. The best performing point in this group is in cell 18, which shows a point-illuminated module I_{sc} of 10×10^{-5} A and V_{oc} of 0.21 V, while the worst performing point is in cell 3, with a point-illuminated module I_{sc} of 2.1×10^{-5} A and V_{oc} of 0.05 V. Within cell 9, at points 1, 2 and 3, a small drop in point-illuminated module I_{sc} from 5.54×10^{-5} A to 3.41×10^{-5} A occurs at the striation ring, while V_{oc} drops from 0.13 V to 0.08 V. It is noted that a drop in point-illuminated module I_{sc} of 21.3 μA at the striation ring is greater than that from the dark LA-LBIC of 20.5 μA shown in Figure 6.3. This occurs because, during dark LBIC, the cell under investigation becomes forward biased as illustrated in Figure 2.3, causing it to operate at a current lower than its actual point-illuminated module I_{sc}. The module point I-V measurements show that the variation in point-illuminated module I_{sc} and V_{oc} is higher between cells than within cells.

The high variation in photo-current between cells is indicative of high variations in the shunt resistances of the individual cells making up the module, as shown by the equivalent circuit model of a point-illuminated module in Figure 6.2. When a module cell has a relatively high shunt resistance, the reduction in module I_{sc} caused by the shunt resistances of the non-illuminated cells, which become active series resistances, is lower, compared to a module cell with a low shunt resistance.

The variation in photo-current that exists within cells is usually due to the presence of defects in the cells. Due to the non-uniform distribution of defects, the recombination of charge carriers within a cell also varies, and as a consequence the photo-generated current varies within a cell. However, since the effect of the shunt resistances of non-illuminated cells remains fairly constant during measurements within a cell, little variation in I_{sc} occurs compared to measurements between cells.

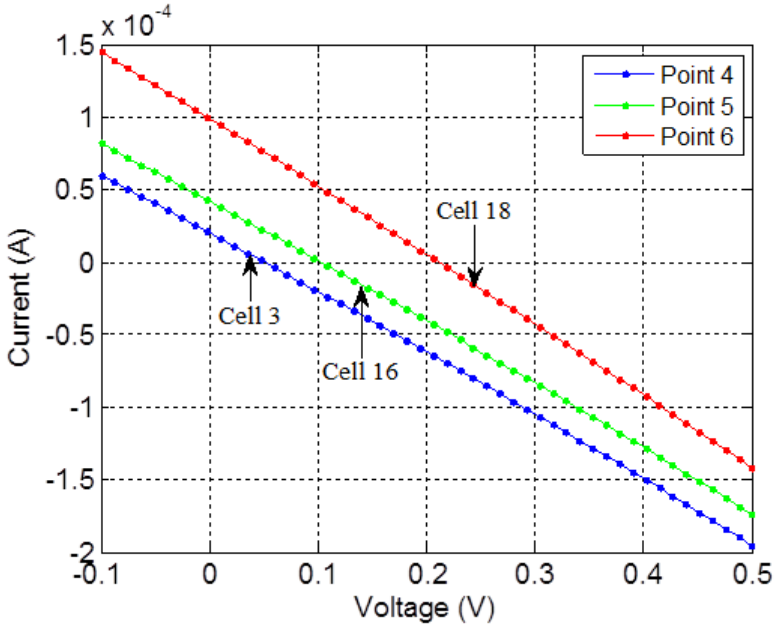

(a)

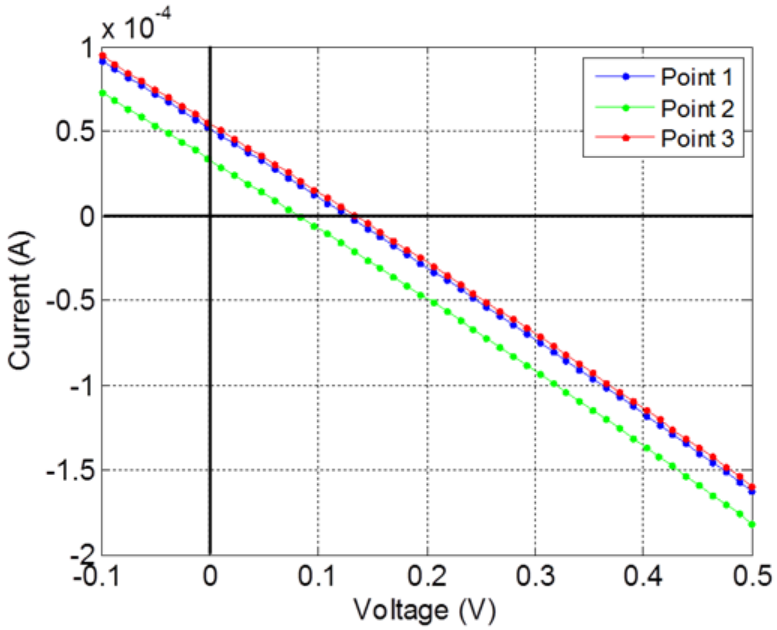

(b)

Figure 6.5: Mono-crystalline silicon point-illuminated module I-V curves (a) For cell 3, 16 and 18 (b) Within cell 9.

The variation in point-illuminated module I_{sc} as seen in Figure 6.5, is explained using the equivalent circuit model of a point-illuminated module, as demonstrated in Figure 6.6.

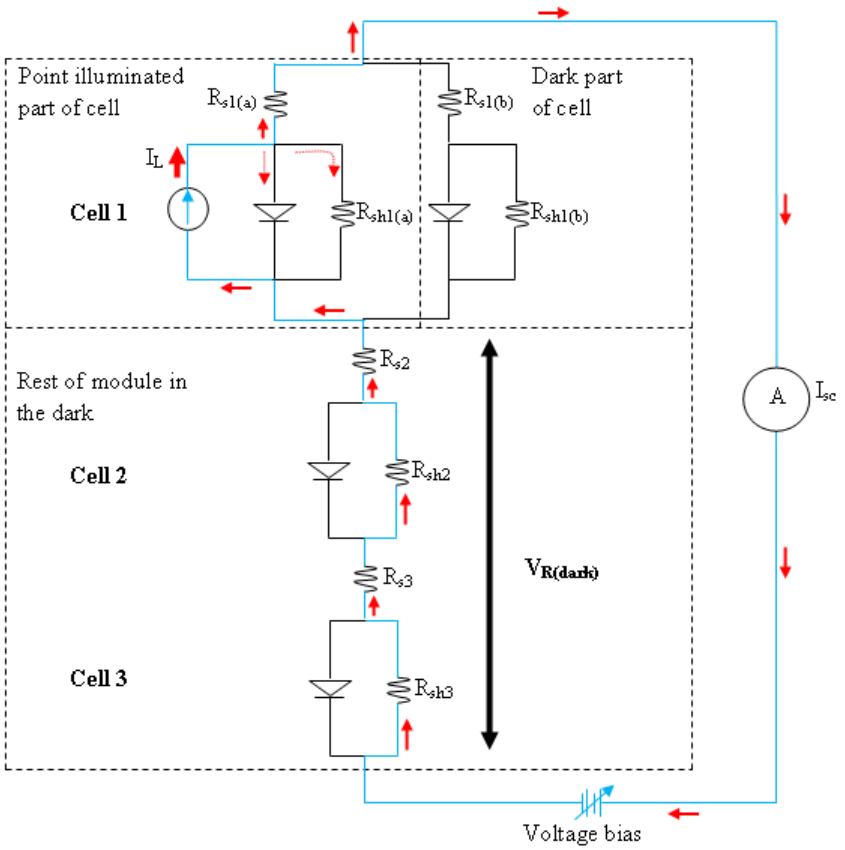

Figure 6.6: Effect of shunt resistances of module cells on the module short circuit current under point illumination.

The module in this case is considered to be made up of three series-connected cells with shunt resistances R_{sh1}, R_{sh2}, R_{sh3} and series resistances R_{s1}, R_{s2} and R_{s3}, respectively. When the module is point-illuminated, the current generated at the laser spot has to flow through all the series-connected cells before it is measured at the module output. When the light spot is moved from cell to cell, the flow of current through the series resistances of the cells constituting the module remains almost constant. Each time a cell is point-illuminated, current leakage through its shunt resistance may occur while the shunt resistances of the non-illuminated cells become active series resistances, causing a significant voltage drop, $V_{R(dark)}$, which reduces the photo-generated current as well as the module voltage. If, for instance, R_{sh1} is relatively large compared to R_{sh2} and R_{sh3}, the voltage drop due to the dark cells would be small compared to when R_{sh1} is relatively small in relation to R_{sh2} and R_{sh3}. Therefore, the module current generated by point illumination of each cell is directly related to its R_{sh}. The voltage drop due to the non-illuminated cells, $V_{R(dark)}$, when a cell is point-illuminated is inversely proportional to the cell R_{sh} and reduces the module voltage accordingly. Therefore, for a cell with high R_{sh}, $V_{R(dark)}$ is small, causing a small reduction

to the module voltage, and so the effective module voltage under point illumination remains high. In general, the point-illuminated module current and voltage of a cell is directly proportional to the cell R_{sh}. Since the shunt resistances of module cells are likely to vary due to the presence of defects and improper cell sorting, large variations in point-illuminated module current and voltage between cells is not unusual.

When a point-illuminated module is at V_{oc}, the voltage drop across the dark cells, $V_{R(dark)}$, is zero, as no current flows through them. The current generated by the point-illuminated cell can therefore only forward bias the pn junction or flow through the shunt resistance of the illuminated portion of the cell, $R_{sh1(a)}$, as shown in Figure 6.7. The current flowing through $R_{sh1(a)}$ develops a voltage across the module, i.e. the point-illuminated module V_{oc}. It should be noted that $R_{sh1(a)}$ of the illuminated part is in parallel with the $R_{sh1(b)}$ of the rest of the dark part of the cell and hence the voltage across them is the same. The V_{oc} of the point-illuminated module is therefore directly related to the shunt resistance of the illuminated part of the cell. Since little variation occurs in R_{sh} across a cell, point-illuminated module V_{oc} tends to remain constant across a cell. However, when a cell has a defect, as seen in Figure 6.5(b), V_{oc} at the point is significantly reduced.

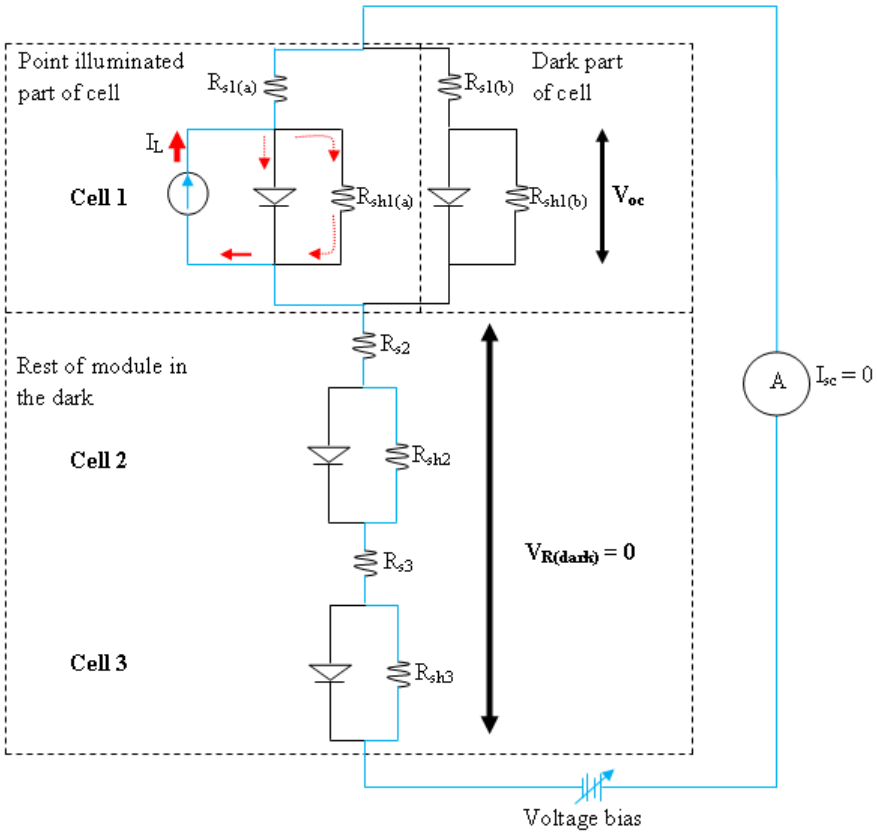

Figure 6.7: Effect of shunt resistances of module cells on the module open circuit voltage under point illumination.

6.3.3 Striation ring feature

6.3.3.1 Impact of striation ring feature on photo-current, at different light wavelengths

Cell number 9 in Figure 6.1, with the striation ring feature was scanned using 448 nm, 660 nm and 785 nm wavelength lasers with the power set at 2.5 mW and a spot diameter of 1 mm. The LA-LBIC maps are shown in Figure 6.8. Striation rings originate from the inclusion of oxygen precipitates in silicon during the Czochralski manufacturing process [9].

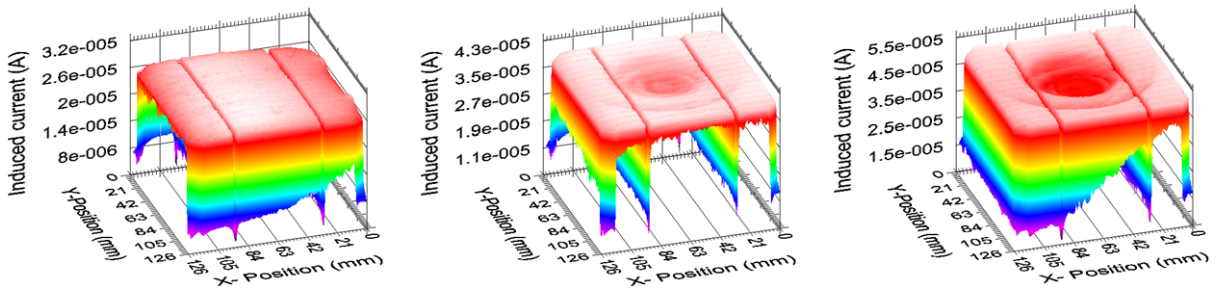

(a) 448 nm wavelength **(b)** 660 nm wavelength **(c)** 785 nm wavelength

Figure 6.8: 3-D LA-LBIC map of cell 9 in Figure 6.1, with the striation ring feature scanned using different laser wavelengths.

The striation ring feature appears to be active deep in the bulk of the cell material, and has no detrimental effect on photo-generation near the surface. n-type silicon is reported to be more tolerant to defects and impurities than p-type [119, 120, 121, 122], and this could be the reason why the striation ring feature is inactive to the high energy photons. During the pn junction formation, phosphorus diffusion into the silicon wafer to form the emitter layer reduces the recombination effect of the oxygen precipitate in the emitter [71], making it less prone to photo-current loss compared to the base. Therefore, by varying the wavelength of the probing laser beam, the LBIC technique can be used to investigate bulk and surface defects [123].

In order to conveniently compare the effect of the striation ring feature on the photo-current, as a function of incident light wavelength, line scans were extracted at position x = 62 mm from the LA-LBIC maps in Figure 6.8 and the results are shown in Figure 6.9.

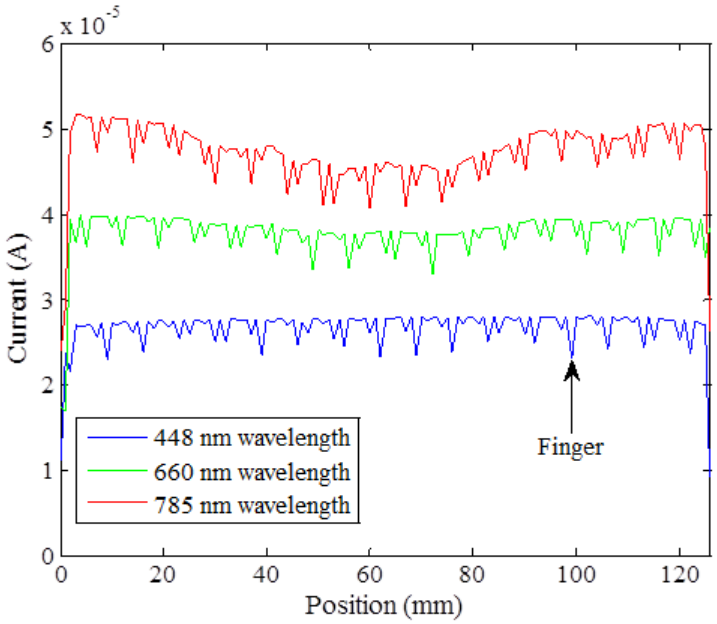

Figure 6.9: Line scan extracted at position x = 62 mm from the LA-LBIC maps in Figure 6.8.

The photo-current generated increases with increase in wavelength as seen in Figure 6.9 and this is typical of the spectral response of mono-crystalline silicon solar cells which increase up to a wavelength of 890 nm, before declining sharply [124]. The short wavelength photons are absorbed close to the cell surface and some of the generated charge carriers recombine due to surface recombination, giving a low relative photo-response. The 660 nm and 785 nm wavelengths show a higher photo-response because the charge carriers are generated over a greater depth compared to the 448 nm wavelength.

6.3.3.2 Impact of striation ring feature on photo-current, at different light intensities

The results presented in Figure 6.10 are line scans across cell 9 at varying light intensities, using the 785 nm wavelength laser. The light intensity was varied by changing the laser power. The line scan at 1 mW laser power is plotted separately so that the effect of the striation ring on I_{sc} can be clearly observed. The dotted lines in Figure 6.10 indicate the points at which I_{sc} were obtained for the different laser powers.

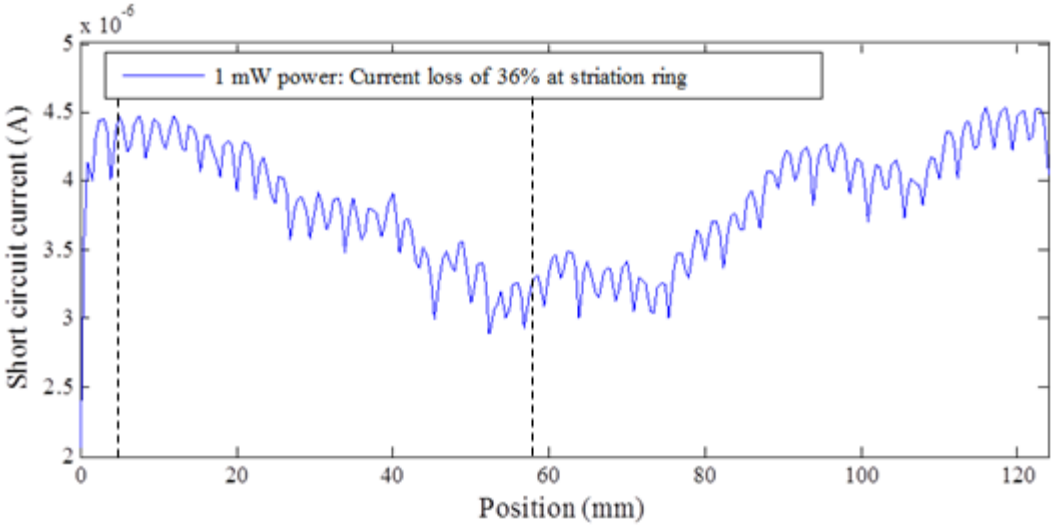

(a) Laser power of 1 mW.

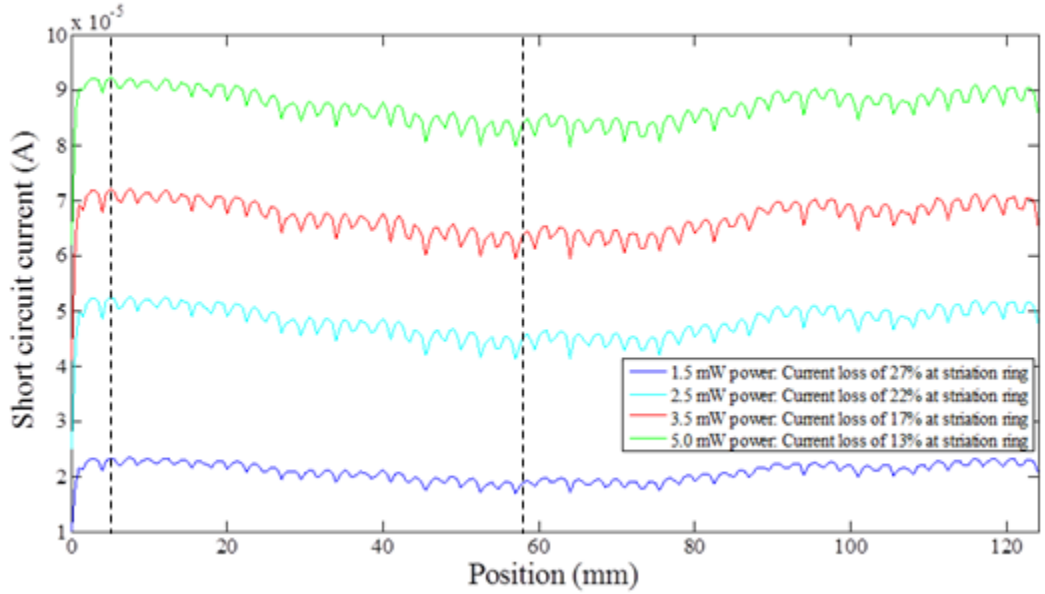

(b) Laser power of 1.5 - 5.0 mW.

Figure 6.10: Line scans on cell 9 under different laser powers.

When the laser power is increased, more photons are produced leading to an increased number of photons available for absorption, hence an increase in short circuit current. In order to compare the effect of the striation ring on I_{sc} under varying laser powers, the percentage drop in I_{sc} was calculated by using I_{sc} values at the highest and lowest points on the line scans. The percentage drop in I_{sc} due to the striation ring feature is highest at low laser powers and reduces with an increase in laser power. At a laser power of 1 mW, the feature causes a reduction in short circuit current of 36%, while at 5 mW, I_{sc} reduces by

13%. Fewer charge carriers are generated at low laser power, meaning that any loss of these carriers becomes more significant compared to the loss experienced under high laser power. Therefore, the percentage reduction in I_{sc} at the feature is high at low power and decreases as the laser power increases.

Figure 6.11 compares I_{sc} within the striation ring to I_{sc} in the same cell that is same distance from the ring. These I_{sc} values are plotted as a function of laser power, and were extracted from Figure 6.10 at position 5 mm and 58 mm as indicated by the dotted lines. It is clear that short circuit current increases as laser power is increased for both regions. It can be seen that, within the range of the laser power used, I_{sc} is directly proportional to laser power, and this indicates that the cell material has not been saturated by the illuminating laser. At 1 mW power, the percentage drop in I_{sc} is 27 % while at 5 mW it reduces to 8.9%. The reason for this is as explained above.

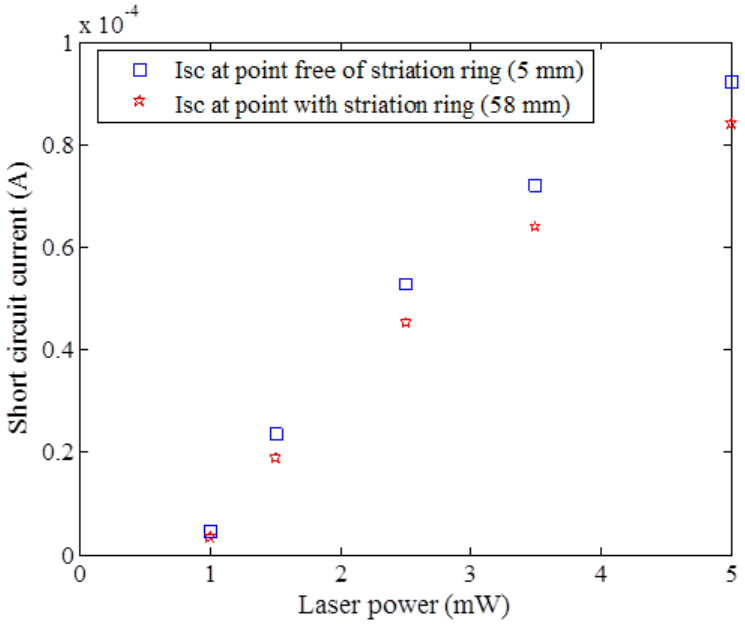

Figure 6.11: Short circuit current as a function of laser power extracted from Figure 6.10 along the dotted lines at 5 mm and 58 mm at the striation ring free area and the area of the cell with striation ring, respectively.

6.3.4 Comparing c-Si module LA-LBIC map and EL image

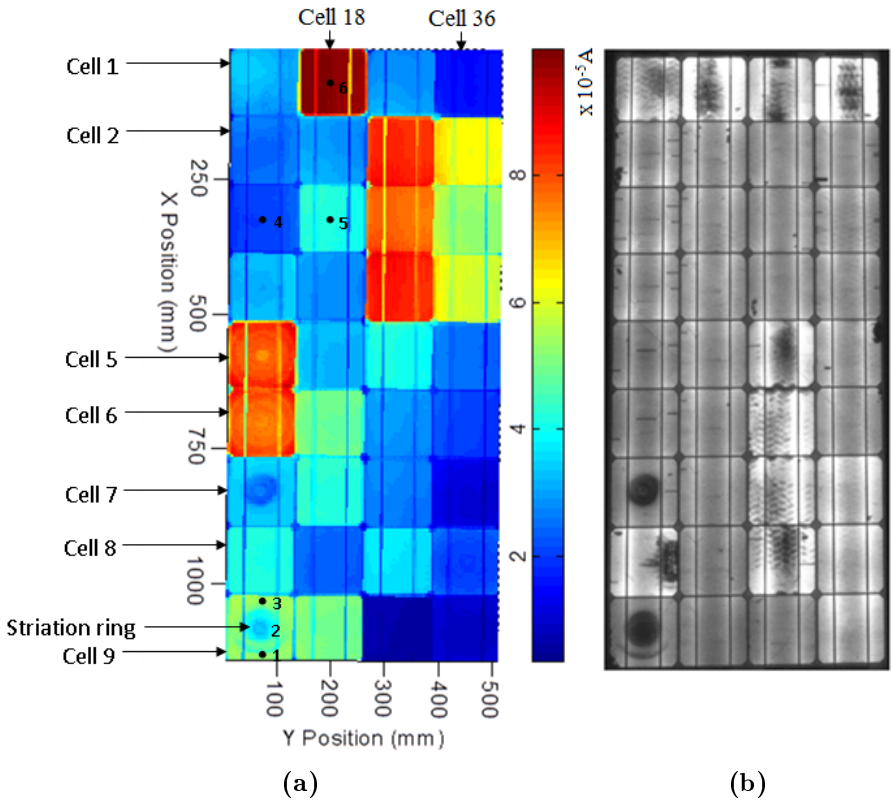

Figure 6.12: Mono-crystalline silicon PV module showing (a) LA-LBIC map (b) EL image.

The LA-LBIC map and the EL image of c-Si module are shown in Figure 6.12. While the LA-LBIC map clearly distinguishes between the individual cell currents, which is useful for identification of cells with high and low photo-current, the EL image does not. This suggests that the LA-LBIC technique is more sensitive to photo-current variations in a module than the EL technique. Quantification of the current generated by each cell is therefore possible by extracting the current values from the LA-LBIC map. The bus bars are clearly observed in both the LA-LBIC map and EL image, while the fingers which are not visible in the EL image are distinctly seen in the high resolution LA-LBIC line scans shown in Figure 6.9. The bus bars and the fingers block the incident light from reaching the cell material during LA-LBIC scanning and as a consequence they appear as regions with low photo-current. The bus bars in the EL image appear as dark regions because they block the emissions of the luminescence photons arising from radiative recombination of the electrically generated charge carriers. The EL image and the LA-LBIC map show striation rings in cells 7 and 9, but those appearing in cells 5 and 6 in the LA-LBIC map are absent in the EL image.

Some of the charge carriers generated by forward biasing of the module during the EL measurement recombine at the striation ring, reducing the number of charges undergoing radiative recombination and consequently reducing the EL intensity. It appears that the deposits of oxygen precipitates in cells 5 and 6 are too low to cause any measurable change in luminescence due to radiative recombination within these cells, hence the striation rings are not visible in the EL image. However, the LA-LBIC technique appears to detect the change in module I_{sc}, arising from the small traces of oxygen precipitates within these cells, thereby making the feature visible. From this analysis, it can be inferred that the LA-LBIC technique is more sensitive in detecting the striation ring feature in PV modules than is the EL technique.

6.4 Multi-crystalline silicon (mc-Si) PV module

This module consists of 12 series-connected cells and the manufacturer's specifications at STC are shown in Table 6.2.

Table 6.2: Manufacturer's STC performance parameters for the mc-Si module.

Performance parameters	P_{max}(W)	V_{mp}(V)	I_{mp}(A)	V_{oc}(V)	I_{sc}(A)
Values at STC	1.0	6.0	0.17	7.2	0.34

Due to the small size of the module, the entire module was conveniently scanned with laser light (633 nm, 2 mW). In order to obtain the desired spot size, a metallic aperture of the desired diameter was fixed at the laser diode exit. By using the aperture to customise the spot diameter, the beam intensity is reduced as the aperture blocks part of the laser beam. Scanning was done point-by-point while measuring the module output current. The photo-response map was generated by plotting the measured current as a function of position. Detectable LA-LBIC features in the photo-response map include variations in current between and within cells, high current at localised points on the bus bar, and cell separation and cracks in the cell material, fingers and the bus bar. Quantification of point-illuminated module I_{sc} at different points on the module was done through module point I-V measurements, in order to compare variations in point-illuminated module I_{sc} between and within cells. The effects of different light wavelengths on photo-generated current was also investigated Finally, the module parameters were measured under Standard Test Conditions (STC), compared with the manufacturers specifications and the findings related to the LA-LBIC results.

Figure 6.13 shows a photograph of the module and the cell numbering as they appear in the LA-LBIC maps and EL images in the following sections.

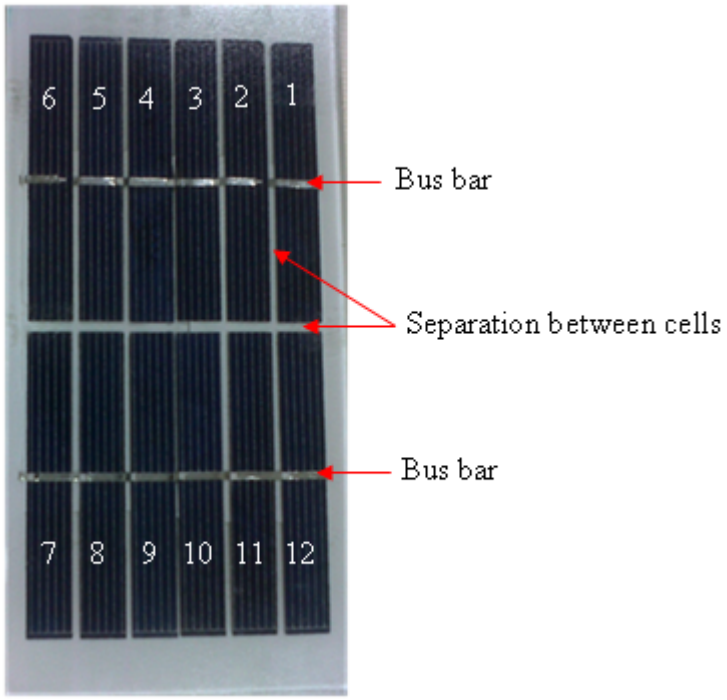

Figure 6.13: Multi-crystalline silicon PV module showing a Photograph and cell position as they appear in the LA-LBIC maps and EL images.

The entire mc-Si PV module was scanned at short circuit using a laser of 633 nm wavelength. The beam spot diameter was reduced to 1 mm using an aperture which reduced the laser power to 1.5 mW. The LA-LBIC photo-response map is presented in Figure 6.14. The variations observed in photo-current will be discussed in the following sections.

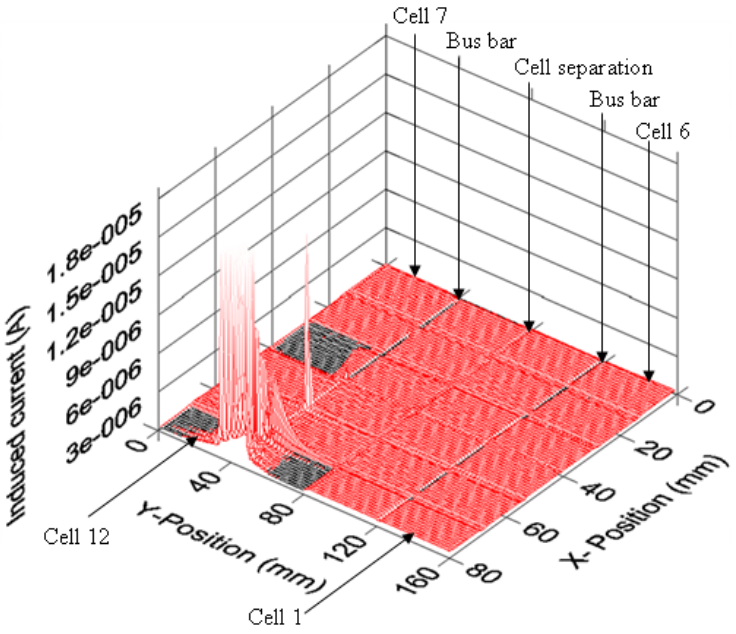

(a)

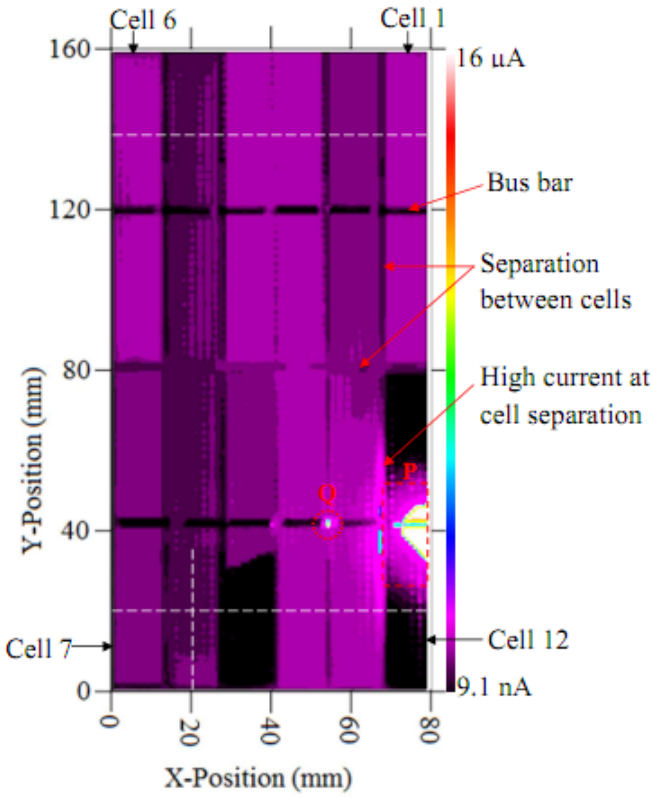

(b)

Figure 6.14: (a) 3D and (b) 2D short circuit LA-LBIC map of multi-crystalline silicon PV module under laser illumination. Q is a region on the bus bar, with a high current, while P is an area of a cell 12, with a triangular-shaped crack.

6.4.1 Variations in photo-generated current

6.4.1.1 Between cells

The variation in photo-current between cells can be seen by magnifying the regions in the module cells 1 to 6 in Figure 6.14, as shown in Figure 6.15.

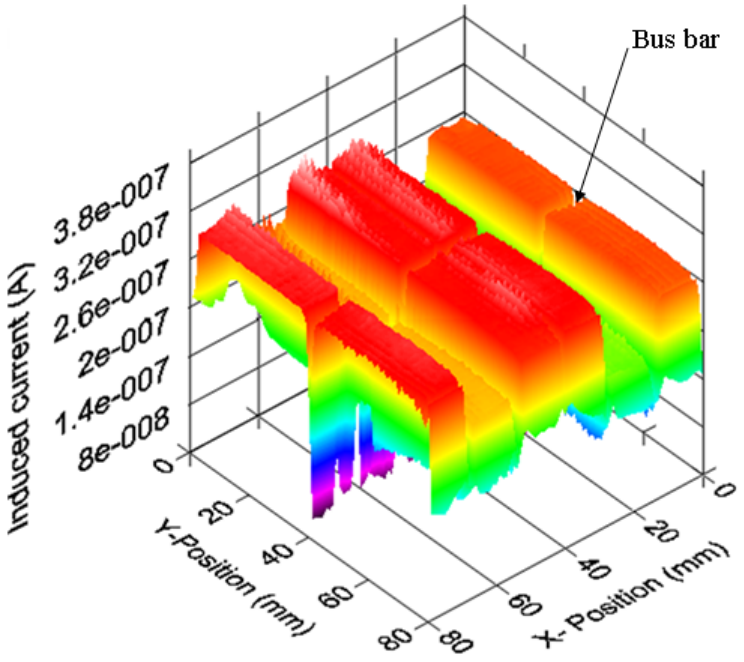

Figure 6.15: Magnified view of cells 1-6 in Figure 6.14 showing variation in photo-current between cells.

In order to quantify the variation in photo-current between cells, a line scan was extracted from Figure 6.14 along the white dotted line at position y = 140 mm. The extracted line scan is shown in Figure 6.16, indicating the variation in photo-current between the highest and the lowest performing cell as 0.11 μA.

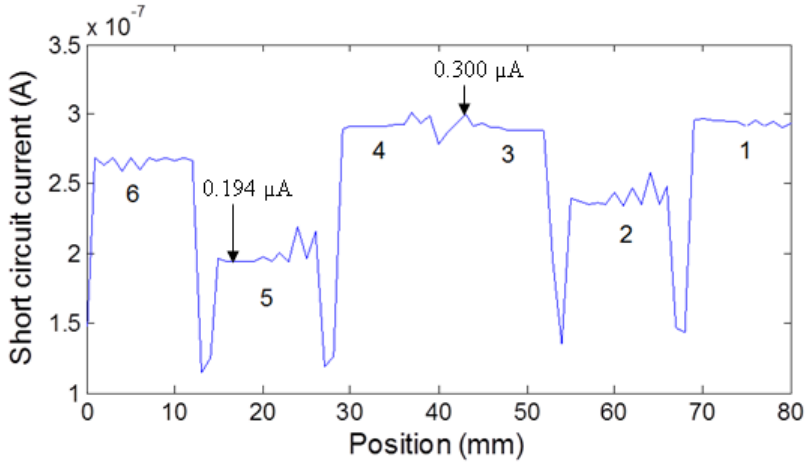

Figure 6.16: Line scan extracted from Figure 6.14 at position y = 140 mm, showing photo-current variation between module cells.

A variation in the photo-current between cells results when the cells have non-identical shunt resistances. The underlying cause for this, in mc-Si modules, is similar to that of c-Si modules as explained in section 6.3. Variation in the photo-current at different points on module cells can also be quantitatively compared by use of module point I-V measurements, as discussed later in section 6.4.3

6.4.1.2 Within cells

The variation in photo-current is investigated in cell 2 in Figure 6.14 by extracting a line scan along the dotted white line at position x = 60 mm. The extracted line scan is presented in Figure 6.17, and shows a maximum variation in photo-current of 0.05 μA.

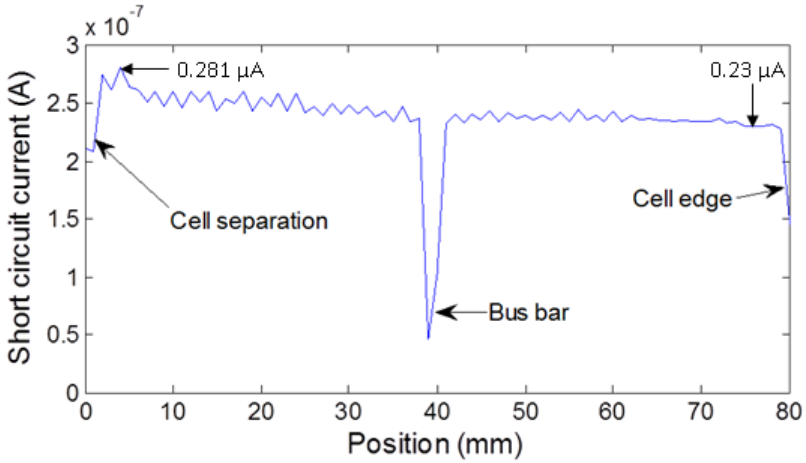

Figure 6.17: Line scan extracted from Figure 6.14 at position x = 60 mm, showing photo-current variation within module cell 2.

It should be noted that photo-current variation within cells is comparatively less than that between cells, with the exception of cells with cracks. The high variation in current within cells 9 and 12 is as a result of the cracks which disconnect the fingers, and hence the photo-generated current is not collected by the bus bar. The smaller variation in photo-current within a cell compared to that between cells is therefore an indication that the variation in shunting levels within cells is lower than between cells.

6.4.1.3 At localised points on the bus bar and cell separation

The LA-LBIC map in Figure 6.14 shows a high current at the bus bar at position marked Q and also at the separation between cell 11 and cell 12, close to the lower bus bar. The area Q in Figure 6.14(b) is magnified to highlight the high current generated at the point on the bus bar and is shown in Figure 6.18.

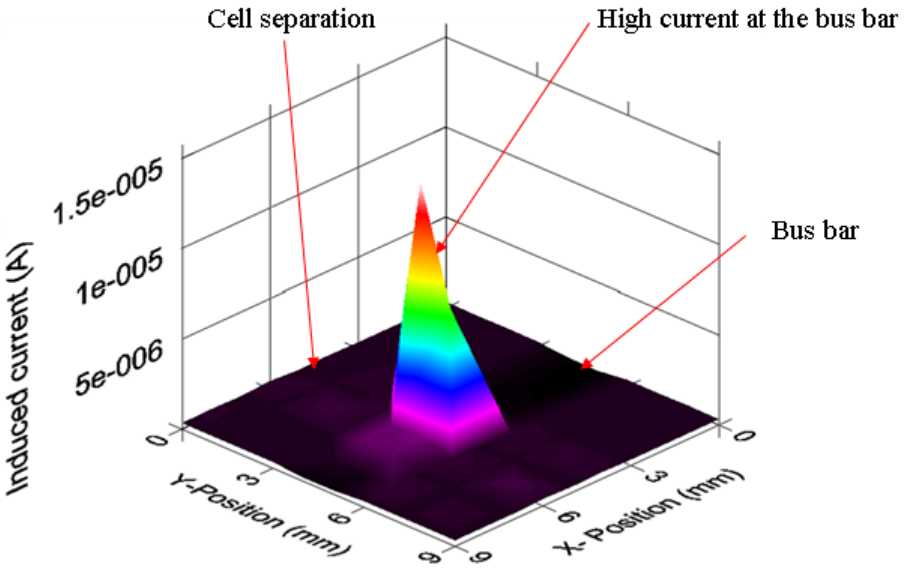

Figure 6.18: Magnified view of area Q in Figure 6.14, showing a high current at a point on a bus bar

Generation of current at the bus bar and cell separation is usually not expected because the bus bar blocks the light from reaching the cell absorbing material, while cell separation is a region devoid of the active cell material. The high current resulting at both locations is a result of light striking an irregular surface. This leads to diffuse reflection of the incident beam onto the top glass, which subsequently reflects the light rays back onto the active solar cell material. The light ray reflected onto the active cell surface is absorbed, leading to current generation. With a number of rays being reflected this way, a high current is

generated at point Q on the bus bar and at the separation between cells 11 and 12 in Figure 6.14. A ray of light being diffusely reflected is illustrated in Figure 6.19.

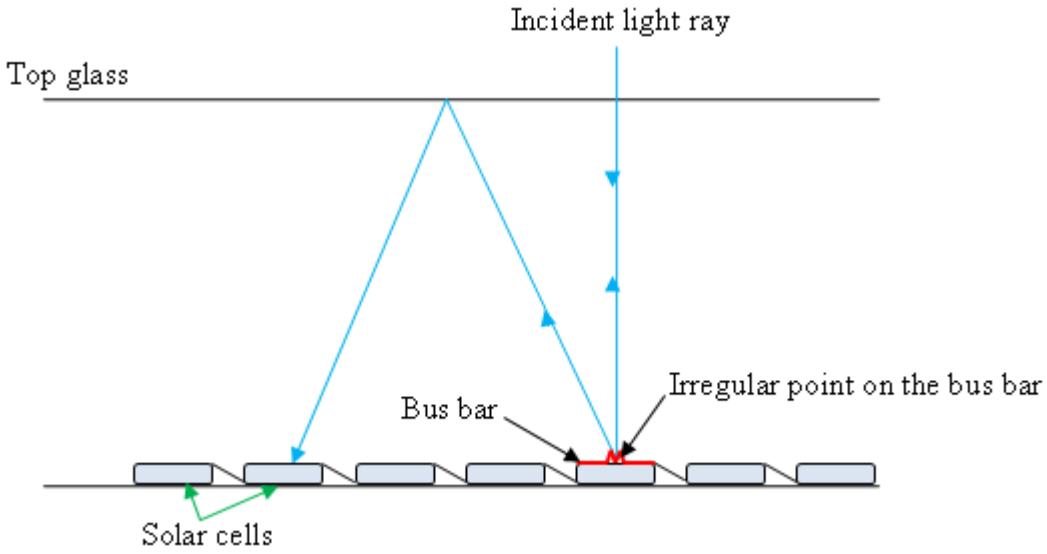

Figure 6.19: Illustration of multiple reflection of the incident light beam resulting from diffuse reflection of the incident light beam at irregular points on the bus bar or cell separation, leading to a high current generated at the point.

6.4.2 Cracks

The LA-LBIC image in Figure 6.14 shows cracks affecting cells 9 and 12. In order to explore the effect of the crack on the photo-current of cell 12, the area marked P in Figure 6.14(b) was scanned at a high resolution using a 660 nm laser with a spot diameter of 0.5 mm. The LBIC map is shown in Figure 6.20.

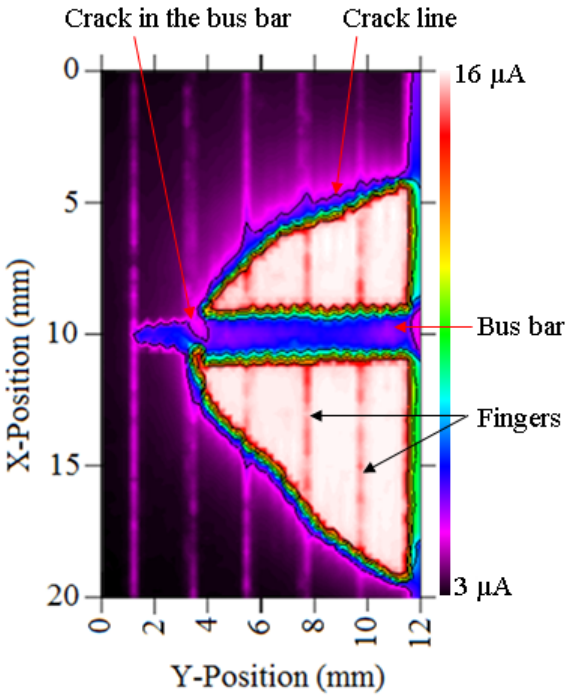

Figure 6.20: Photo-response map of area P in Figure 6.14(b), scanned using a 660 nm laser with a spot diameter of 0.5 mm

Cracks electrically isolate the cell material as well as the fingers, with the portion attached to the bus bar able to deliver current, while the part detached from the bus bar generates current which is not delivered to the bus bar. The crack in Figure 6.20 is V-shaped, allowing only the current generated within the V-shape to be collected, while the other areas of the cell remain disconnected. A crack is also visible in the bus bar attached to the V-shaped portion, at the soldering point, leaving only a small strip for continuity. This crack appears to arise from improper soldering during cell stringing, leaving a gap in the solder. The origin of most cell cracks in silicon solar cells have been linked to the soldering process during cell stringing [57, 59, 58]. During the cooling process after soldering, the copper wires contract more than the silicon and the associated thermo-mechanical stress may cause cracks in the silicon as well as in the metallisation [60].

6.4.3 Module point I-V measurements

Module point I-V measurements were taken at the centre of each cell along the dotted horizontal lines shown in Figure 6.14(b), using a 633 nm wavelength laser with no aperture fixed at the beam exit. These are presented in Figure 6.21(a). Measurements were also taken along the vertical dotted line in cell 8 (x = 20 mm) to investigate homogeneity

in photo-current within a cell. These I-V curves are presented in Figure 6.21(b). Since little variation in photo-current occurs within a cell, as can be seen in Figure 6.17 and Figure 6.21(b), the point-illuminated module I-V characteristics at a point within a cell can be assummed to be representative of the cell I-V characteristic. A greater variation in point-illuminated module I_{sc} and V_{oc} occurs between cells than within cells, as it is evident in Figure 6.21. The point-illuminated module $I_{sc} = 1.6\ \mu A$ and $V_{oc} = 0.22$ V for cell 1 is the highest in the group while the cracked portions of cells 9 and 12 generate hardly any current and voltage. The point-illuminated module I_{sc} on the cracked part of cell 9 is 63 nA while $V_{oc} = 6$ mV. The fact that the cracked part of the cell is still able to generate some current and voltage suggests that some of the fingers have not been completely disconnected and are therefore able to deliver some current to the bus bar. The wide variation in current generated by the cells, which has been amplified by the presence of the cracks, makes the module vulnerable to current mismatch. This leads to a lower module power output, as the weakest cell is the one that determines the module current [6]

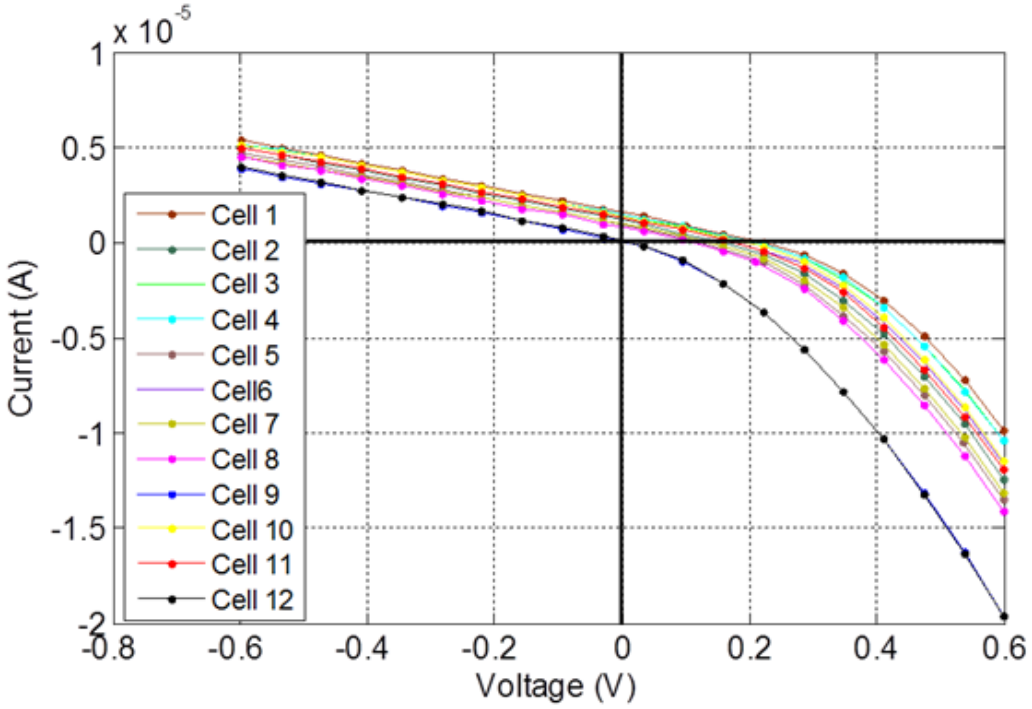

(a)

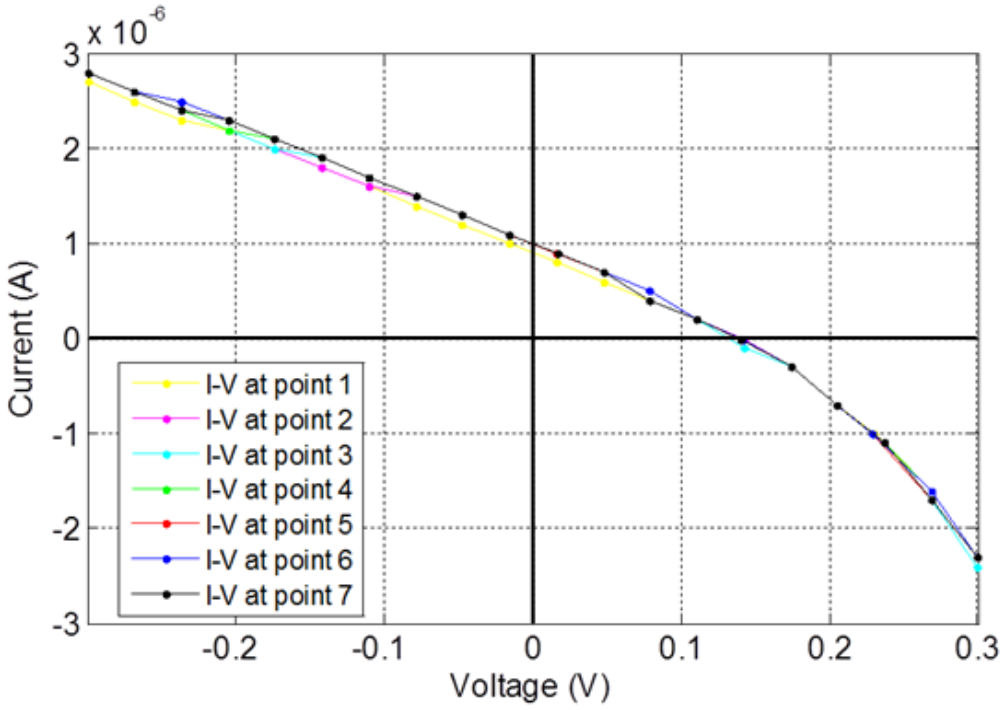

(b)

Figure 6.21: Multi-crystalline silicon point-illuminated module I-V curves (a) For 12 module cells (b) Within cell 8.

6.4.4 Effect of different wavelengths of light on photo-generated current

The application of the LA-LBIC technique to investigate the dependence of photo-generated current on the wavelength of the incident light is presented in this section. The short circuit current at different laser wavelengths as a function of position for cells 7 to 12 is shown in Figure 6.22.

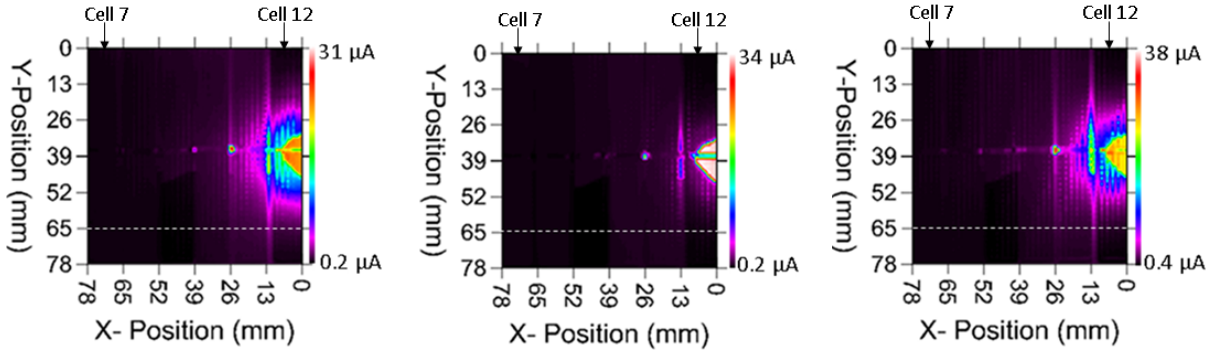

(a) 448 nm wavelength. **(b)** 660 nm wavelength. **(c)** 785 nm wavelength.

Figure 6.22: The I_{sc} maps of cells 7 to 12 under illumination by different laser wavelengths, all set at 5 mW power.

In order to compare the variation in I_{sc} as a function of position under illumination by the different laser wavelengths, line scans were extracted at position y = 65 mm from each of the maps in Figure 6.22 and the results are shown in Figure 6.23. For the cells without cracks, the 785 nm laser wavelength generates the highest current, while the lowest current is generated by the 448 nm laser wavelength. Wavelengths of less than 500 nm are mostly absorbed in the emitter region of the solar cell [125] and this makes the generated charge carriers prone to surface recombination, consequently leading to a low I_{sc}. The low energy wavelengths, however, penetrate deeper into the solar cell material and generate charge carriers which are not vulnerable to surface recombination, hence the high I_{sc}. Low energy photons are absorbed more homogeneously throughout the volume of the solar cell material [118]. For cell 9 and cell 12 which have cracks, it can be noted that the point illuminated module I_{sc} generated by the 448 nm wavelength exceeds that of 660 nm and approaches that of 785 nm wavelength. This change in the trend could be due to the negative effect of the crack on the photo-generated current. Micro-cracks act as electrical recombination centers and can reduce the diffusion length of minority charge carriers by up to 50% [67]. In general, the charge carriers generated by the 448 nm wavelength are close to the solar cell surface and

suffer more from surface recombination, but less from the recombination effect of the crack, since the generation point is close to the pn junction. However, for the low energy photons, the charge carriers are generated in the bulk of the solar cell and have to flow a long distance, parallel to the crack before collection by the pn junction. This long journey in the vicinity of the crack (recombination centre) leads to a substantial reduction in the number of minority carriers and hence a low I_{sc}. The recombination effect of the crack seems to override surface recombination, causing the 488 nm wavelength to generate more current than the 660 nm. It is worth noting that the crack in cell 9 is more severe than that in cell 12, when considering the I_{sc} generated by the two cells. The crack in cell 9 extends across the entire cell while that in cell 12 leaves one or two fingers unaffected.

In Figure 6.23, much larger variations in photo-current within cells are observed at higher wavelengths compared to shorter wavelength (448 nm). Wavelengths of less than 500 nm are mostly absorbed in the emitter [125] which is a single layer of PV material, therefore, little variation in photo-current is expected. However, higher wavelengths are absorbed throughout the volume of the solar cell material [118], which includes two different layers of PV material (emitter and base). With increase in penetration depth, higher variation in photo-current may occur, since as the thickness of the PV material increases it may become less homogeneous. From these results, it can be inferred that, variation in photo-current within a cell increases as the wavelength of the incident light is increased.

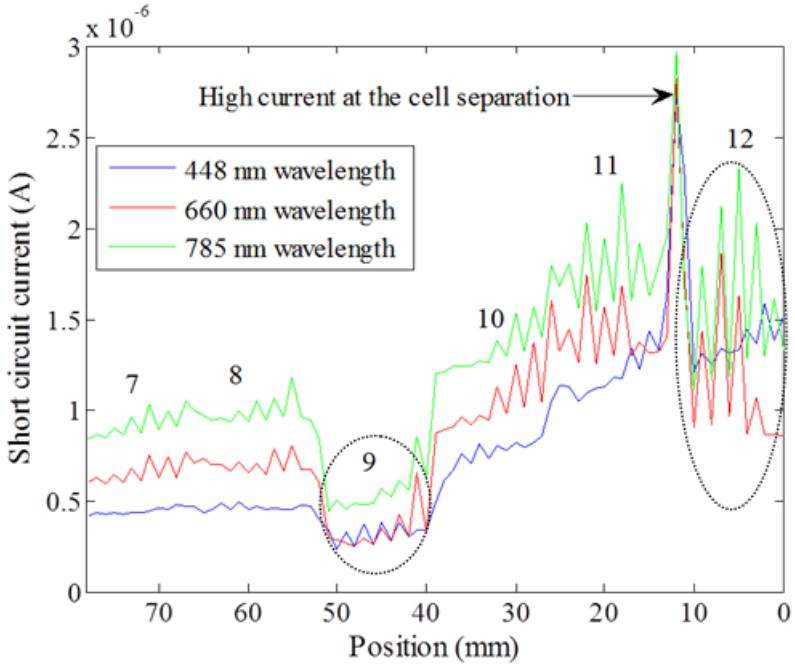

Figure 6.23: Line scans extracted at position y = 65 mm in Figure 6.22, showing how I_{sc} varies with position for different light wavelengths.

To illustrate how the I_{sc} varies with the laser wavelengths, I_{sc} values at selected points were extracted from Figure 6.22 at position y = 65 mm and the results are shown in Figure 6.24. Cells 7, 8, 10 and 11 show a higher I_{sc} at 660 nm than at 448 nm wavelength, which is consistent with the spectral contribution to I_{sc} of mc-Si solar cells [126]. However for cells 9 and 12, as explained, a drop in I_{sc} is observed from 448 nm to 660 nm wavelength.

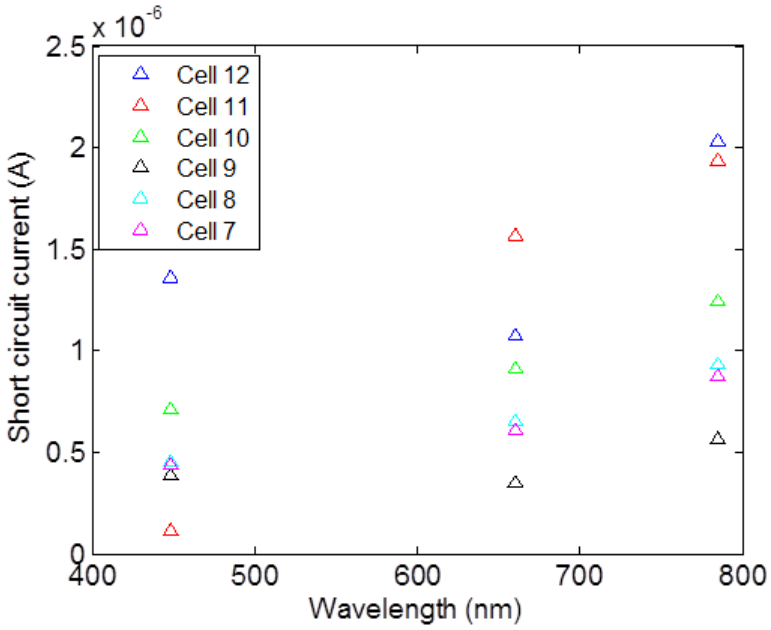

Figure 6.24: Variation of I_{sc} as a function of wavelength extracted from Figure 6.22 at points (3,65), (20,65), (35,65), (45,65), (60,65) and (72,65).

6.4.5 Module I-V characterisation

The current-voltage characteristic of the mc-Si module under Standard Test Conditions (STC) is shown in Figure 6.25. By considering the slopes projected at I_{sc} and V_{oc}, no significant effect from shunting is observed. However, the series resistance appears slightly increased, probably as a consequence of the broken fingers and a crack in the bus bar. Cracks cause an increase in series resistance and consequently a reduction in short circuit current [64]. A step is also noticed below the knee of the I-V curve, which is typically a manifestation of current mismatch in the module [105]. Current mismatch causes a change in the shape of the I-V curve [5] and in this particular case it is due to the presence of cracks which disconnect portions of the cells. When the module cells generate different currents, it is the worst performing cell that determines the module output current. [127].

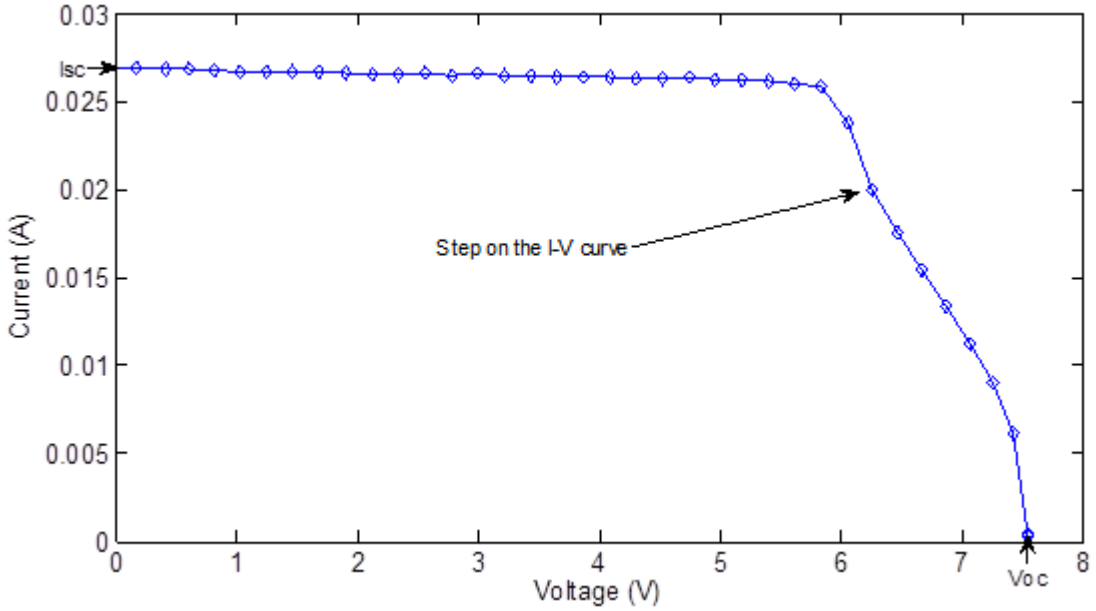

Figure 6.25: Multi-crystalline silicon module measured I-V curve at STC.

6.4.6 Comparison of manufacturer's and measured parameters

The manufacturer's specification and the measured performance parameters of the module under STC are shown in Table 6.3. Cracks in the cells and fingers and also a crack in the bus bar, seem to have contributed to the drastic reduction of the module output current. As a consequence, the P_{max} of the module is reduced significantly. The LA-LBIC and EL results seem to link the enormous deviation of the measured performance parameters from the manufacturer's parameters, as revealed by the I-V characterisation results, to the current mismatch introduced by cracks in the module.

Table 6.3: Manufacturer's and measured performance parameters of mc-Si PV module.

Performance parameters	P_{max}(W)	V_{max}(V)	I_{max}(A)	V_{oc}(V)	I_{sc}(A)
Manufacturer	1.0	6.0	0.17	7.2	0.3400
Measured	0.2	5.8	0.03	7.5	0.0269

6.4.7 Comparison between mc-Si module LA-LBIC map and EL image

The LA-LBIC map and the EL image of mc-Si module are shown in Figure 6.26.

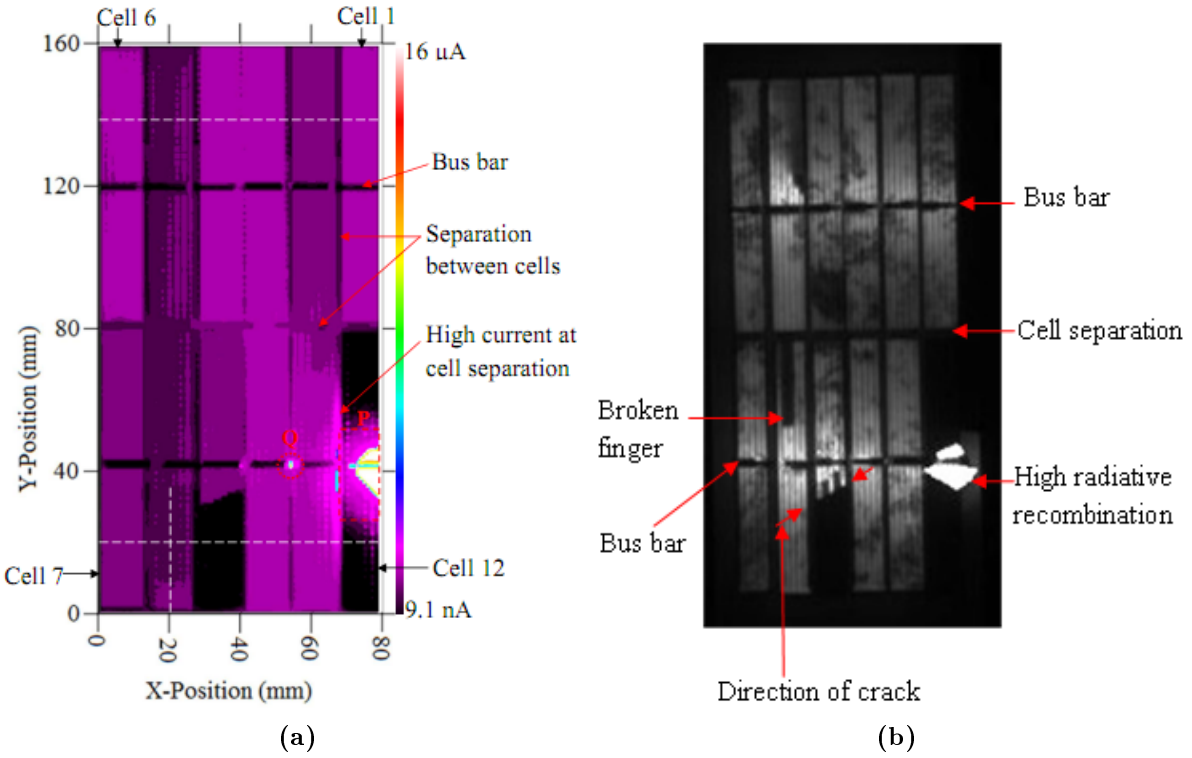

Figure 6.26: Multi-crystalline silicon PV module showing (a) LA-LBIC map (b) EL image.

The cracks in cells 9 and 12 in the LA-LBIC image also appear in the EL image as seen in Figure 6.26. In the EL image, the intensity of the light emitted as a result of radiative recombination is directly proportional to the local voltage [10] and therefore weak and inactive areas of the cells appear dark while good areas appear bright [115]. Bus bars and cell separations are both visible in the LA-LBIC map and EL image as inactive areas. While some points on the bus bar and between cells in the LA-LBIC map show high current, these features are not detectable by the EL technique. This is because the high current results from multiple reflections of the incident light by module features during LA-LBIC scanning and has nothing to do with the quality of the cell material, making the features undetectable by EL technique. It is worth noting that the broken finger in the EL image on cell 8 is not visible in the LA-LBIC map at a resolution of 1 mm spot diameter. During EL imaging, current is used to forward bias a module in order to excite charge carriers which eventually recombine radiatively, causing luminescence. Therefore, a broken finger implies charge carriers within the region are not excited and hence no photoemission is induced, making it easily detectable on the EL image. However, in LA-LBIC, the photo-current generated at the broken finger by the point illumination is in the vicinity of two adjacent unbroken fingers, which are used to conduct the photo-current at the broken finger and this makes the broken finger undetectable by the LA-LBIC technique.

6.5 Amorphous silicon (a-Si) photovoltaic module

This module consists of 29 cells connected in series by monolithic integration. The entire module was scanned with white light with a spot diameter of 5 mm to establish areas of interest which were later investigated using a 1 mm laser spot diameter. The spot-illuminated PV module equivalent circuit model was used to interpret the variation in photo-current between and within the module cells. Due to the shifts in individual cell voltages during scanning, the measured point-illuminated module I_{sc} is less than the actual point-illuminated module I_{sc}. Therefore, in order to quantify and compare the point illuminated module I_{sc} at different points on the module, point I-V measurements were performed. By mapping the module under illumination at different wavelengths, the photo-current at different depths of the cell material was investigated.

A photograph of the module and the LA-LBIC map scanned at short circuit using white light of spot diameter 5 mm are shown in Figure 6.27.

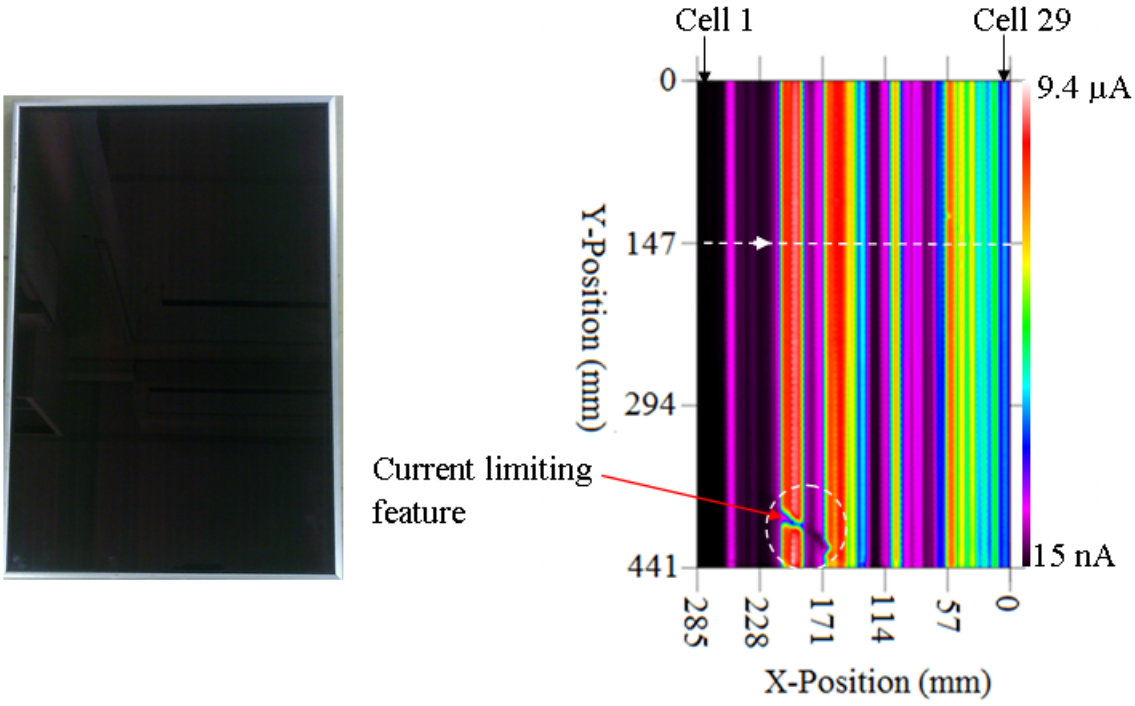

Figure 6.27: Amorphous silicon PV module showing (a) Photograph (b) Short circuit LA-LBIC map under white light illumination.

Due to the large spot size used, the module cells in the LA-LBIC map in Figure 6.27 are not distinctly seen. In order to examine the cells properly, a line scan was performed across

the cells at position y = 147 mm in Figure 6.27, using 633 nm laser illumination with a spot diameter of 1 mm. The short circuit line scan is presented in Figure 6.28. The LA-LBIC map and the line scan show how the photo-generated current varies between and within the module cells.

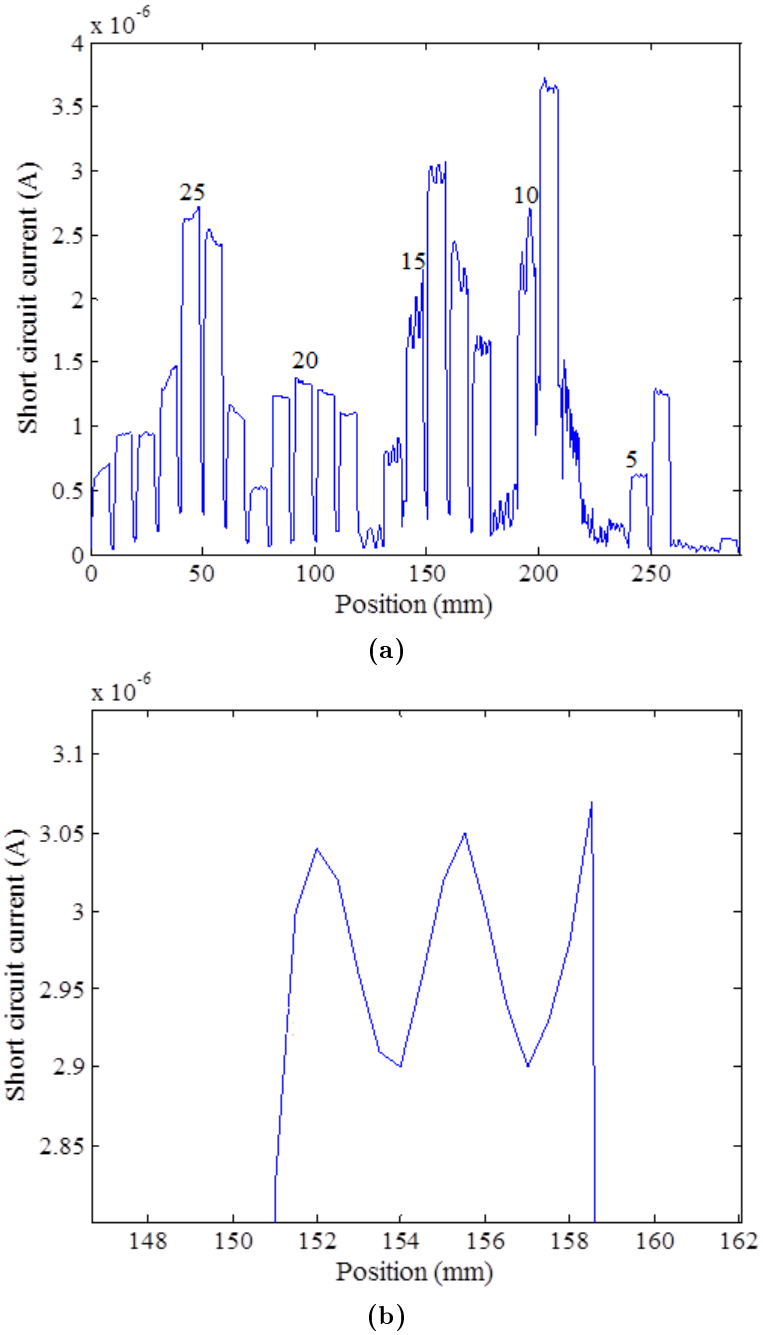

Figure 6.28: (a) Line scan, with cell numbers shown, performed at position y = 147 mm in Figure 6.27 using laser illumination. (b) Magnified region with circular dotted lines on cell 14 in (a), illustrating variation in photo-current within a cell.

6.5.1 Variations in photo-generated current

6.5.1.1 Between cells

The I_{sc} varies considerably from cell to cell as seen from the LA-LBIC map in Figure 6.27 and the line scan under laser illumination in Figure 6.28. In order to compare the variation in photo-current between cells, a line scan was extracted from the LA-LBIC map in Figure 6.27 at position y = 147 mm and is presented in Figure 6.29. This line scan, from the LA-LBIC map scanned by white light is similar to the line scan under laser illumination, shown in Figure 6.28.

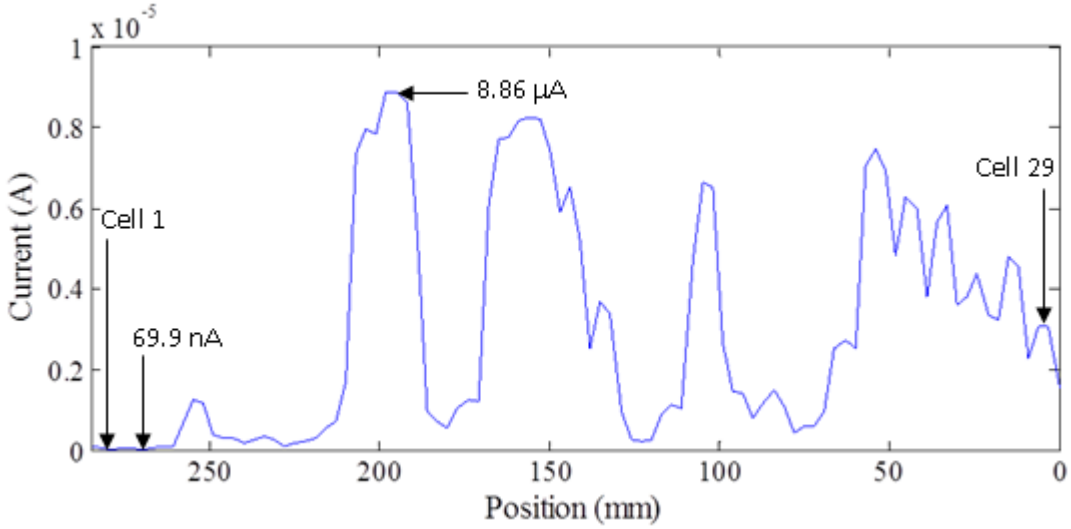

Figure 6.29: Line scan extracted at position y = 147 mm from the LA-LBIC map in Figure 6.27, showing variation in photo-current between module cells.

The variation in photo-current between the cell with the lowest photo-current and that with the highest photo-current is 8.79 μA, as can be seen in Figure 6.29. During thin film module manufacture, the PV materials are deposited over a large area and the cells are monolithically isolated and interconnected using laser scribing. The huge variation in photo-current from cell to cell, as seen in the extracted line scan, suggests that this variation is not due to non-uniformity in the deposited cell material. Variation in photo-generated current arising from non-uniformity in thin film deposition cannot affect all the cells as seen in the line scan, since the deposition is expected to be uniform in some areas and in such areas the generated photo-current would be uniform. Variation in photo-current due to deposition non-uniformity in an area of a module would affect all the cells within that area, as seen in the enclosed region in the LA-LBIC map (Figure 6.27). Cell to cell photo-current variation can therefore be more reasonably hypothesised to result from the formation of the

cell interconnection. Non-uniform effects of the laser beam on the walls, depth and width of the scribes and also incomplete cleaning of the debris left in the scribes make the cells electrically different from each other. Laser scribing is known to create material defects along the edge of the scribe lines [80] and shunting usually results from the P1 and P3 laser scribes [128] during the cell isolation and interconnection process as explained in chapter 3, Figure 3.3. Residue left in the scribes [81] and lack of optimisation of laser parameters [129] also lead to shunting. The variation in photo-generated current between cells is thus attributed to the differences in the shunt resistances of the individual module cells.

The spot-illuminated equivalent circuit model in Figure 2.6 is used to explain the variation in photo-generated current between cells in the module. When the light spot is on a cell, the current generated has to flow through the shunt resistances of all the non-illuminated cells before it is measured. In order for equal current to flow in the string, the non-illuminated cells become reverse biased and consequently force the illuminated cell into forward bias. The amount by which the photo-generated current at the illuminated spot drops is therefore determined by the effective shunt resistance of the non-illuminated cells. The change in the measured current from cell to cell therefore means the effective shunt resistance of the non-illuminated cells changes when the spot is moved from one cell to another. However, cells experiencing the same effect from the non-illuminated cells show similarity in photo-response, meaning that their shunt resistances are comparable.

6.5.1.2 Within cells

In order to investigate the variation in photo-current within cells, a line scan was extracted along cell 8 at position x = 216 mm from the LA-LBIC map in Figure 6.27. The extracted line scan is shown in Figure 6.30 and indicates a variation in photo-current of 0.28 μA between the lowest and the highest performing points within the cell.

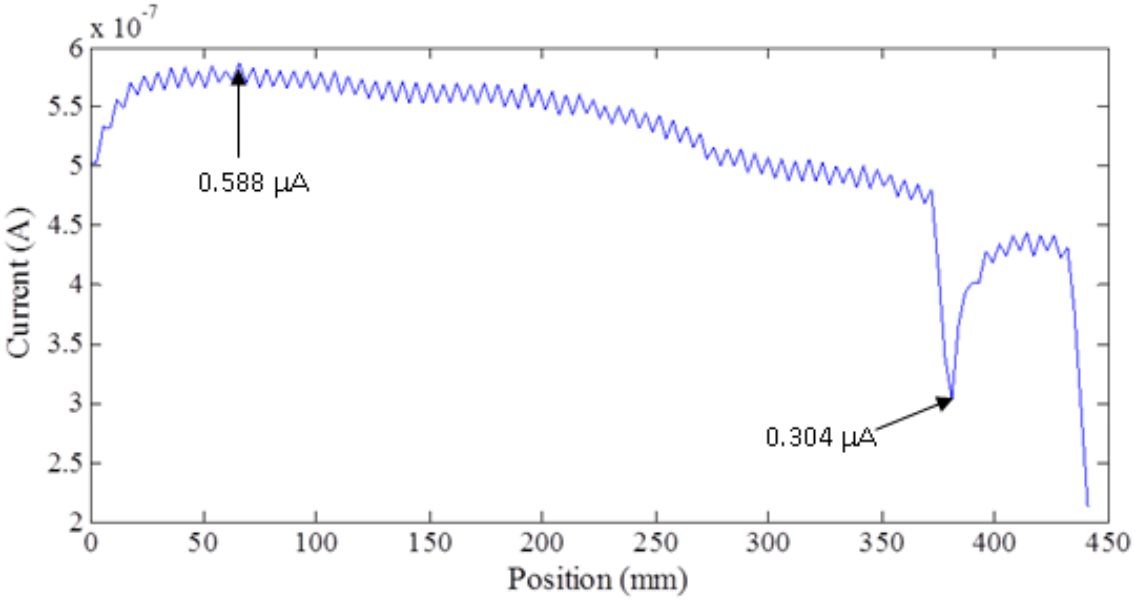

Figure 6.30: Line scan extracted at position x = 216 mm from the LA-LBIC in Figure 6.27, showing variation in photo-current within a module cell.

The variation in current within a cell can also be explained using the spot-illuminated equivalent circuit model in Figure 2.6. When the light spot is confined within a cell, the reduction in photo-generated current due to the reverse bias effect of the non-illuminated cells remains constant. The only variation in current within a cell therefore arises from the non-identical electrical properties within the cell. In the case of thin film modules, variation in current within a cell can arise from non-uniformity in the deposited cell material. Film thickness is a parameter that affects the solar cell performance [76, 78, 79, 130], and because of the large area deposition of the PV material, thin film modules are prone to variations in the thickness of the deposited film.

The variation in photo-current between cells of 8.79 μA (Figure 6.29) and that within a cell of 0.28 μA (Figure 6.30) indicates that the variation in photo-current between cells is higher than within cells. The extremely high variation in photo-current between cells arises from the cell formation process during module construction.

The line scan under laser illumination in Figure 6.28 shows that some cells have significant variations in photo-current within cells, although this is not comparable to that between cells. The variations are distinctly seen, especially in cells 8, 10 and 15. This could be attributed to shunts introduced during the scribing process.

6.5.1.3 Current limiting feature

The enclosed area indicated by a dashed line circle in the LA-LBIC map in Figure 6.27 shows a current limiting feature traversing cells 9, 10, 11, 12 and 13. In order to properly visualise the effect of the current limiting feature on photo-generated current, this area was scanned under laser illumination and the photo-response map is presented in Figure 6.31.

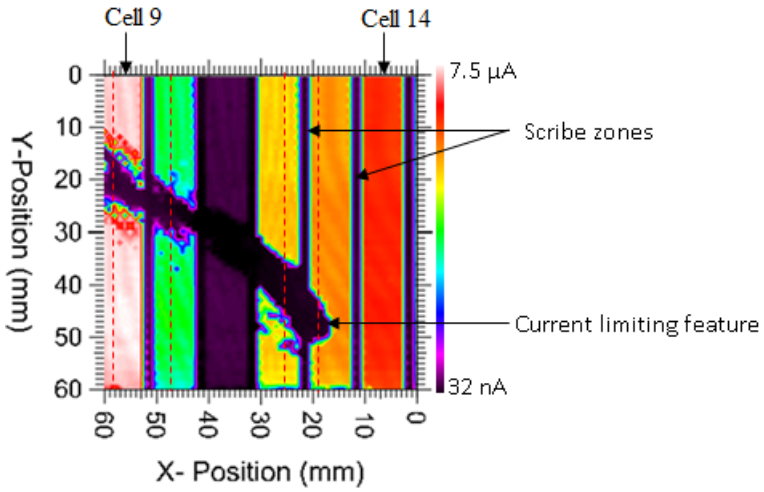

Figure 6.31: Photo-response map of the encircled region in Figure 6.27 under laser illumination

Line scans were extracted at position x = 19, 25, 47 and 58 mm, as indicated by the dotted red lines in Figure 6.31, to investigate the effect of the current limiting feature on cells 13, 12, 10 and 9 respectively. The line scans are presented in Figure 6.32 and show that the current limiting feature reduces the current in the affected cells by almost the same amounts, as highlighted by the circular dotted lines. This feature could be due to the presence of foreign material on the substrate, which affected the deposition uniformity of the PV material at the location.

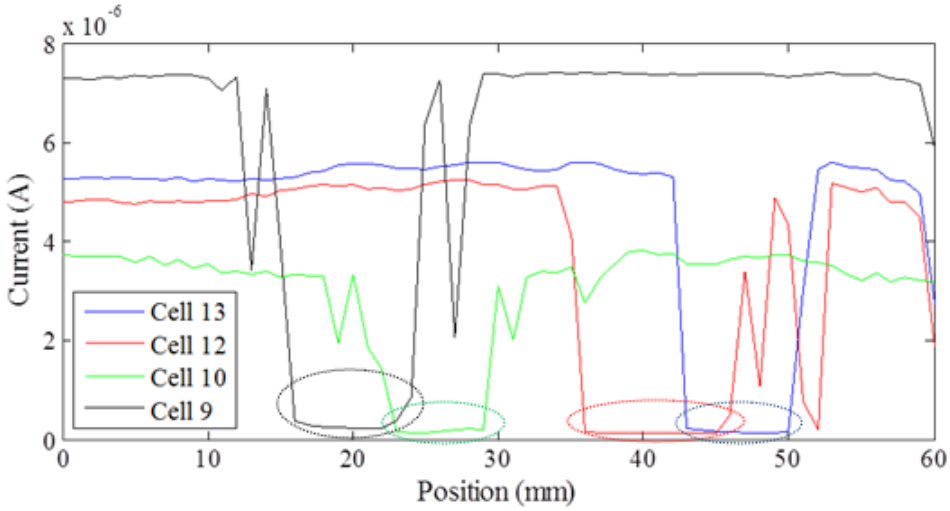

Figure 6.32: Line scans extracted from Figure 6.31 at position x = 19, 25, 47 and 58 mm, showing how the current limiting feature affects the photo-current of the different module cells.

6.5.2 Module point I-V measurements

Figure 6.33 is the LA-LBIC map of the enclosed region in Figure 6.27(b). Point I-V curves were measured at different points along the dotted lines shown in Figure 6.33 in order to compare the point illuminated module I_{sc} between and within cells in the enclosed region in Figure 6.27

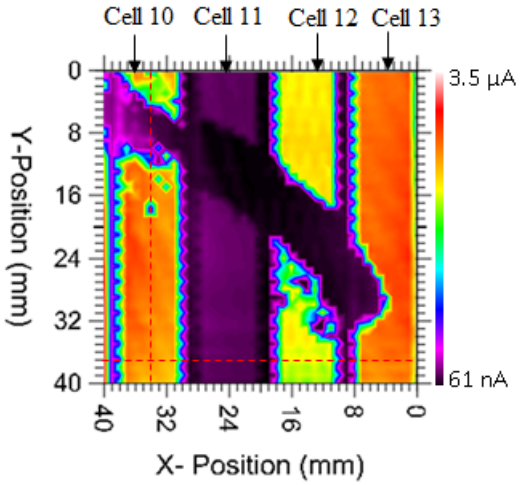

Figure 6.33: Short circuit photo-response map of an area of an a-Si module showing positions at which point I-Vs were measured, as marked by dotted lines.

The variation in point-illuminated module I_{sc} between and within cells are shown in the

point-illuminated module point I-V curves presented in Figure 6.34. The point-illuminated I-V curves measured for the four different cells along the dotted lines, at the specified points, indicate a significant variation in point-illuminated module I_{sc}. Cell 11 generates the lowest point-illuminated module I_{sc} and V_{oc}. Large variations in photo-generated current between module cells is not unusual since cells acquire different levels of shunting during the module manufacturing process. The point-illuminated module I-V curves measured along the dotted lines, at the specified points within cell 10, show little variation in point-illuminated module I_{sc} and V_{oc}, except for the I-V curve measured at the current limiting feature which shows almost no current and voltage. Large variations in electrical performance parameters within cells are usually not expected, unless the cell has a current limiting feature.

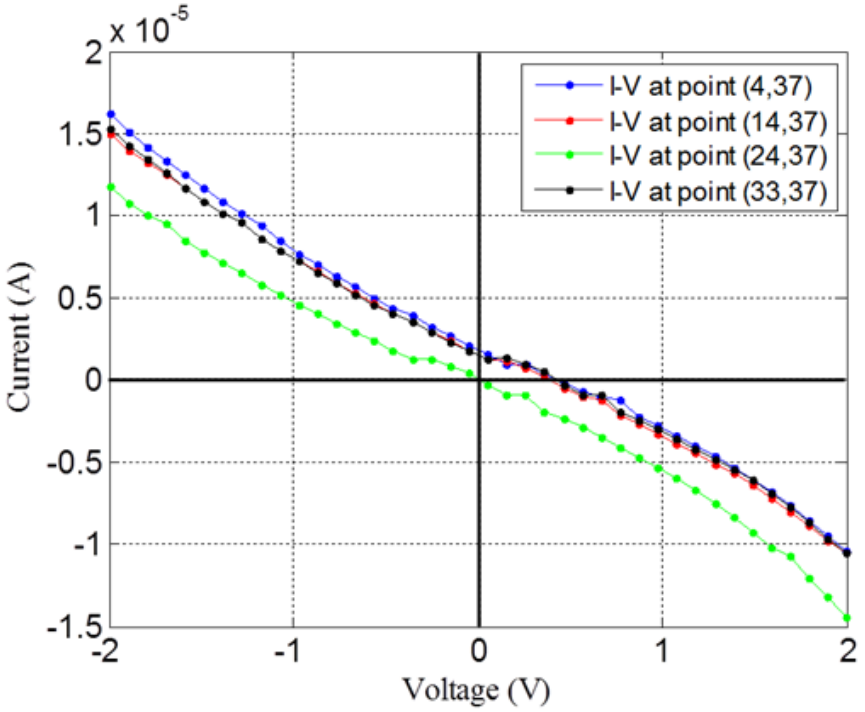

(a)

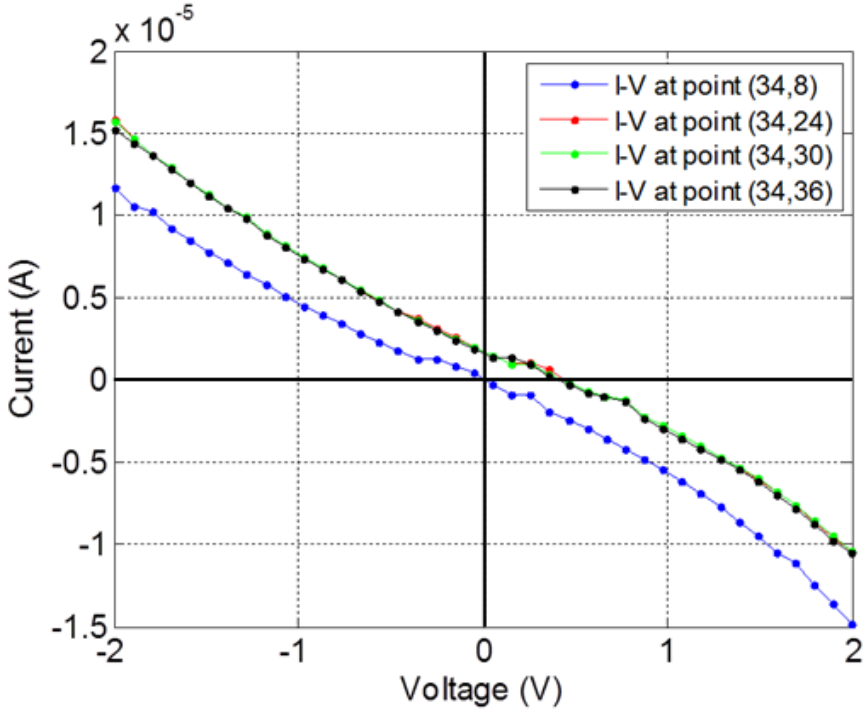

(b)

Figure 6.34: Comparison of short circuit current (a) Between cells (b) Within cells.

6.5.3 Photo-generated current at different illumination wavelengths

The area with the current limiting feature in Figure 6.27 was scanned using different light wavelengths and the results are presented in Figure 6.35. Different light wavelengths have different penetration depths and the point-illuminated module I_{sc} generated by different wavelengths was investigated. In order to analyse the effect of photon energy on I_{sc}, line scans were extracted from each of the maps at position y = 80 mm (dotted lines in Figure 6.35) and the results are shown in Figure 6.36. The 448 nm wavelength photons generate a lower I_{sc} than the 660 nm wavelength photons, because the charge carriers are generated near the solar cell surface and are affected by surface recombination. The 785 nm wavelength photons are mostly absorbed in the bulk but generate very little current. It should be noted that the band gap energy of a-Si is equivalent to a wavelength of about 790 nm [131], which is close to the 785 nm wavelength. When the energy of the photons is close to the band gap energy, the photons are weakly absorbed since only the electrons at the edge of the valence band can interact with the photons [132].

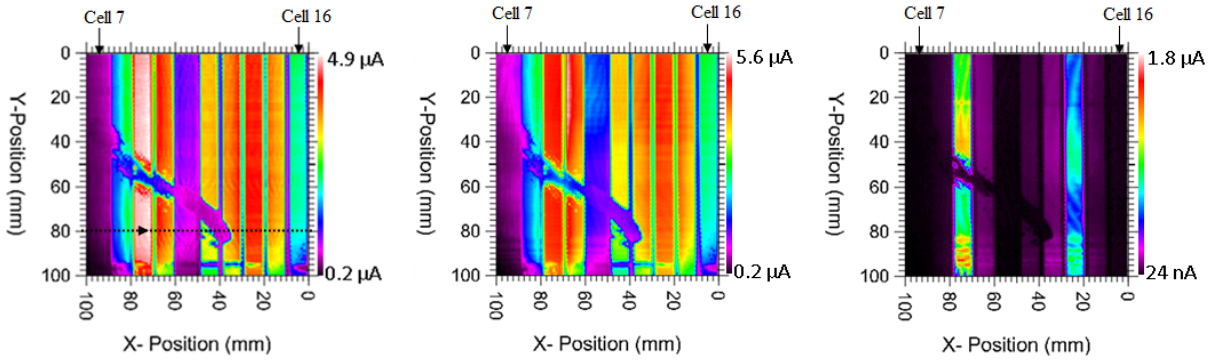

(a) 448 nm wavelength **(b)** 660 nm wavelength **(c)** 785 nm wavelength

Figure 6.35: Short circuit current map of the area containing the current limiting feature, scanned using different light wavelengths at 2 mW power.

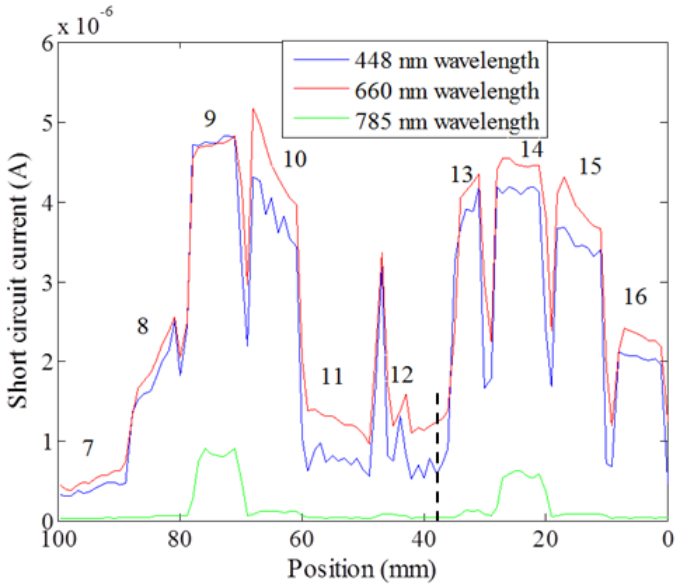

Figure 6.36: Line scans extracted from Figure 6.35 at position y = 80 mm. The vertical dotted line shows part of cell 13, affected by the current limiting feature.

Part of cell 13, affected by the current limiting feature, is indicated by the vertical dotted line in Figure 6.36. It can be seen that, the variations in I_{sc} for the different wavelengths, for this affected part, is similar to the variations that occur in the cells without the current limiting feature. Therefore, it can be inferred that, the current limiting feature is an active PV material. The reduced I_{sc} at the feature, therefore, could be due variation in thickness of the deposited PV material.

6.5.4 Investigating the shunting levels of module cells by using different light intensities

Line scans were performed at position y = 80 mm in Figure 6.35, using 448 nm wavelength laser light at different intensities and the results are shown in Figure 6.37. The light intensity was changed by changing the laser power. Decreasing the light intensity means less photons are available for absorption, hence I_{sc} decreases. However it should be noted that the rate of decrease is not uniform for all the cells. At low light intensities, highly shunted cells show the highest percentage drop compared to the cells with low shunt levels. Shunts are detrimental at low light intensities [133] and cells with high shunt resistance retain a greater fraction of their original power at low light intensity than those with low shunt resistance [134]. The solar cell equivalent resistance starts to approach the shunt resistance when the light intensity decreases and the fraction of the total current through the shunt resistance increases when

these two resistances are similar [135]. By scanning light of different intensities across the module cells and computing the percentage drop in current at high and low intensity for each cell, the shunting levels of the module cells can be compared.

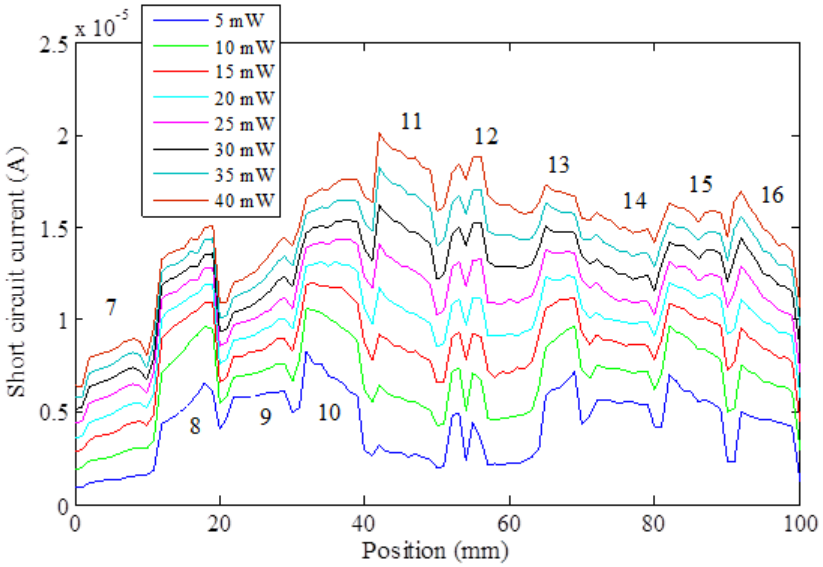

Figure 6.37: Line scans at position y = 80 mm along the dotted line in Figure 6.35(a), using light of wavelength 448 nm at different laser powers.

The dependence of I_{sc} on laser power was investigated for cell 8, by plotting the I_{sc} at position 15 mm in Figure 6.37 against the different laser power, as shown in Figure 6.38. It can be seen that the I_{sc} is almost linearly dependent on the laser power. Increasing the laser power means more photons are available for absorption, hence I_{sc} increases.

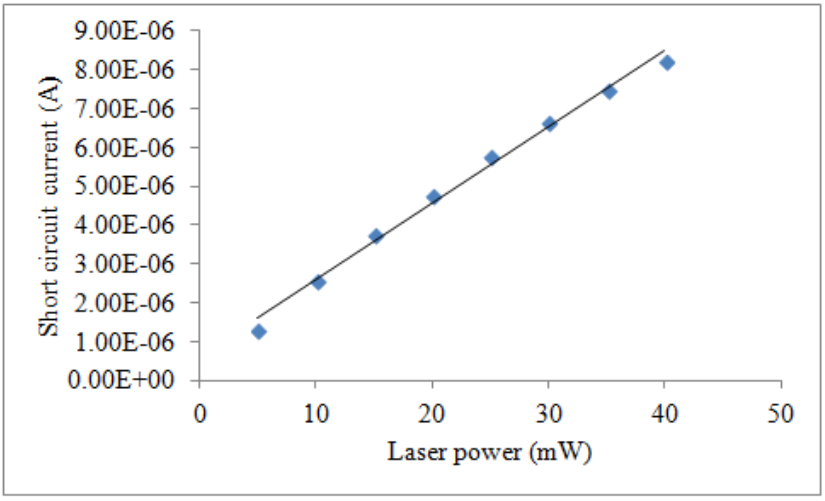

Figure 6.38: The dependence of a-Si point-illuminated module I_{sc} on laser power, extracted for cell 8 at position 15 mm in Figure 6.37.

The I_{sc} values were extracted at the centre of each cell in Figure 6.37 for 5 mW and 40 mW laser power and the results are presented in Table 6.4. It can be seen that cells which show the highest percentage drop in I_{sc} are more shunted than those showing a lower percentage drop. These results are consistent with the short circuit LBIC results in Figure 6.35.

Table 6.4: Drop in I_{sc} for different cells under illumination with 5 mW and 40 mW power.

Cell	7	8	9	10	11	12	13	14	15	16
I_{sc} at 40 mW (µA)	8.3	13.9	12.6	17.0	19.1	18.8	17.3	14.9	15.8	14.9
I_{sc} at 5 mW (µA)	1.3	5.2	5.8	7.0	2.8	4.4	5.9	5.4	6.2	4.6
% drop in I_{sc}	84.3	62.6	54.0	58.8	85.3	76.6	65.9	64.0	60.8	69.1

6.6 Copper indium diselenide (CIS) modules

Two CIS modules, A and B, consisting of 50 and 34 monolithically series-connected cells respectively, were investigated. The manufacturer's specifications for the modules are shown in Table 6.5.

Table 6.5: Manufacturer's STC performance parameters for the CIS module.

Performance parameters	P_{max} (W)	V_{max}(V)	I_{mp}(A)	V_{oc}(V)	I_{sc}(A)
Values at STC (Module A)	10	18.8	0.53	25.0	0.61
Values at STC (Module B)	5.5	16.5	0.33	22.0	0.36

Both modules were scanned by white light of spot size 5 mm to identify features of interest which were later investigated using laser light of spot size 1 mm. In module A, short circuit current mapping and module point I-V measurements were performed to identify and study the effects of the current limiting features on the module short circuit current. In module B, the effect of forward voltage bias on the photo-generated current of the module cells was investigated.

6.6.1 Short circuit current mapping of performance limiting features

A photograph of module A and the LA-LBIC map under white light illumination is presented in Figure 6.39. The two salient features in the LA-LBIC map include the current limiting feature at the right edge of the module and an electrical disconnection feature at the centre of the module indicated by the arrows. It can be noticed that due to the effect of the electrical disconnection feature, significant variation in photo-current occurs within the cells.

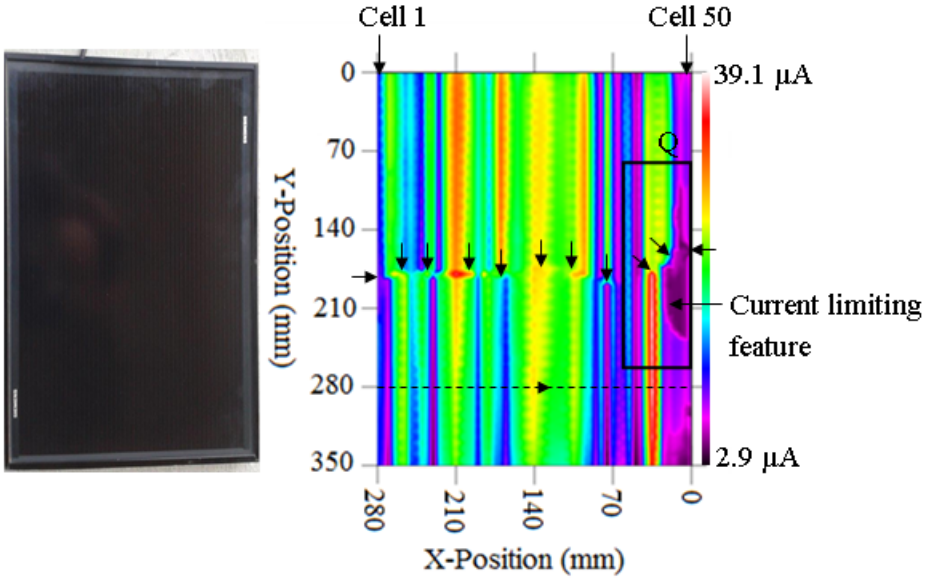

Figure 6.39: CIS module A showing (a) Photograph (b) LA-LBIC map under white light illumination.

The scribe lines are not distinctly seen in the LA-LBIC map because of the large spot size used. In order to view the cells separately from each other, a line scan under laser illumination of spot diameter 1 mm was performed at position y = 280 mm as shown in Figure 6.39. The line scan is shown in Figure 6.40 and shows variation in photo-current both between and within cells.

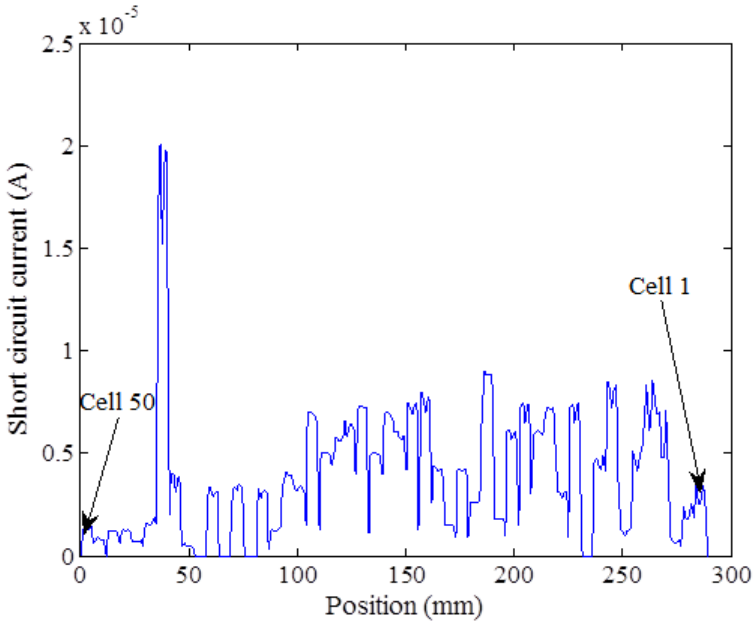

Figure 6.40: Line scan at position y = 280 mm in Figure 6.39, under laser illumination of spot diameter 1 mm.

Figure 6.40 shows large variations in I_{sc} between cells than within cells. The large variations could be attributed to variations in the shunt resistances of individual cells in the module.

By scanning the area labelled Q using laser light (633 nm, 1.5 mW), the electrical disconnection and the current limiting feature become more prominent as seen in Figure 6.41. It is also worth noting that a third feature, indicated by a circle on Figure 6.41 is a region of extremely low photo-response, which is not seen in Figure 6.39. This feature is an electrical disconnection in the form of a triangular shape and it is not visible in the white light scan because of the large spot size which overlaps on the surrounding areas during measurements at the points where the feature is located.

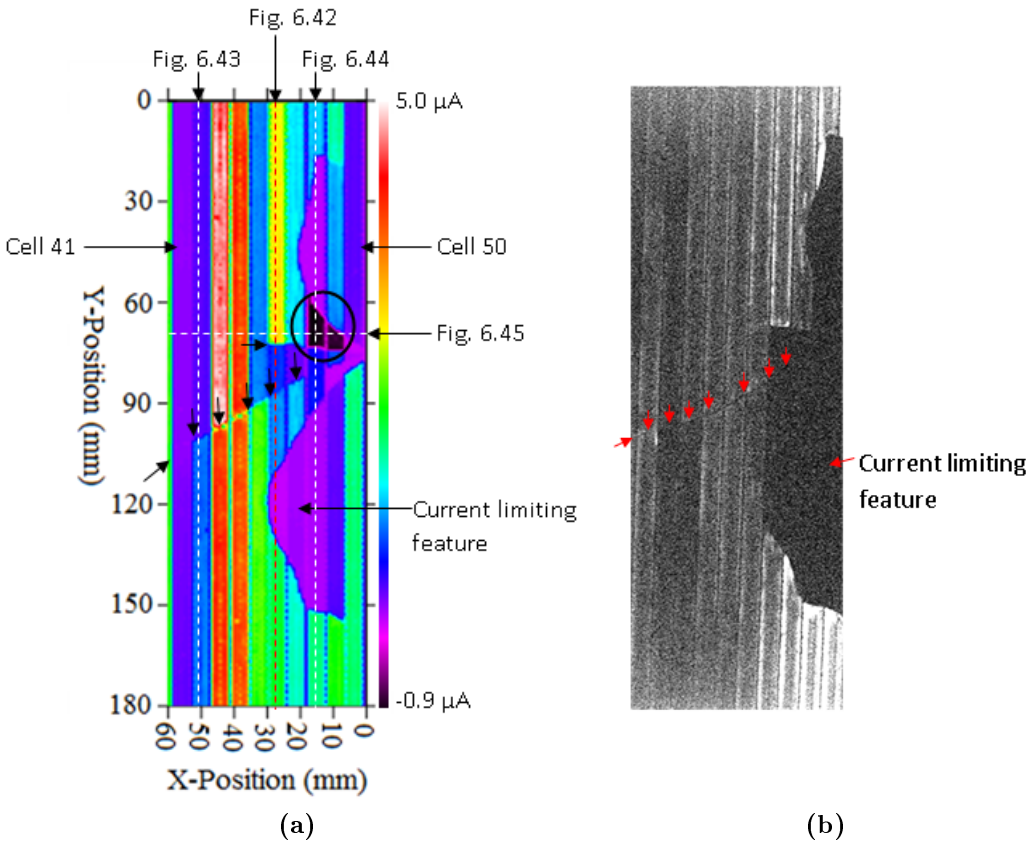

Figure 6.41: (a) Photo-response map under laser illumination and (b) EL image of area Q in Figure 6.39(b).

6.6.1.1 Current limiting feature

The current limiting feature is distinctly seen in the photo-response map as well as the EL image in Figure 6.41. By its characteristic well-defined boundary, the feature could be caused by an optical blockage [18] and may arise from delamination. The line scan extracted from Figure 6.41 at position x = 27 mm is presented in Figure 6.42 and shows LBIC of 22.3 nA generated at this feature, which is negligible compared to the current generated by the other parts of the cell. The variation in photo-current within cells can clearly be seen with LBIC, but not with EL.

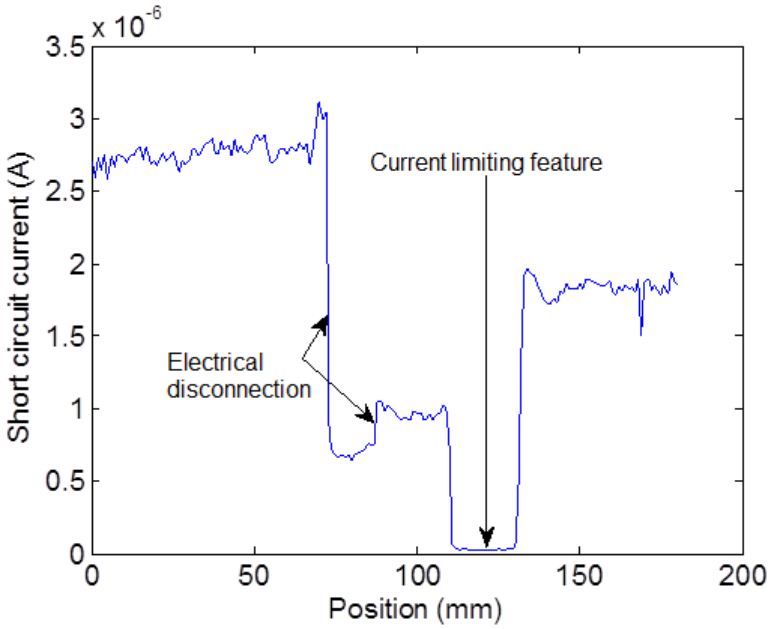

Figure 6.42: Line scan extracted from Figure 6.41 at position x = 27 mm, showing the effect of the current limiting feature and electrical disconnection on photo-current.

6.6.1.2 Electrical disconnection

The electrical disconnection in the LA-LBIC map in Figure 6.41, indicated by the line of arrows, causes the two affected areas of the module to operate in parallel. The electrical disconnection is verified by the electroluminescence (EL) image in Figure 6.41(b) and is indicated by red arrows. The EL image of the area in the LA-LBIC map excludes cell 50. A line scan extracted from the LA-LBIC map in Figure 6.41 at position x = 50 mm is shown in Figure 6.43, and indicates a drop in LBIC from 0.81 µA to 0.31 µA as a result of the disconnection. In the line scan, significant variation in current within the cell is observed. Variations in I_{sc} of 37% and 31% occurs at the 0.3 μA and 0.8 μA levels, respectively. Variation within a cell may arise from non-uniformity in the deposition layer thickness.

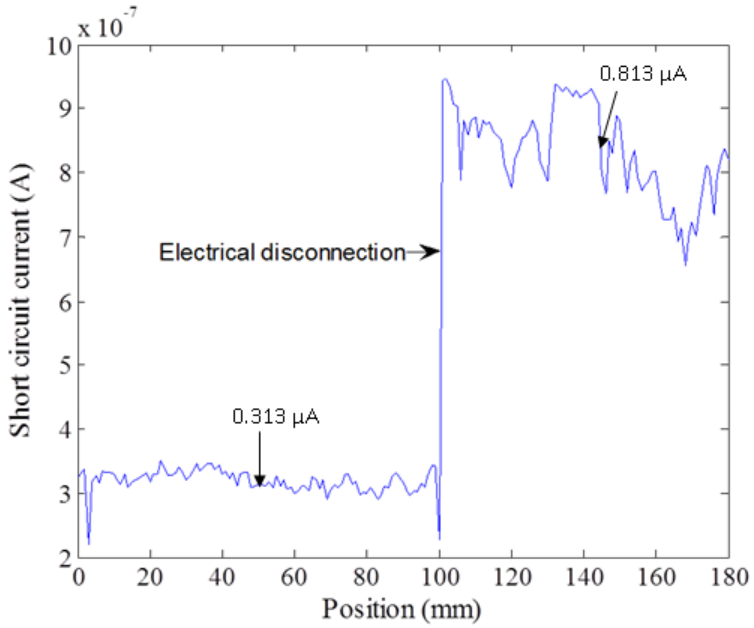

Figure 6.43: Line scan extracted from Figure 6.41(a) at position x = 50 mm showing how the electrical disconnection in the module causes a substantial variation in short circuit current within a module cell.

The triangular-shaped dark region indicated by the circle in Figure 6.41 shows a portion of cells 49 and cell 48 which has been electrically isolated from the rest of the cells. It appears that the disconnection has affected the top contact within the triangular region, while the back contact is unaffected. The interconnection of thin film cells into a module is shown in chapter 3, Figure 3.3. Illuminating the region within the triangular disconnection generates current which is unable to flow in the conventional direction of photo-current due to the discontinuity in the top contact. However, apart from the top contact of the isolated portion, the rest of the top contact remains unaffected. Noting that the disconnected portion does not create a discontinuity between the top and bottom contact of the entire module, and remembering that the two contacts are now at different potentials, current flows through the module, but in a reverse direction when the light spot is within the disconnected triangular portion. This is a very interesting feature detectable by the LA-LBIC technique and there is a need to apply other non-destructive characterisation techniques to evaluate their potential in the detection of such a feature. To highlight the reverse current generated at this disconnection feature, a line scan was extracted at position x = 15 mm from Figure 6.41 and this is presented in Figure 6.44.

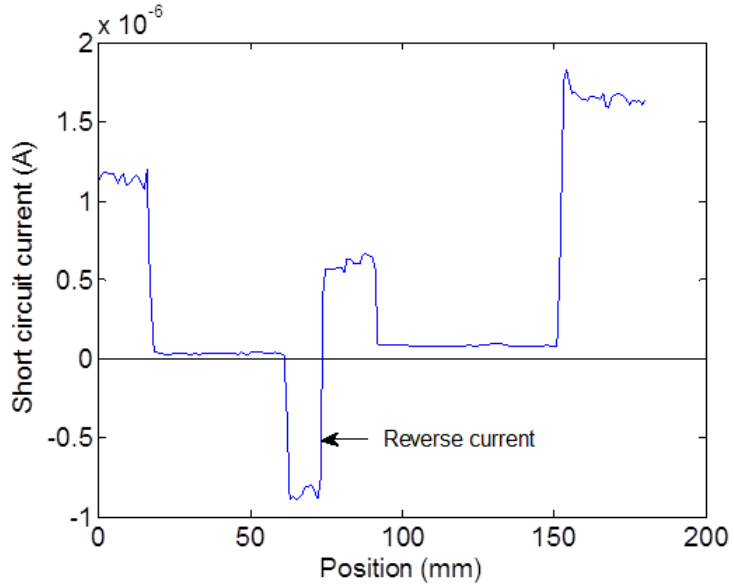

Figure 6.44: A line scan extracted from Figure 6.41(a) at position x = 15 mm, showing how current direction is reversed within the triangular-shaped disconnection feature.

Measurements of module point I-V curves along the horizontal dotted lines in Figure 6.41 at position x = 15 mm and x = 38 mm are shown in Figure 6.45. These were taken in order to compare the spot-illuminated module I_{sc} within the triangular shaped disconnection feature and at a good cell. At the good cell, the spot illuminated module I_{sc} is 3.5 μA while at the defect it is 0.9 μA in the opposite direction.

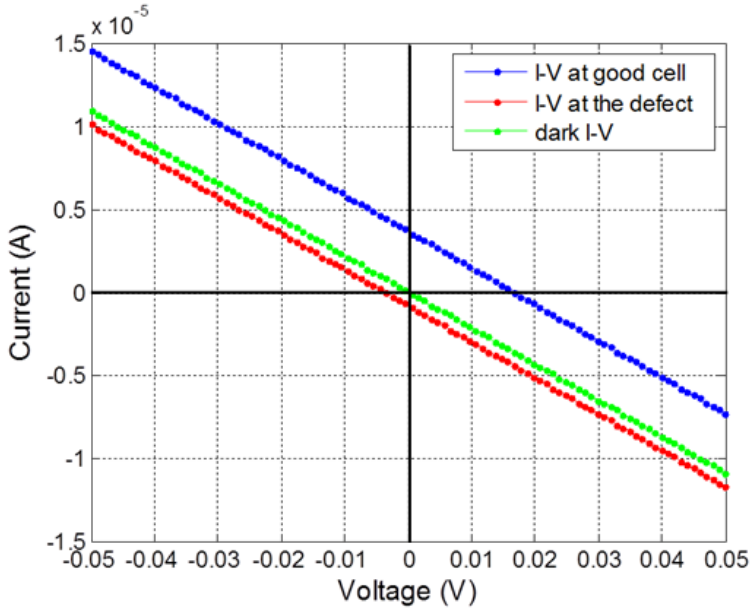

Figure 6.45: Module point I-V curves measured along the horizontal dotted line passing through the encircled region in Figure 6.41 at position x = 15 mm and x = 38 mm.

6.6.2 Module I-V characterisation

The measured I-V characteristic and the extracted parameters of module A are presented in Figure 6.46 and Table 6.6, respectively. Table 6.6 shows the manufacturer's and measured performance parameters at STC including the calculated R_s. As seen in the I-V curve, there is flattening of the curve making the knee almost invisible, consequently causing a significant drop in P_{max}. Reduction in slope at V_{oc} is a manifestation of an increase in module series resistance, which leads to a reduction in the maximum power point voltage [40]. It is worth noting that R_s has increased from 3.6 Ω to 48.6 Ω. This dramatic increase in R_s is due to the electrical disconnection in the module as revealed by LA-LBIC mapping. Electrical disconnections, such as a crack in a module can lead to a significant increase in the module R_s [64]. The increase in series resistance has a reducing effect on FF [136, 137]. The LA-LBIC technique can therefore be used to diagnose and trace the origin of local performance limiting features which alter the shape of the I-V curve and reduce the module electrical parameters.

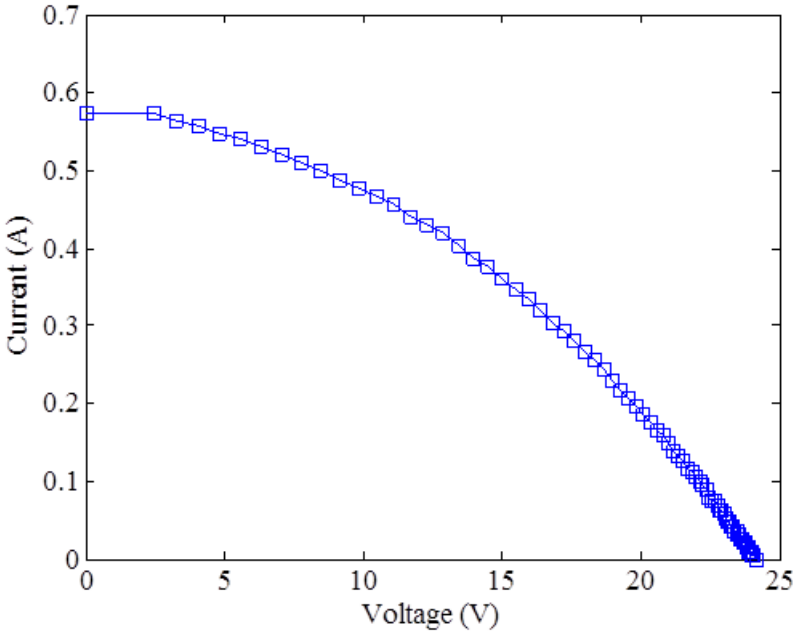

Figure 6.46: Measured I-V characteristics of CIS module A at STC.

Table 6.6: The manufacturer's and measured performance parameters of CIS module A at STC.

Parameters	P_{max}(W)	V_m(V)	I_m(A)	V_{oc}(V)	I_{sc}(A)	R_s(Ω)
Manufacturer	10	18.8	0.53	25.0	0.61	3.6
Measured	5.4	14.2	0.38	24.2	0.57	48.6

6.6.3 Comparison of manufacturer's and measured parameters

A significant reduction in the P_{max} of the module is noticed, as seen in Table 6.6. This is a consequence of the reduction in V_m and I_m, caused by the flattening of the I-V curve. The flattening of the I-V curve arises from the increase in R_s caused by the electrical disconnection in the module, as revealed in the LA-LBIC map and EL image.

6.6.4 Forward voltage biasing

The measured I-V curve and performance parameters of module B are shown in Figure 6.47 and Table 6.7, respectively.

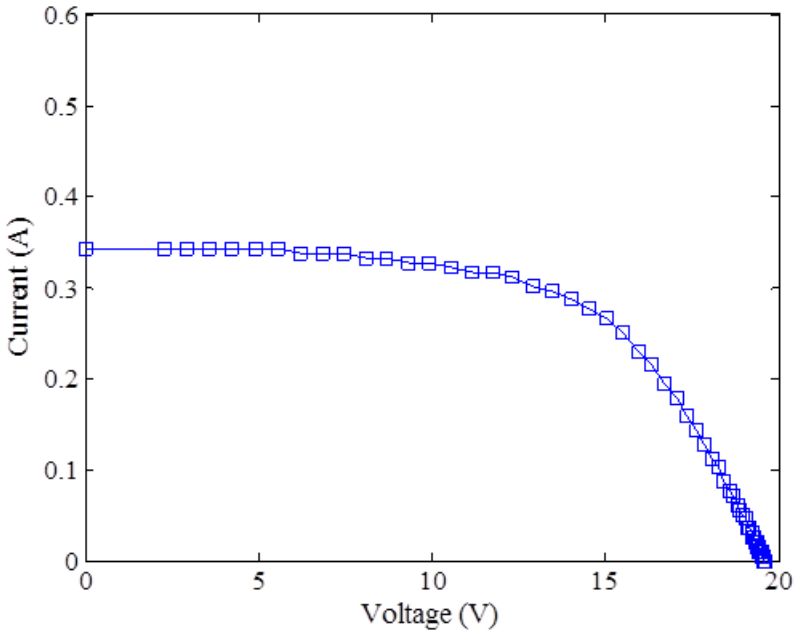

Figure 6.47: Measured I-V characteristics of CIS module B at STC

Table 6.7: The manufacturer's and measured performance parameters of CIS module B at STC.

Parameters	P_{max}(W)	V_m(V)	I_m(A)	V_{oc}(V)	I_{sc}(A)	R_s(Ω)
Manufacturer	5.5	16.5	0.33	22.0	0.35	7.5
Measured	4.0	14.2	0.28	19.6	0.34	34.6

Module B was scanned with white light of spot diameter 5 mm and the photograph and the LA-LBIC map of the module are shown in Figure 6.48.

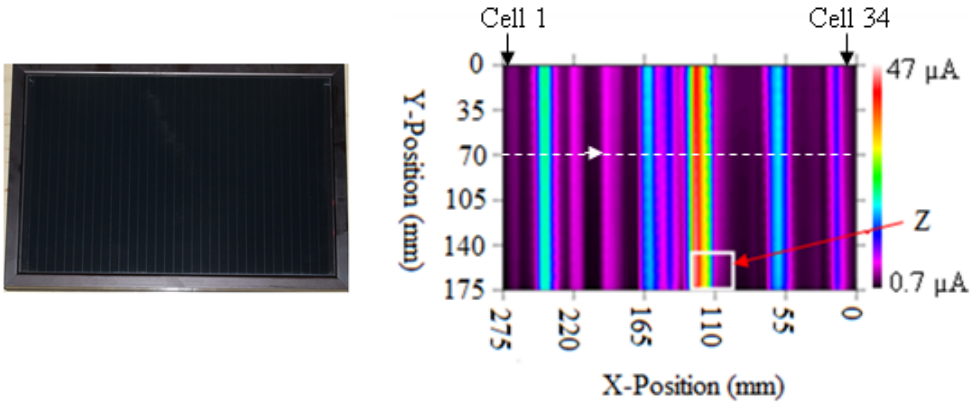

(a) **(b)**

Figure 6.48: CIS module B showing (a) Photograph (b) LA-LBIC map under white light illumination.

Due to the large spot size of the white light used, the scribe lines are not visible in the LA-LBIC map in Figure 6.48. However, the scribe lines were observed in the line scan in Figure 6.49, which was performed using a laser (spot size of 1 mm) across the cells at position y = 70 mm in Figure 6.48. The LA-LBIC map and the line scan show a large variation in photo-current between cells, while that within cells is very small. The large variation in photo-current between cells is attributed to the differences in the shunt resistances of the cells, as discussed previously.

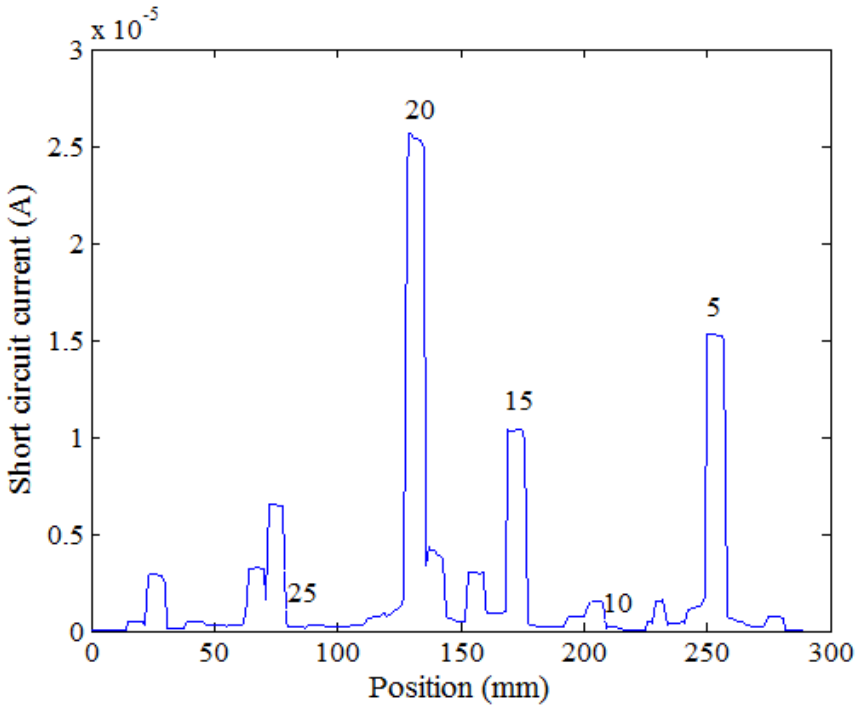

Figure 6.49: Line scan along the dotted line at position y = 70 mm in Figure 6.48 under laser illumination of 633 nm wavelength.

Area Z in Figure 6.48, which covers parts of cells 20, 21, 22 and 23, was scanned at different module forward voltage biases and the photo-responses maps are shown in Figure 6.50. Area Z was intentionally chosen because it consists of cells generating both high and low point-illuminated module photo-currents, making it possible to study the effect of forward voltage biasing on the point-illuminated module photo-current of both categories of module cells.

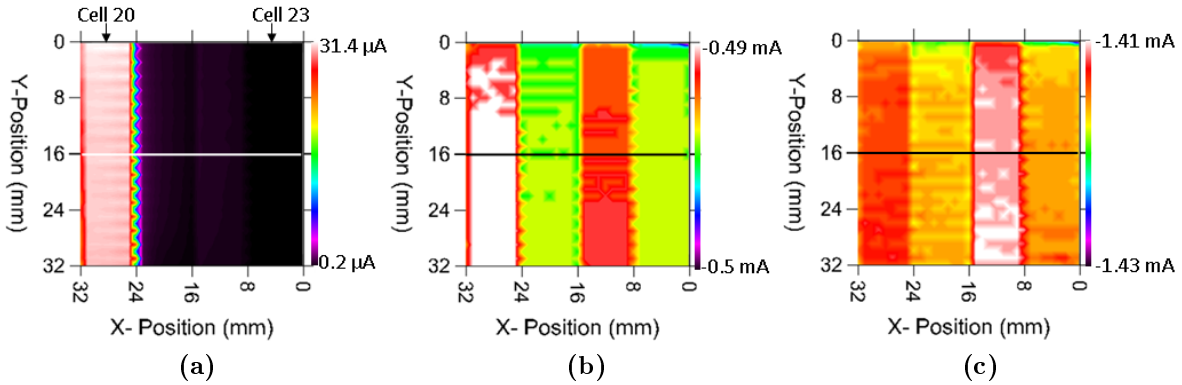

Figure 6.50: Photo-response map of area Z in Figure 6.48 scanned under laser illumination (633 nm, 1 mm spot size) at module forward biases of (a) 0 V (b) 3 V and (c) 5 V.

In order to visualise the changes in the point-illuminated module photo-current of the different module cells under different forward voltage bias conditions, line scans were extracted from Figure 6.50 at position y = 16 mm. The line scan at 0 V bias is presented in Figure 6.51 and shows that the point-illuminated module photo-current of cell 20 is much higher than that of the rest of the cells.

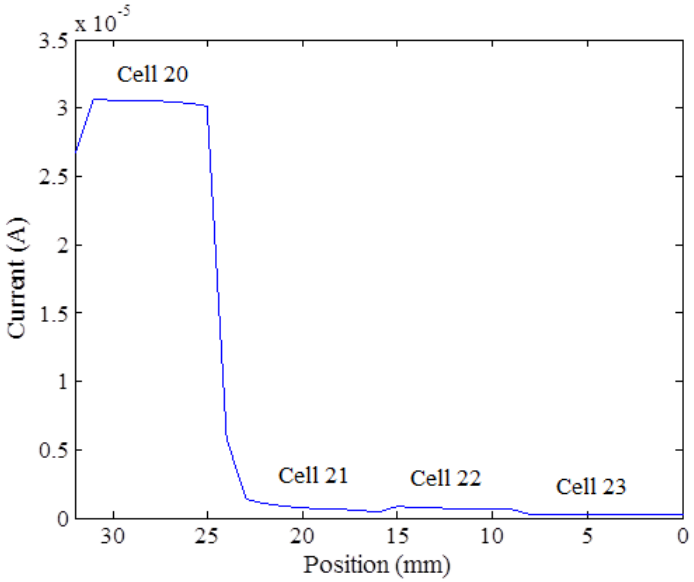

Figure 6.51: Line scan extracted from Figure 6.50 at position y = 16 mm, showing the photo-current generated by the cells at a module bias of 0 V.

When the forward bias voltage is increased to 3 V, as shown in the extracted line scan in Figure 6.52, the point-illuminated module photo-current of cell 20 reduces while that of cells 22 and 23, which were lower under 0 V bias, start to increase. The change in point-illuminated module photo-current of different module cells due to the increase in forward voltage bias gives a clue regarding the shunting level of the cells. An increase in the photo-current of severely shunted cells under forward voltage bias has been reported [49]. However, in this work, further analysis of the I-V curves of the shunted and less severely shunted cells under different module bias voltages is explored to establish why shunted cells generate a higher photo-current at a particular forward bias voltage than their less severely shunted counterparts.

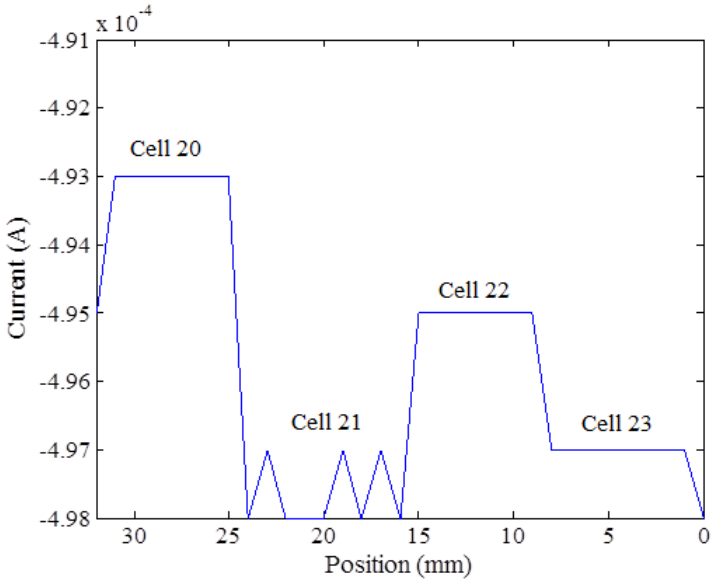

Figure 6.52: Line scan extracted from Figure 6.50 at position y = 16 mm, showing the photo-current generated by the cells at a module bias of 3 V.

When the forward bias voltage is increased to 5 V, as presented in the extracted line scan in Figure 6.53, the point-illuminated module photo-current of cell 20 continues to drop while that of cell 22 increases drastically, exceeding that of cell 20. This is an indication that, in the group of four cells considered, cell 22 is highly shunted.

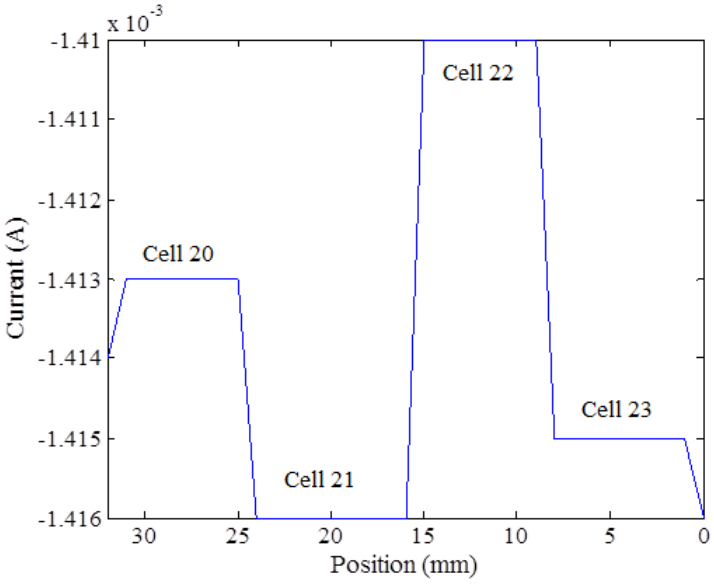

Figure 6.53: Line scan extracted from Figure 6.50 at position y = 16 mm, showing the photo-current generated by the cells at a module bias of 5 V.

The spontaneous increase in the photo-current of highly shunted cells is a result of the

crossing over of the I-V curves of the cells at some forward bias voltage. In order to explore this behaviour, spot-illuminated I-V curves of cell 20 and cell 22 were measured as shown in Figure 6.54.

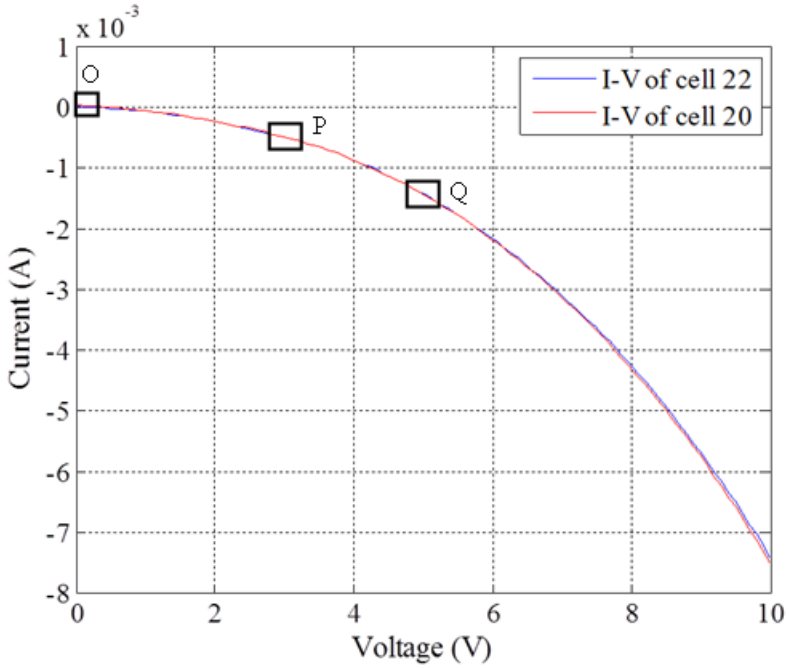

Figure 6.54: Point-illuminated module I-V curves measured on cell 20 and cell 22 shown in Figure 6.50 under laser illumination of 633 nm wavelength.

Magnification of area O in Figure 6.54 reveals that cell 20 generates a higher point-illuminated module I_{sc} than cell 22. This is shown in Figure 6.55 below.

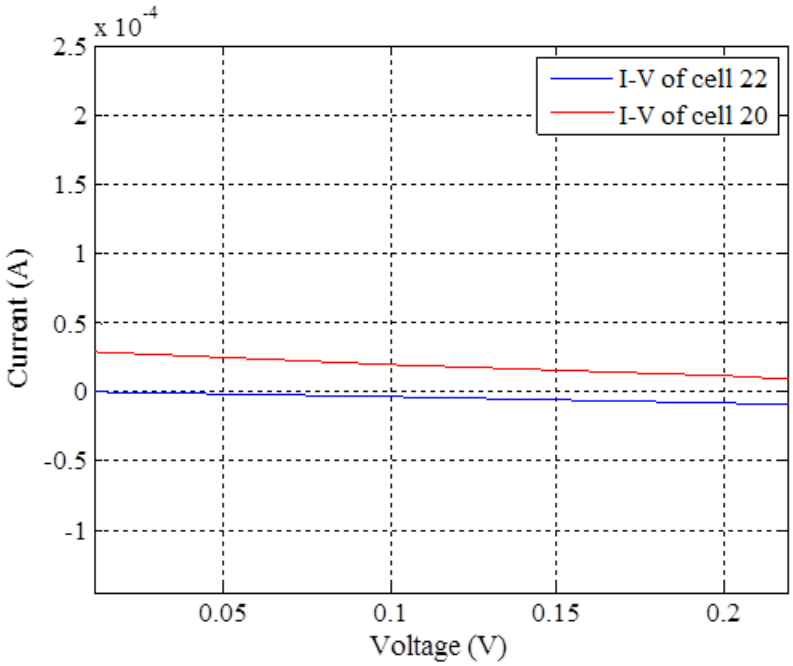

Figure 6.55: Magnification of area O in Figure 6.54 highlighting the point-illuminated module I_{sc} generated by cell 20 and cell 22.

Magnification of areas P and Q on Figure 6.54 are presented in Figure 6.56 and Figure 6.57, respectively. It is clear from these two areas that the I-V curves have crossed at some point between P and Q, since the I-V curve of cell 22, which was below that of cell 20 as shown in Figure 6.55, now lies above the I-V curve of cell 20. Beyond the crossover point, cell 22 begins to generate a higher photo-current than cell 20. It should be noted that areas P and Q are chosen to be at the module bias voltages of 3 V and 5 V respectively, used during scanning. The magnification of areas P and Q confirm that the I-V curves of the two cells crossed between the forward bias voltage of 3 V and 5 V.

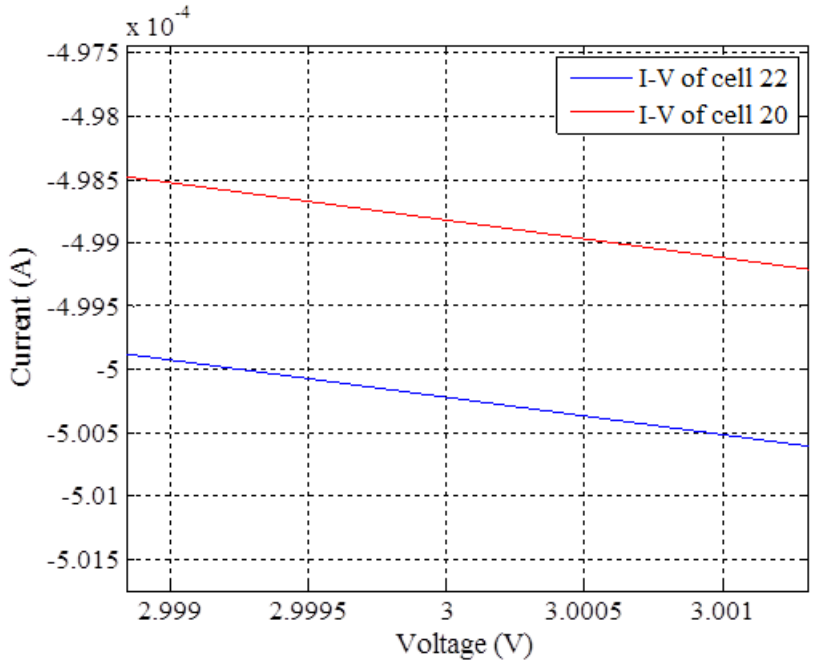

Figure 6.56: Magnified area P of Figure 6.54, showing that cell 20 generates a higher photo-current than cell 22 at a module bias voltage of 3 V.

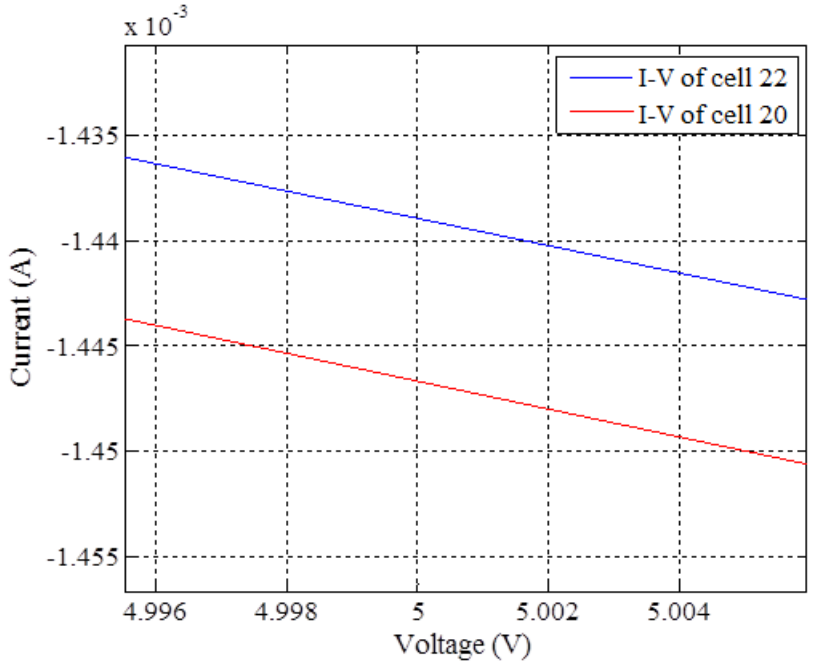

Figure 6.57: Magnified area Q of Figure 6.54, showing that cell 22 generates a higher photo-current than cell 20 at a module bias voltage of 5 V.

The concept of a highly shunted cell generating more photo-current than a less shunted cell as a result of the crossing over of the I-V curves of the two cells is illustrated in Figure 6.58.

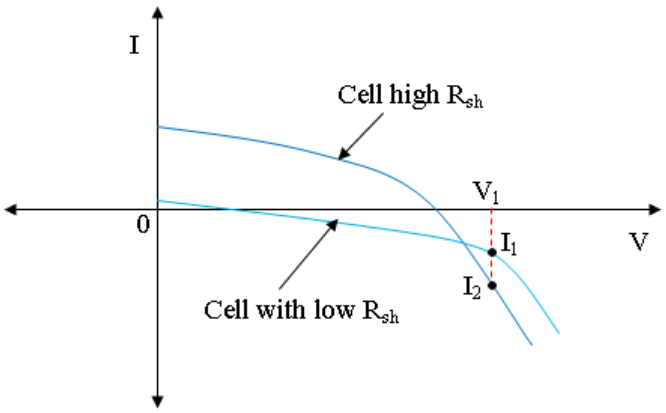

Figure 6.58: Illustration of how the I-V curves of cells with different levels of shunting cross over during increase in module forward bias, leading to severely shunted cells generating a higher current than less shunted cells.

At 0 V module bias, cells with higher R_{sh} generate more current than those with lower R_{sh}. When forward bias voltage is increased, the current generated by both groups of cells decrease but at a particular forward voltage bias, the I-V curves of cells with low R_{sh} cross over those of cells with high R_{sh}, such that at a particular forward bias voltage, V_1, the photo-current of cells with low R_{sh} exceeds that of the cells with high R_{sh}, as illustrated in Figure 6.58. Therefore, by scanning the module under different fixed forward biases and studying the changes in photo-response of the different cells, severely shunted cells can be identified. The LA-LBIC mapping of the module at different fixed voltage biases can therefore be used as a technique to investigate the shunting levels of the cells in a module.

6.7 A method for determination of the shunt resistance of cells in a PV module

A method to determine the shunt resistance of cells in an encapsulated PV module, which involves shading of an individual cell while the rest of the module is illuminated, is presented. In this section, a CIS module C consisting of 34 monolithically series-connected cells was used. The measured I-V curve of the module is shown in Figure 6.59 and the performance parameters are shown in Table 6.8.

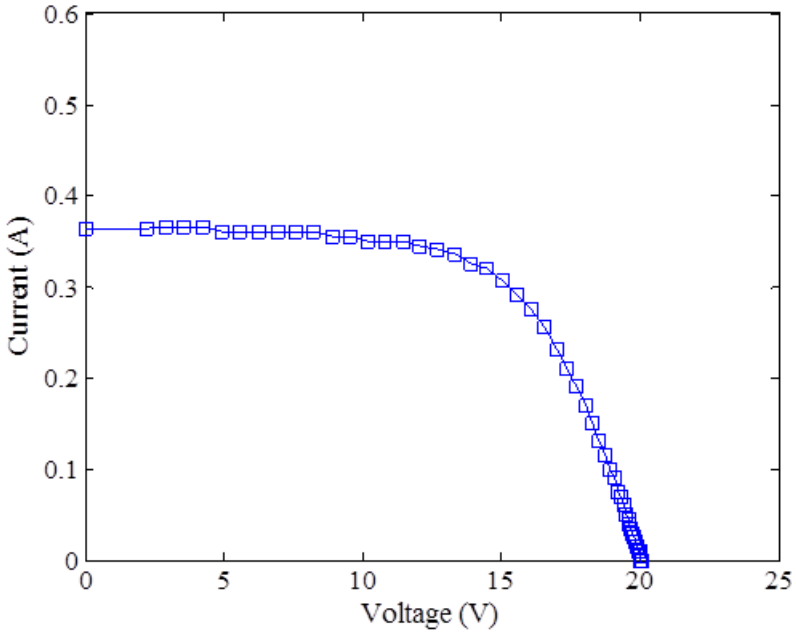

Figure 6.59: Measured I-V curve of CIS module C at STC.

Table 6.8: Manufacturer's and measured performance parameters of CIS module C at STC.

Performance parameters	P_{max}(W)	V_m(V)	I_m(A)	V_{oc}(V)	I_{sc}(A)	R_s(Ω)
Manufacturer	5.5	16.5	0.33	22.0	0.35	7.5
Measured	4.6	14.5	0.32	20.1	0.37	18.9

The photograph and LA-LBIC map under white light illumination are presented in Figure 6.60.

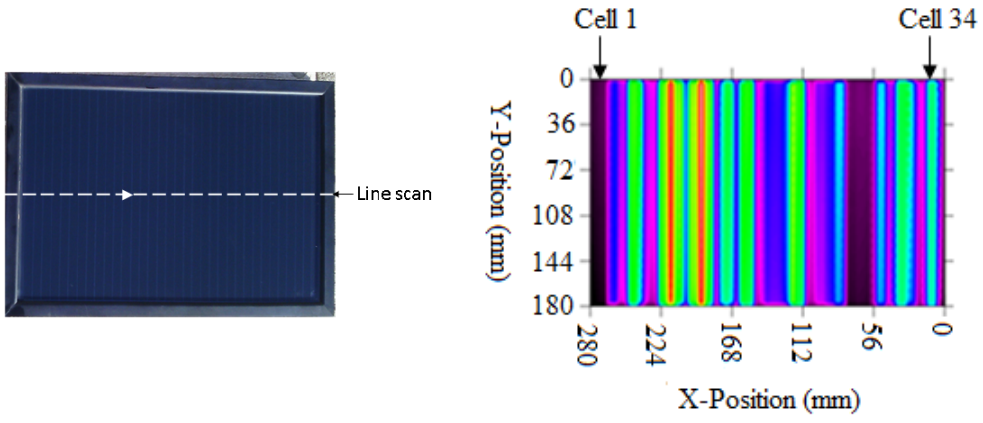

(a) **(b)**

Figure 6.60: CIS module C showing (a) Photograph (b) LA-LBIC map under white light illumination (power of 6 mW, spot size of 5 mm).

In order to distinctively view the cells, a line scan was performed along the dotted line in Figure 6.60(a) using laser illumination (power of 6 mW, spot size of 5 mm) and the result is shown in Figure 6.61.

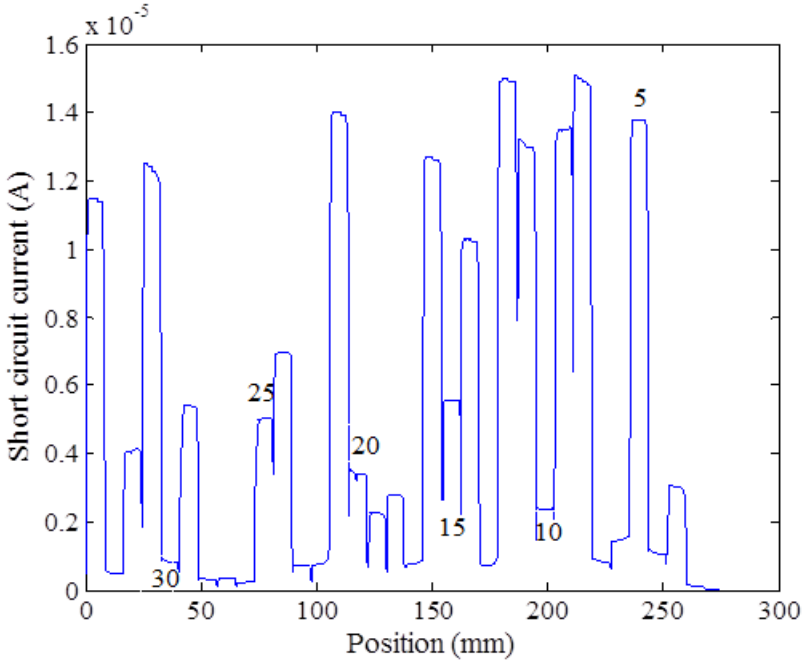

Figure 6.61: Line scan along the dotted line in Figure 6.60(a) under laser illumination. Cell numbers are indicated.

6.7.1 Shading scenarios and patterns

6.7.1.1 Fractional cell shading

Fractional cell shading was performed in order to investigate the response of the module I_{sc} as a function of the area of the cell shaded. Different fractions of the total area of a module cell were shaded using different sizes of an opaque rubber material as shown in Figure 6.62.

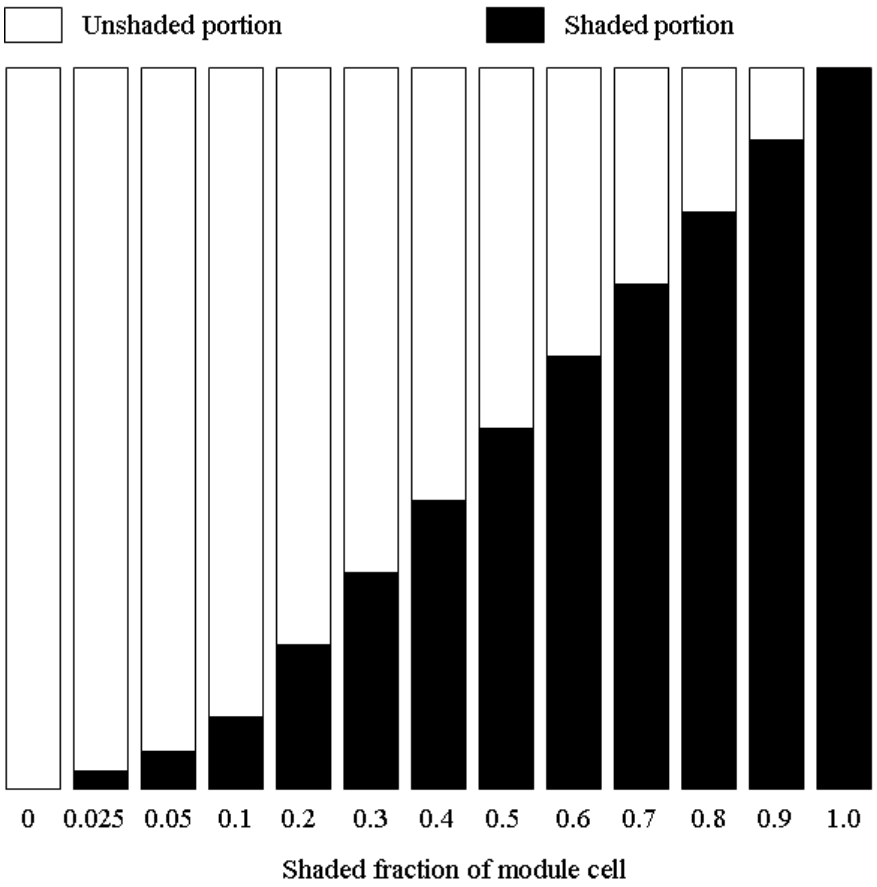

Figure 6.62: Schematic diagram showing how the different areas of a module cell under investigation were shaded using an opaque rubber material.

An LED light source was used to illuminate the module and was able to provide a relatively uniform intensity, with variation within $\pm 5\%$ over the module surface area, measuring 28 cm x 18 cm. The module was first fully illuminated and the module short circuit current, $I_{sc(F)}$, noted. Part of the cell under investigation was then shaded and the module short circuit current, $I_{sc(P)}$, recorded. It should be remembered that when a module cell is shaded, it becomes reverse biased and operates at a lower short circuit current than the string current [138]. The drop in module current, which is essentially the short circuit current generated by the cell's shaded portion, $I_{sc(SP)}$, was then computed using the equation:

$$I_{sc(SP)} = I_{sc(F)} - I_{sc(P)} \tag{6.1}$$

By plotting the short circuit current generated by each of the shaded portions against the fraction of the cell shaded, as shown in Figure 6.63, the relationship between the shaded area and the generated short circuit current could be explored. It is clear from the figure that,

as the shaded portion increases, $I_{sc\ (SP)}$ increase.

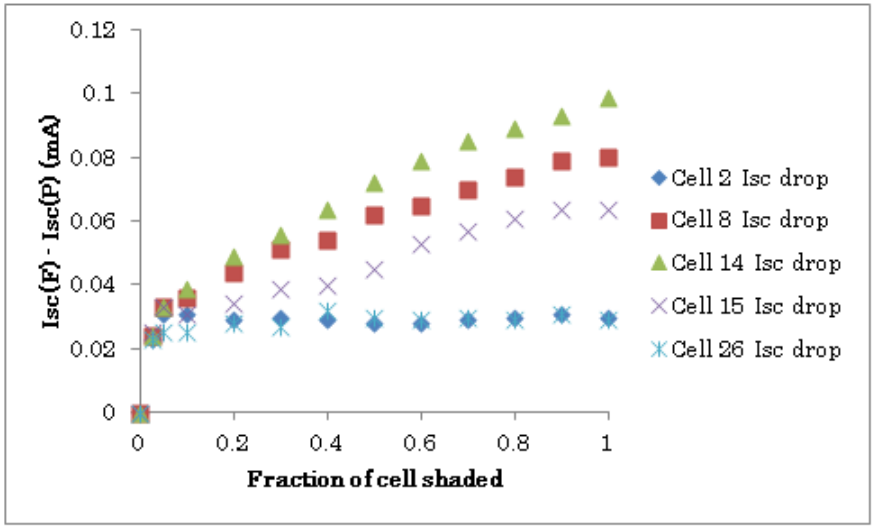

Figure 6.63: Drop in module current as a function of fractional area of the cell shaded.

In this experiment, it was assumed that the series resistance across each cell remains constant, the *pn* junction across a cell is of uniform quality and the illumination intensity variation within 5% does not cause a significant variation in module photo-generated current.

The equivalent circuit model in Figure 6.64 is used to explain how module current drop is related to the portion of the module cell shaded. For the sake of this explanation, different shading scenarios are applied on the middle cell of the module as shown in the equivalent circuit model.

When the module is fully illuminated as shown in Figure 6.64(a), all the shunt leakage paths are opened and the shunt current, I_{sh}, flows through the shunt resistances of the individual cells. Under this scenario, since no part of the cell is shaded, the drop in current due to shading is zero.

When a portion of the cell is shaded as shown in Figure 6.64(b), shunt losses through the shunt resistance of the illuminated part of the cell occurs, while the shunt resistance of the non-illuminated portion contributes to the module series resistance. The current flowing through this partially shaded cell therefore divides into two paths, however, hardly any current flows through the non-illuminated path due to its high resistance. Because of the low current through the shunt resistance of the non-illuminated path, the resultant voltage drop is small and hence the drop in the module output current is also small. When the shaded area of the cell is increased, the illuminated portion is reduced and the effective shunt resistance reduces since the shunt resistances within a cell are essentially in parallel.

Therefore, by increasing the shaded area, the current diverted through the non-illuminated portion increases, leading to a higher drop in the module output current.

When the entire cell is shaded as shown in Figure 6.64(c), all the current passes through the shunt resistance of the non-illuminated cell and this is when the voltage drop across the non-illuminated cell is at a maximum, causing the highest drop in module output current.

The R_{sh} values of the weak cells in Figure 6.63 are small and do not significantly affect the module series resistance compared to the good cells, and they therefore show a smaller drop in the module output current. Due to their low R_{sh}, varying the shading on the cell does not cause a significant change in the module output current. For the good cells, increasing the shading increases the current through the non-illuminated portion, leading to an increase in voltage drop across the overall series resistance, consequently reducing the module output current.

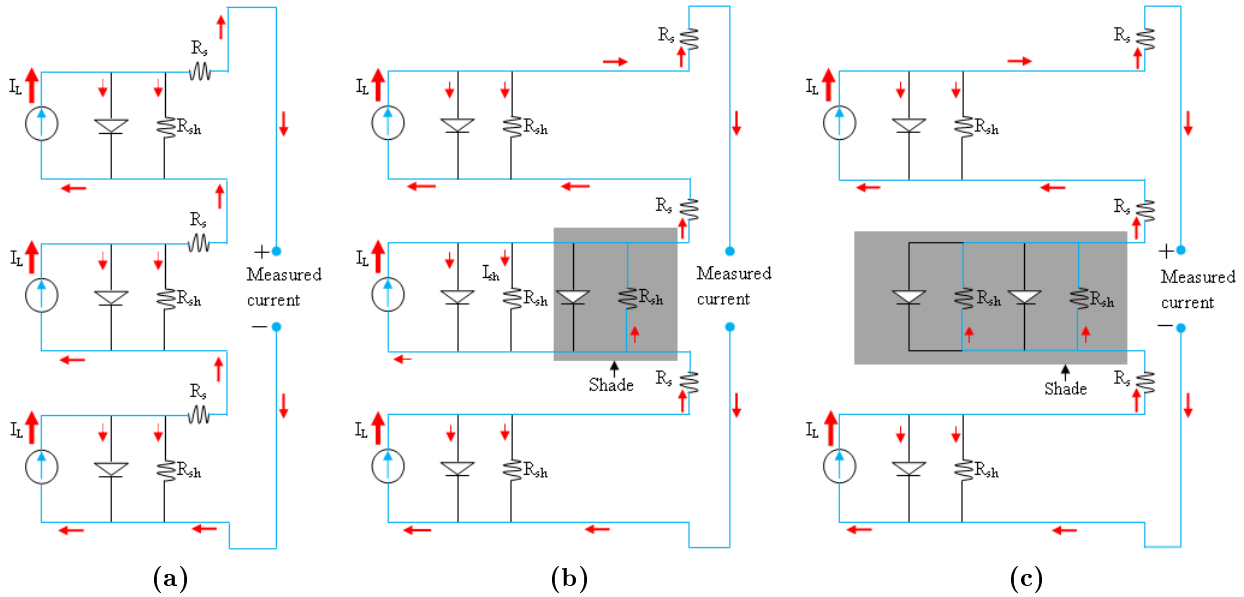

Figure 6.64: Photovoltaic module equivalent circuit model showing (a) Fully illuminated module (b) Part of a module cell shaded (c) Entire module cell shaded.

6.7.1.2 Full cell shading

In this experiment, it was assumed that $R_s \ll R_{sh}$ for each cell such that the voltage drop arising from cell shading is due to R_{sh} of the shaded cell. It was also assumed that the pn junction of the cells are of the same quality and that the illumination intensity variation (within 5%) does not cause a significant variation in module photo-generated current.

When a module is illuminated with one cell completely shaded, as shown in Figure 6.64(c), the shunt resistance of the shaded cell becomes an active circuit load resistance, causing a voltage drop which consequently reduces the measured module current. The drop in the measured module current is therefore related to the R_{sh} of the shaded cell and this can be used as a method for measuring the relative strengths of shunt resistances of cells in a PV module. By computing the decrease in the module output current when each cell is shaded, the shunt resistances of the cells in the module can be compared. In this investigation, equation 6.1 is applied to compute the decrease in module current. In this case, $I_{sc(F)}$ refers to the short circuit current of a fully illuminated module, while $I_{sc(P)}$ refers to the short circuit current of a module when one of its cells is completely shaded. Figure 6.65 shows that when shaded, the cells with low R_{sh} cause a lower decrease in module output current than the cells with high R_{sh}. As already explained, when R_{sh} is small, the resultant voltage drop is also small and this also leads to a small drop in the module output current. However, for a shaded cell with high R_{sh}, a high voltage decrease results, consequently causing a large decrease in the module output current.

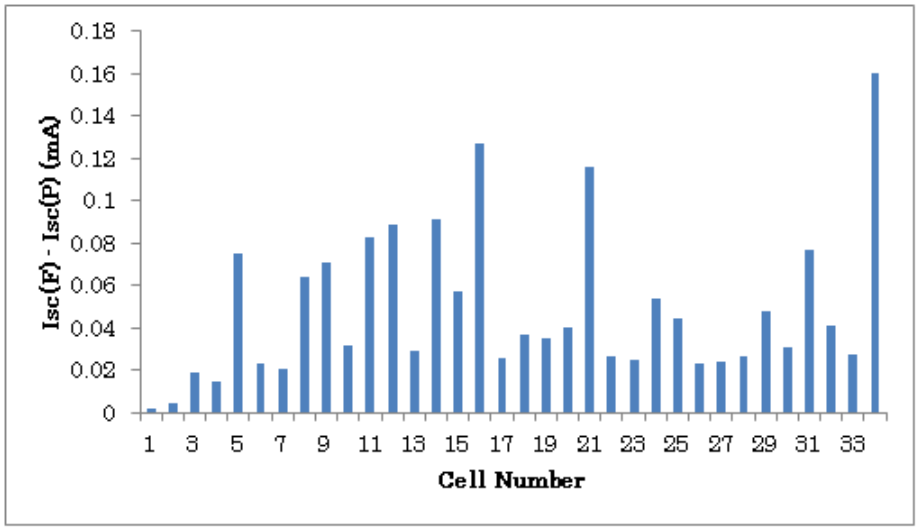

Figure 6.65: The current generation strength of each completely shaded module cell determined using equation 6.1.

6.7.2 Extraction of shunt resistance from I-V curves

In order to quantify the shunt resistances obtained from measurements of the I-V curves of a fully illuminated module and that with one cell shaded, the I-V curves were fitted using a LabView curve fitting program (shown in Appendix B) and the shunt resistances were extracted. The shunt resistance of each cell was obtained by subtracting the shunt

resistance extracted from the I-V curve with one cell shaded, from that extracted from the I-V curve of a fully illuminated module, according to the equation:

$$R_{sh(n)} = R_{sh(full-illum)} - R_{sh(n-shaded)} \tag{6.2}$$

where $R_{sh(n)}$ is the shunt resistance of cell n, $R_{sh(full\text{-}illum)}$ is the shunt resistance of the fully illuminated module and $R_{sh(n\text{-}shaded)}$ is the shunt resistance of the illuminated module with cell n shaded.

The I-V curves obtained by shading different module cells are presented in Figure 6.66. When a very weak cell, like cell 1, is shaded, the module I-V curve is almost identical to that of the fully illuminated module, implying that shading the cell produces insignificant impact on the module parameters. This is because cell 1 is highly shunted, and by its shunt resistance contributing to the module series resistance as a consequence of shading, the module series resistance hardly changes and the resultant voltage drop is so minute that the module output current remains almost the same. When a good cell, like cell 34 is shaded, the module I-V curve deviates significantly from that of a fully illuminated module, meaning that shading the cell has a considerable impact on the module parameters. A cell generating a high photo-current has a high shunt resistance when this cell is shaded, the module series resistance increases greatly, leading to a significant drop in the module output current. It should be noted that as the shunt resistance changes from cell to cell, the shape of the module I-V curves also changes as each cell is shaded.

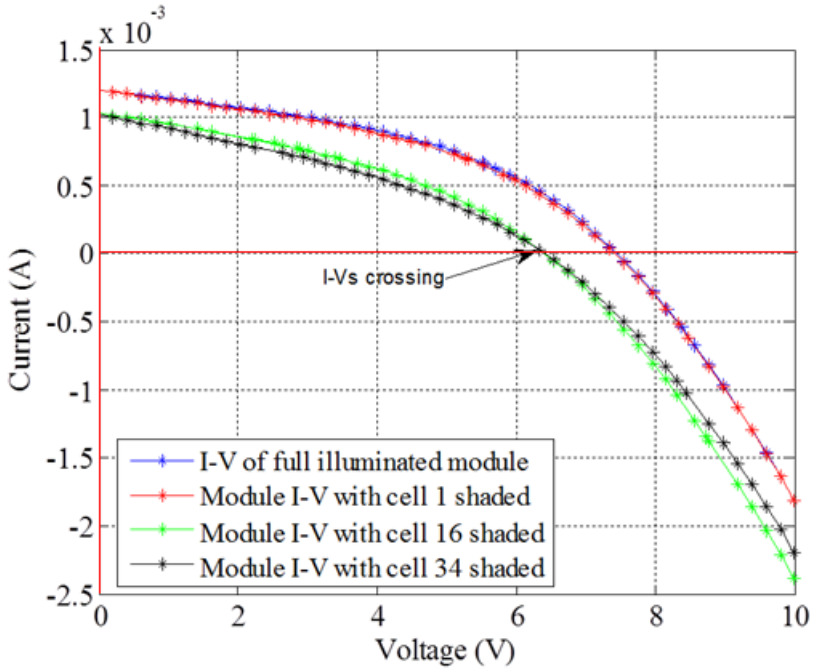

Figure 6.66: The I-V characteristics of the module under different shading conditions.

The slopes at V_{oc}, by observation, appear different when the different module cells are shaded. Cell 34, which is the best in the group, shows the highest reduction in the slope at V_{oc} while cell 1, which is the weakest, shows the lowest reduction in the slope. This observation is in agreement with the fact that shading a cell has the effect of increasing the module series resistance by the R_{sh} value of the shaded cell. The equivalent circuit model in Figure 6.67 is used to explain this observation, where $R_{sh1} \ll R_{sh3}$, while R_s for all the cells are assumed to be equal. When a weak cell (cell 1) is shaded as shown in Figure 6.67(a), the shunt resistance of the weak cell becomes an active series resistance. Due to the low value of the weak cell's shunt resistance, R_{sh1}, its contribution to the module R_s is smaller compared to that of a strong cell, like cell 34, and therefore the slope is less reduced by shading cell 1 compared to shading cell 34. When a strong cell is shaded, as shown in Figure 6.67(b), the high shunt resistance of the strong cell becomes an active series resistance, leading to a substantial increase in the module's series resistance.

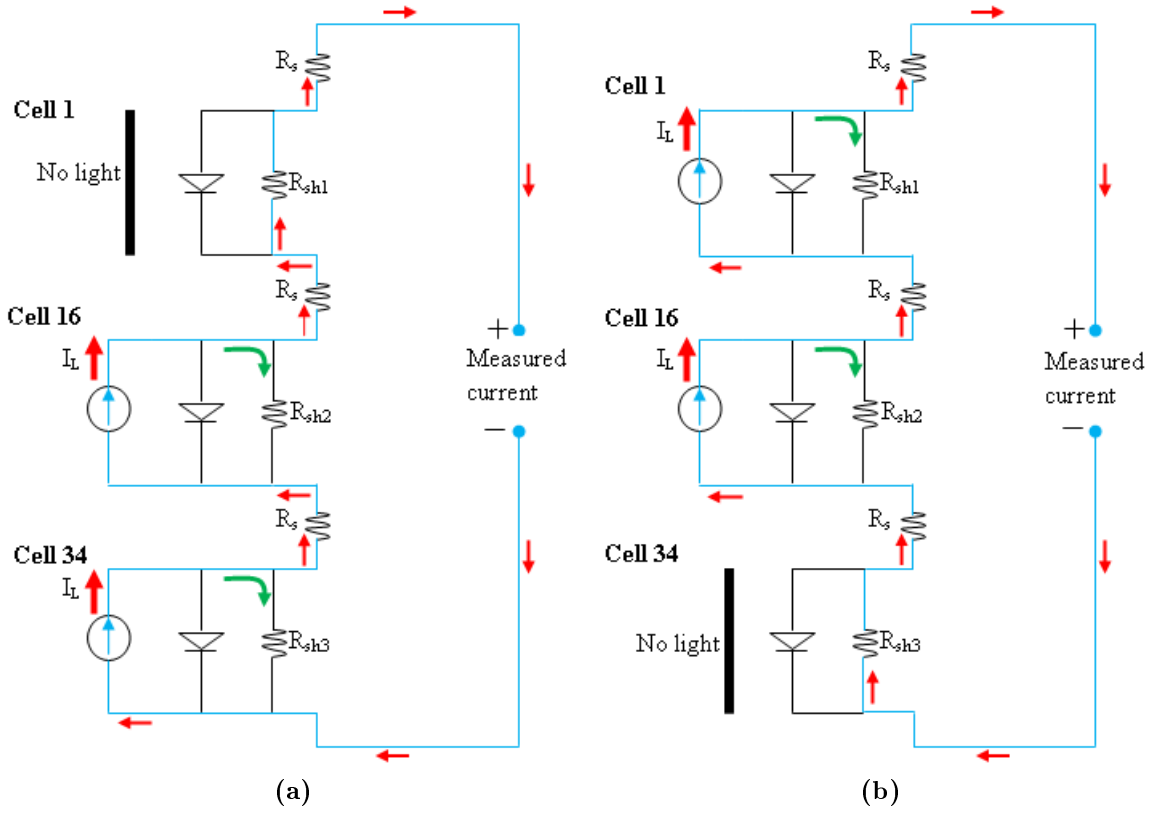

Figure 6.67: Module equivalent circuit model showing how the R_s and R_{sh} of the module are affected by shading (a) a weak cell (b) a strong cell.

It is also interesting to note that the slopes at I_{sc} appear different when the different module cells are shaded. By shading the weakest cell in the group, cell 1, it is observed that the shunting level of the module is different compared to when a strong cell like cell 34 is shaded. When the shunt resistance of cell 1 becomes an active series resistance as a result of shading as shown in Figure 6.67(a), the module shunt resistance is reduced by the value of the shunt resistance of cell 1, R_{sh1}. Since R_{sh1} is comparatively small, excluding it from the module shunt resistance has little effect on the overall module shunt resistance. When the shunt resistance of cell 34 becomes an active series resistance due to shading as shown in Figure 6.67(b), the module shunt resistance decreases significantly since R_{sh3} is comparatively high.

Another feature of interest is the crossing of the I-V curves as seen for cells 16 and 34. When a strong cell like cell 34 is shaded, the electrical parameters of the module are reduced significantly, and this puts the module in a highly shunted position. When a comparatively weaker cell such as cell 16 is shaded, the module appears less shunted. Under a highly shunted condition, the module I-V curve crosses one that is under a less shunted condition, and at a higher forward bias voltage the highly shunted I-V curve shows a higher current

than the less shunted one. This observation is consistent with the argument advanced in chapter 2 regarding identification of shunted module cells by use of module forward biasing.

The shunt resistance for each of the module cells was determined from the I-V curves by use of equation 6.2, and a plot of shunt resistance against cell number is shown in Figure 6.68.

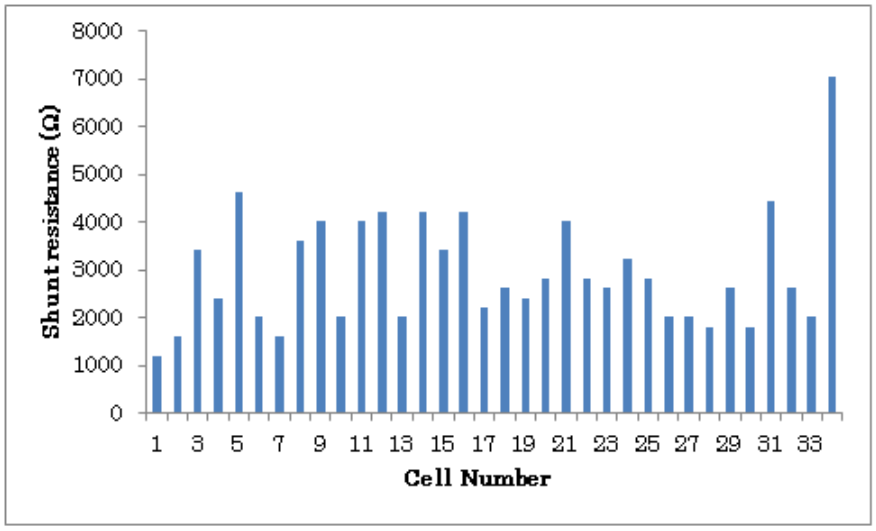

Figure 6.68: Shunt resistance of each cell in the module, determined from the I-V curves of the module under full and partial illumination (one cell shaded)

6.7.3 Relationships between the different methods of investigating module shunt resistance

To determine the relationship between the different methods discussed above, all of which reveal the extent of shunting in the module cells, regression analysis was applied. These methods include the line scans obtained by scanning the module in the dark (dark LBIC), single cell shading and the shunt resistance extraction method.

6.7.3.1 Current drop due to single cell shading and dark LBIC scan

The relationship between the current drop due to the single cell shading method in Figure 6.65 and the dark LBIC method in Figure 6.61 was probed by plotting the two variables as shown in Figure 6.69. It can be seen that the plots show a linear positive trend with a regression line giving R^2 value of 0.72, indicative of a fairly strong correlation between the two methods. However, a large variation is noticed with cell 34, where the results from single cell shading identifies it as the best while the dark LBIC ranks it as 9^{th} best. During dark LBIC

scanning, as explained in section 2.2, the operating point of a cell on which the light spot is incident is shifted into forward bias by the reverse effect created by the non-illuminated cells. Shifting the cell into forward bias puts it into a state of a lower current than its actual generated current. This distortion of the true current generated by the cell is a shortcoming of the dark LBIC method and seems to suggest why cell 34 is behaving the way it is. However, when a very weak cell is being scanned, the non-illuminated cells are barely forced into reverse bias, hence the operating point of the cell being probed remains almost unchanged. This is true as can be seen from the graph, where the two methods show a higher correlation between poorly performing cells compared to good cells. Since the weakest cell in the module is the one that determines the module output current [6], subjecting a cell to a limiting condition by shading gives a more reliable LBIC signal from the cell than the dark LBIC method.

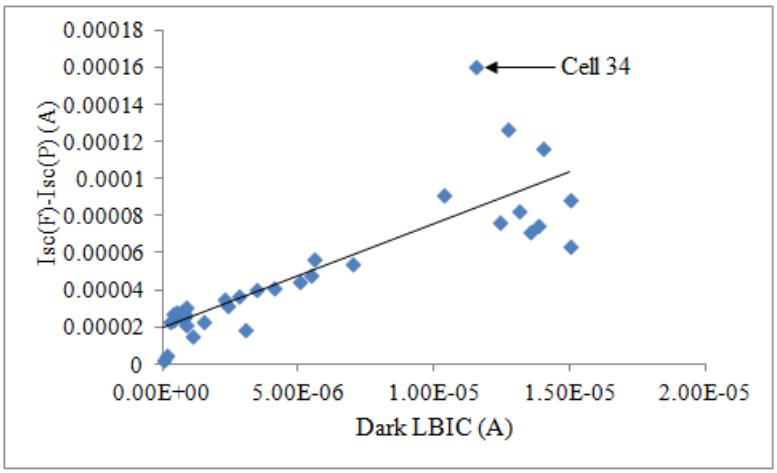

Figure 6.69: The relationship between module cell current, obtained from the difference between the fully and partially illuminated module, and the dark LBIC.

6.7.3.2 Current drop due to single cell shading and R_{sh} extraction from I-V curves

The relationship between current drop due to single cell shading and R_{sh} extracted from the I-V curves was investigated and the result is shown in Figure 6.70. The R^2 value of 0.8262 indicates a very strong correlation between the two methods. It is therefore evident that the module current drop due to single cell shading is highly linked to the shunt resistance of the shaded cell, as extracted from the I-V curves. The two methods are therefore considered useful for quantifying the shunt resistances of cells in encapsulated PV modules.

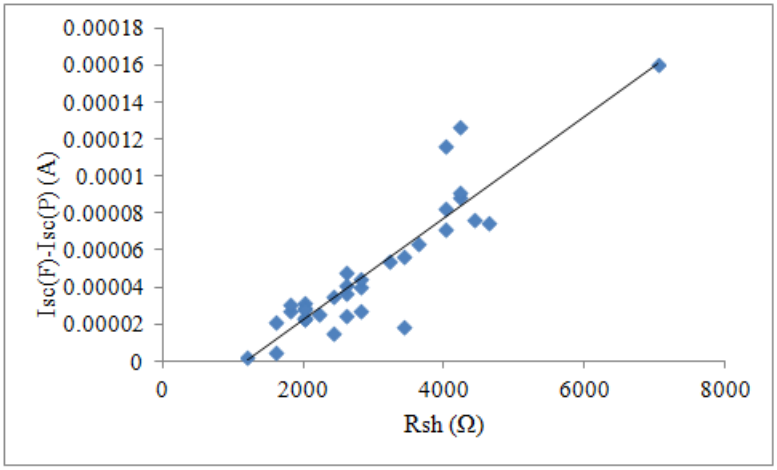

Figure 6.70: The relationship between module cell current and cell shunt resistance, obtained from the fully and partially illuminated module I-V curves.

6.8 Conclusion

Photovoltaic modules which included c-Si, mc-Si, a-Si and CIS, were characterised using the LA-LBIC technique. Results revealed photo-current variation between and within the module cells, with a higher variation appearing between cells. The mono-crystalline silicon module showed a photo-current variation of 100 μA between cells under a white light scan, which is comparatively higher than the variation in photo-current in the other modules scanned with white light. For the crystalline silicon technology, variation in photo-current between cells is attributed to mismatch in cell resistances, while variation in photo-current within cells is attributed to individual cell shunts. In thin film modules, the variation in photo-current is expected to originate from the local cell shunts and series resistances developed by the scribing process during module manufacture. By extraction of module point I-Vs, the short circuit current at different points on the module could be quantitatively compared. The striation ring defect was found to be more detrimental under low energy light wavelengths than at higher energy wavelength. The photo-current generated by high energy photons in the vicinity of a crack was found to be less affected by the crack compared to when lower energy photons were used. Results from module I-V characterisation and EL imaging were found to strongly complement the LA-LBIC results. By scanning the module cells at different light intensities, weaker cells were found to experience a higher percentage drop in current when the light intensity was reduced, compared to stronger cells. In the CIS module, a triangular shaped disconnection feature was found to generate current in a reverse direction in the module when light is incident at the feature. The technique of

forward biasing the module at different voltages during scanning was found to be useful in the identification of severely shunted cells in the module. The I-V curves of severely shunted cells were found to cross the I-V curves of less shunted cells, with the severely shunted cells generating a higher current at some forward bias voltage. The decrease in module current due to cell shading was found to result from the shunt resistance of the shaded cell. The module current decrease arising from the individual cell shunt resistances, determined using the methods of cell shading and dark LA-LBIC, were found to be strongly correlated.

Chapter 7

Further application of LA-LBIC measurements to characterise concentrator photovoltaic (CPV) modules

7.1 Introduction to concentrator photovoltaic technology

A concentrator photovoltaic module is a combined system consisting of the concentrating optics (primary and secondary optical elements) and a III-V multi-junction (MJ) solar cell, all working together as a unit. The primary optical element is a Fresnel lens (collector) which collects light over a large area and focuses it onto the secondary optical element. The secondary optical element then refracts light incident on it onto the solar cell (receiver). The main focus of CPV is to utilise a small amount of the expensive high quality multi-junction solar cell to absorb as much as possible of the different solar light wavelengths in order to generate high power. By using a high quality solar cell under a high concentration of solar light, a high power output per module active area is achievable. Characterisation of the combined CPV system is therefore important in evaluating the device performance

7.2 CPV current status

Presently, the efficiencies for 3-junction (3J) and 4-junction (4J) cells are 44.4% and 45.7% [91], respectively, while the module efficiencies for 3J and 4J are 35.9% and 38.9% [139],

respectively. Despite the achievement of higher efficiencies, many leading CPV companies have exited the market as they could not withstand the PV price competition, while others still face the challenge of raising the capital to meet the production cost [140]. A dramatic drop in annual CPV capacity installation from 2012 to 2015, as a result of many companies shutting down, is shown in Figure 7.1 [140]. Both high concentrator photovoltaic (HCPV) and low concentrator photovoltaic (LCPV) are considered.

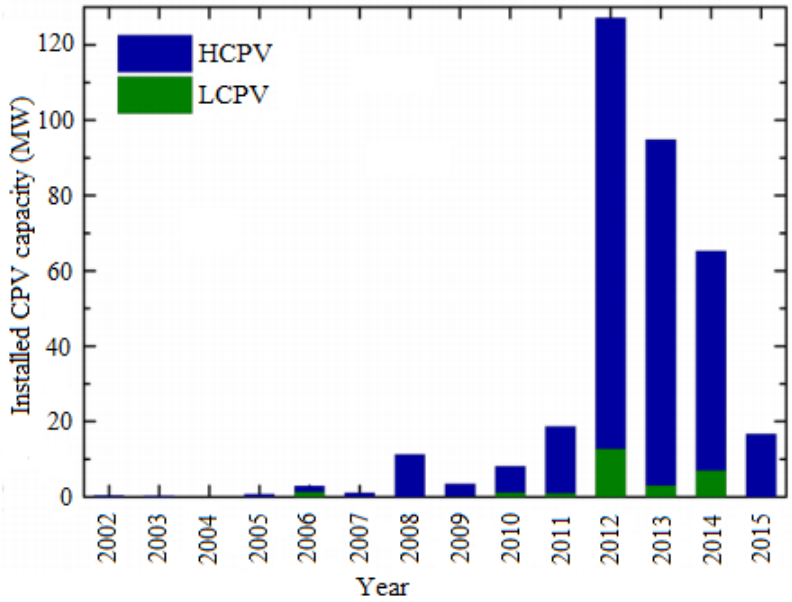

Figure 7.1: Global yearly CPV capacity installation.

7.3 CPV system design

The CPV module operates as a combined system of a multi-junction cell and concentrating optics. The concentrating optics consists of the primary optical element (POE), usually a Fresnel lens and the secondary optical element (SOE). Details about the multi-junction cell and the concentrating optics are presented below.

7.3.1 III-V Multi-junction PV cell

The III-V multi-junction cell is preferred for use in CPV systems because the band gap energy of the constituting sub-cells is tuned to absorb a particular section of wavelengths of the solar spectrum. The entire stack of sub-cells is therefore able to absorb a large section of wavelengths of the solar spectrum, making it possible to achieve a high efficiency. In a

MJ cell, the sub-cells are arranged in descending order of band gap energies from top to bottom. The high energy photons are absorbed in the top layer, moderate energy photons in the middle layer while the low energy photons are absorbed in the bottom cell. For a 3J cell the stack from top to bottom may consist of GaInP/GaInAs/Ge with band gap energies 1.86 eV, 1.40 eV and 0.65 eV, respectively. Figure 7.2 shows the structure and the equivalent electrical circuit of a triple junction cell [53].

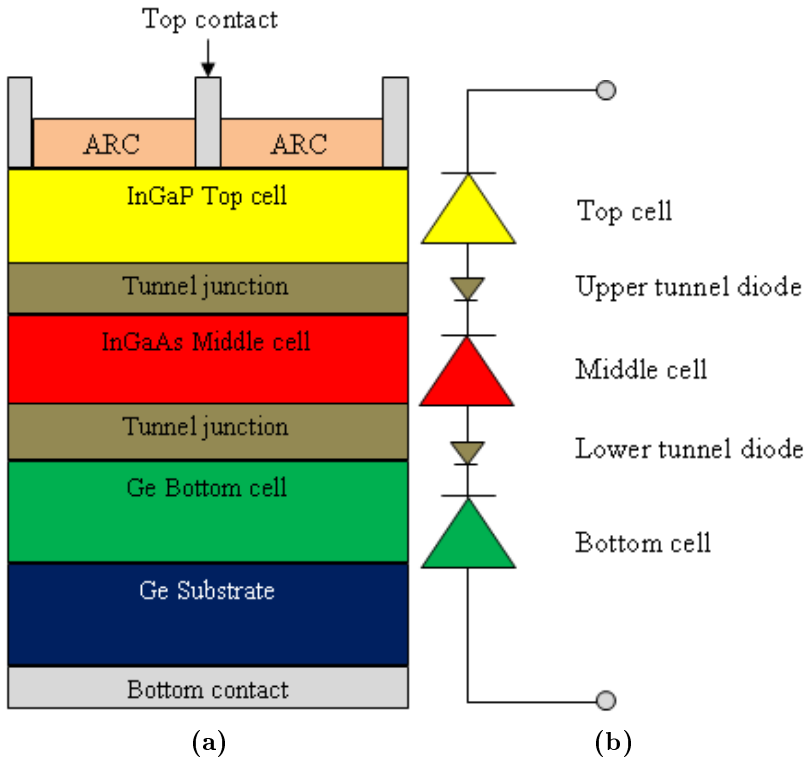

Figure 7.2: A triple junction cell showing (a) Structure (b) Equivalent electrical circuit.

When the sub-cells in a multi-junction solar cell are grown on top of each other, reverse bias pn juctions are created at the interface between the sub-cells [41], shown by dotted circles in Figure 7.3. These reverse bias pn junctions block the current flow from one sub-cell to the other. In order to mitigate this effect, the layers on either side of these reverse bias pn juctions are heavily doped and this has the effect of reducing the depletion layer width so that charge carriers can tunnel through the junction. Hence these reverse bias pn junctions are referred to as tunnel diodes.

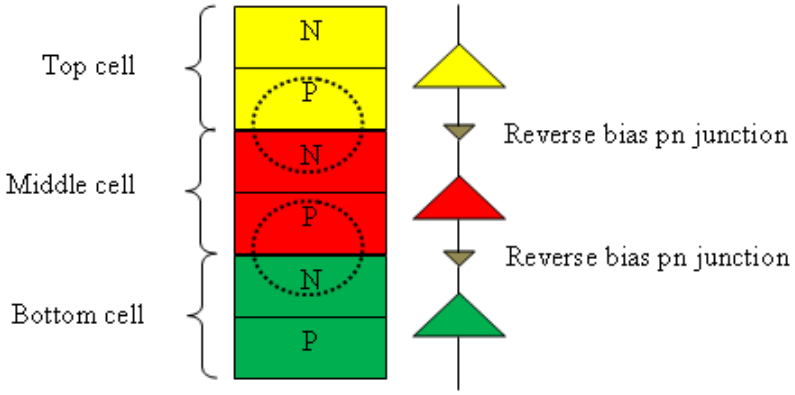

Figure 7.3: The different sub-cells in a multi-junction cell showing how reverse bias *pn* junctions develop between the sub-cells.

7.3.2 CPV concentrating optics

Light concentration on the receiver (MJ cell) is achieved by use of POE and SOE. The POE collects light over a large area and refracts it onto the SOE, which then uniformly distributes it onto the receiver. The MJ cell ensures that a high percentage of photons with appropriate energies that are incident on it are absorbed.

Concentration of solar light in CPV, which entirely depends on the effectiveness of the concentrating optics, is crucial for device high power generation. The CPV optics work better with direct light, therefore a two-axis light tracker is required to work in tandem with the concentrating optics. The photograph and the schematic diagram of the POE (Fresnel lens) is shown in Figure 7.4.

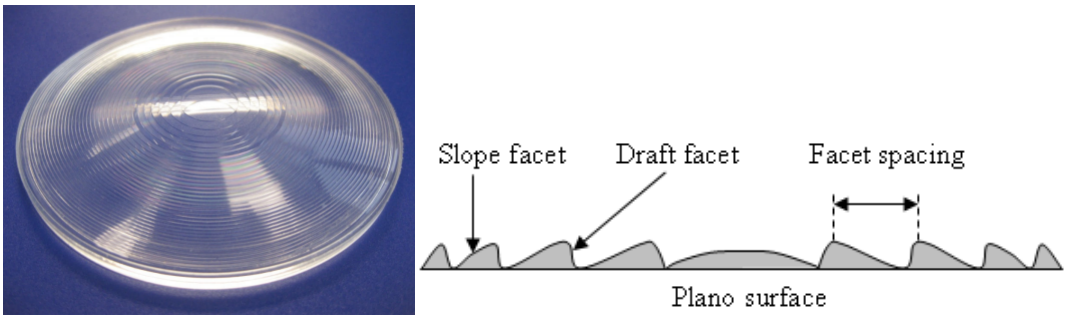

Figure 7.4: (a) Photograph and (b) Schematic diagram of a CPV Fresnel lens.

The Fresnel lenses used in CPV are usually made of polymethyl methacrylate (PMMA), also known as acrylic. Close to the centre of the Fresnel lens, the facets or grooves are almost

parallel to the plano surface while the inclination of the facets becomes steeper towards the edges of the lens. The Fresnel lens collects light and concentrates it onto the SOE as shown in Figure 7.5. The aperture of the SOE is positioned at the focal point of the POE, so that the light refracted on it can be uniformly distributed on the receiver which is attached to its lower bottom.

Figure 7.5 shows how the light rays are concentrated by the POE (collector) onto the SOE and finally onto the MJ solar cell (receiver).

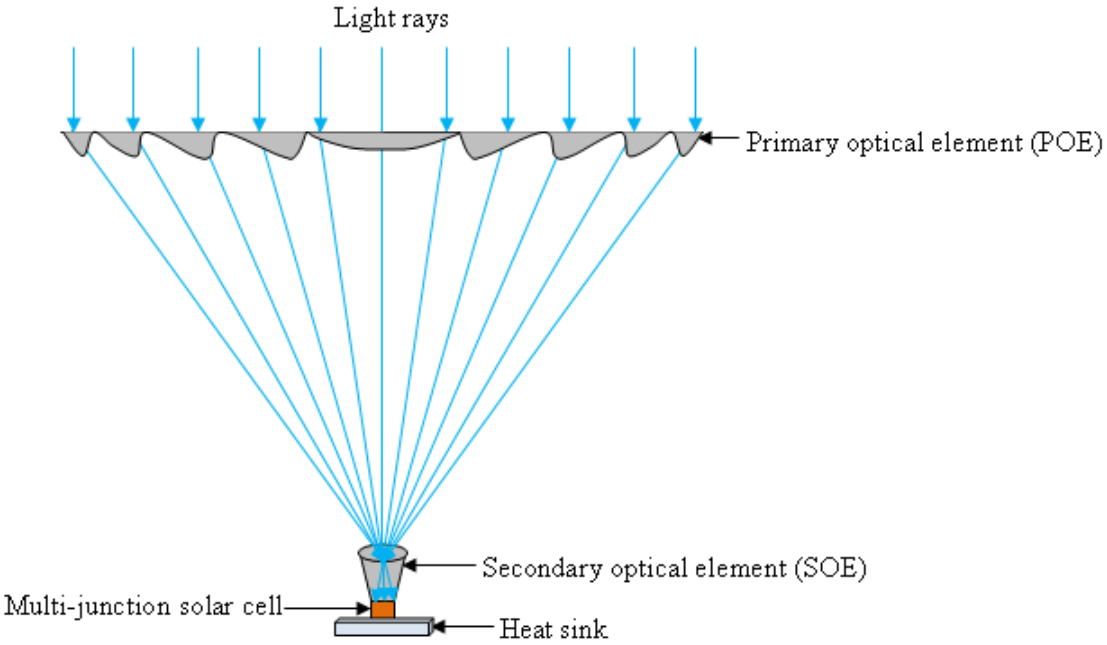

Figure 7.5: Concentration of light on the MJ solar cell by CPV optics.

The CPV system utilises the fact that changing the light intensity incident on a PV cell changes all the solar cell parameters. By increasing the intensity of light incident on a solar cell, a higher power can be obtained from the cell. At high light intensities, a lot of heat is generated, so the multi-junction cell is embedded in a heat sink to dissipate the generated heat.

7.4 Optical losses in Fresnel lenses

One of the major sources of optical loss in a Fresnel lens arises from the scattering of light from the valley (draft facet), tip or back side of the facets, indicated by rays 1, 2 and 3 respectively, as shown in Figure 7.6. Rays of light P and Q in Figure 7.6 represent reflected

light at the air-lens and lens-air interfaces respectively. The incident and refracted angles at the lens-air interface are θ_i and θ_r respectively. The area indicated by the red circle has been magnified to show the reflection losses that occur at the lens-air interface. This area acts as a Fresnel prism. Fresnel reflection, R, of light incident at the surface of a dielectric material is given by the equation 7.1 [141]:

$$R = \frac{1}{2}\left[\frac{sin^2(\theta_i - \theta_r)}{sin^2(\theta_i + \theta_r)} + \frac{tan^2(\theta_i - \theta_r)}{tan^2(\theta_i + \theta_r)}\right] \tag{7.1}$$

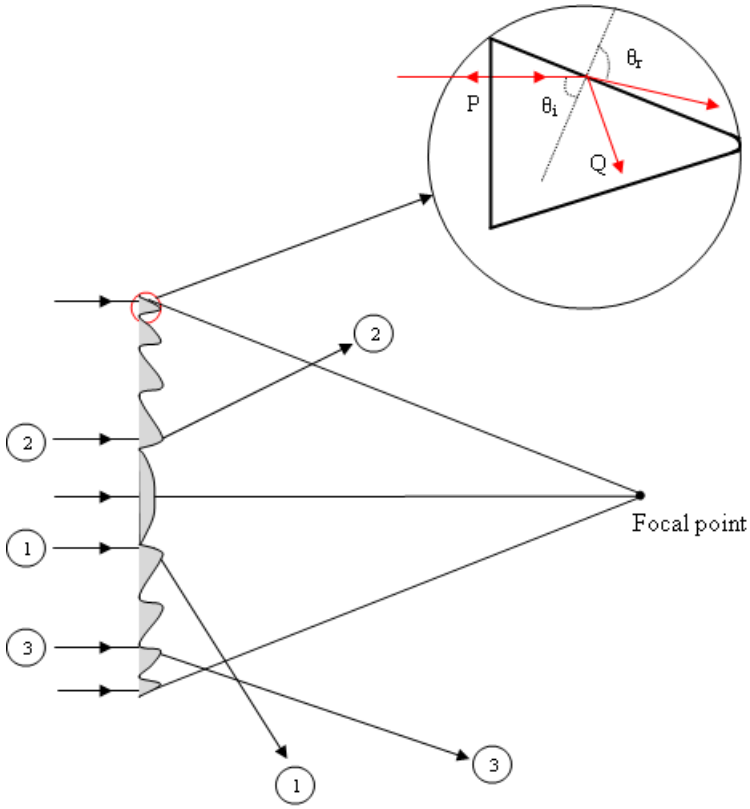

Figure 7.6: Fresnel lens optical losses due to scattering and reflection.

The magnitude of the loss due to reflection is a function of the angle of incidence, θ_i, and for the case of unpolarised light, the relationship between reflectance and angle of incidence for PMMA as determined by Wallhead [142] is shown in Figure 7.7.

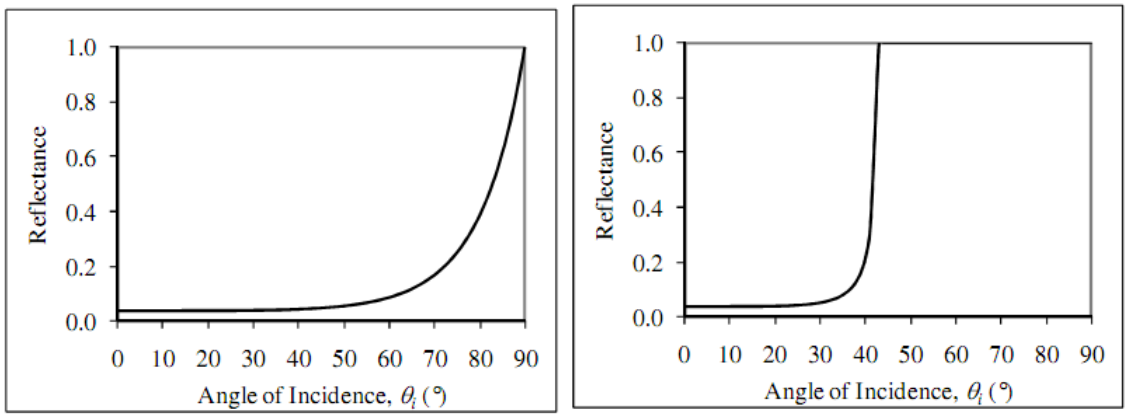

(a) Light from air to PMMA. **(b)** Light from PMMA to air.

Figure 7.7: Reflectance at the PMMA-air interface [142].

Diffraction is another source of optical loss in a Fresnel lens. The fraction of the light energy that spill off due to diffraction by the facets of a Fresnel lens of focal length, f_{lens}, radius, r_{lens} and pitch, Δr, is approximated as [143, 144]:

$$\frac{P_{spilled}}{P_o} \approx \frac{4\sqrt{C_{geo}}}{5\pi k \triangle r} \frac{(1+tan^2\phi)^{\frac{5}{2}} - 1}{tan^3\phi} \tag{7.2}$$

Where C_{geo} represents the geometrical concentration (target area divided by lens aperture), k is the wavenumber of the incident light and $tan\phi = {}^{r_{lens}}/_{f_{lens}}$.

It can be seen from equation 7.2 that diffraction loss is inversely proportional to the prism pitch, implying that Fresnel lenses with gradually decreasing facets from the centre to the edges encounter a higher diffraction loss at the edges where the prisms get smaller.

7.5 Set-up for investigating a combined CPV module

In this study, the LA-LBIC measurement technique was applied in the characterisation of a CPV module by illuminating the Fresnel lens point-by-point while measuring the photocurrent generated at the receiver. When scanning a CPV module, the Fresnel lens is placed above the laser and this facilitates positioning of the light spot at the point of interest on the lens, as the lens is transparent and the spot can be conveniently viewed from above. The schematic and the photograph of the set-up is presented in Figure 7.8. The secondary optical element is positioned at the focal point of the Fresnel lens by varying the position of the Fresnel lens holder.

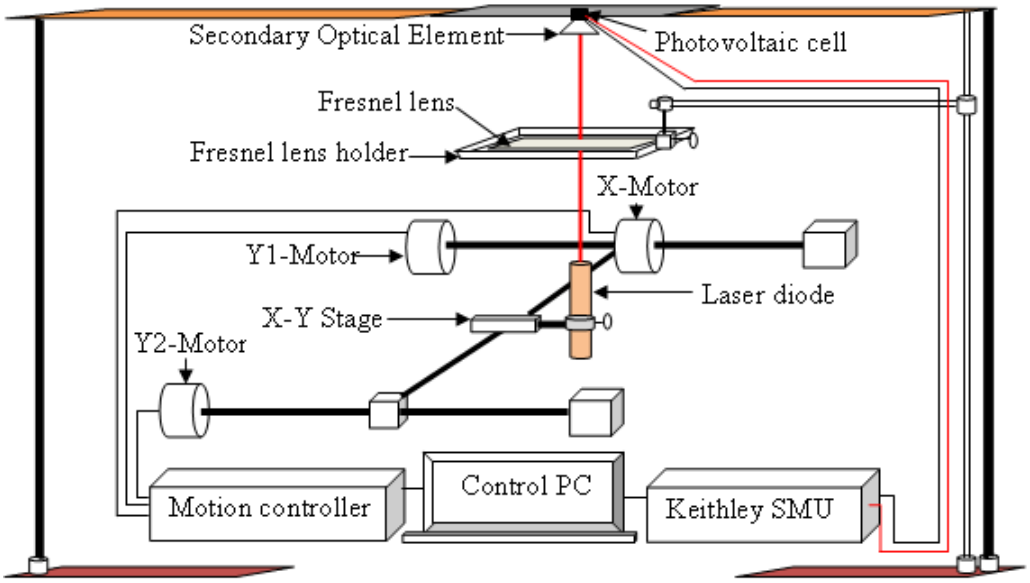

(a)

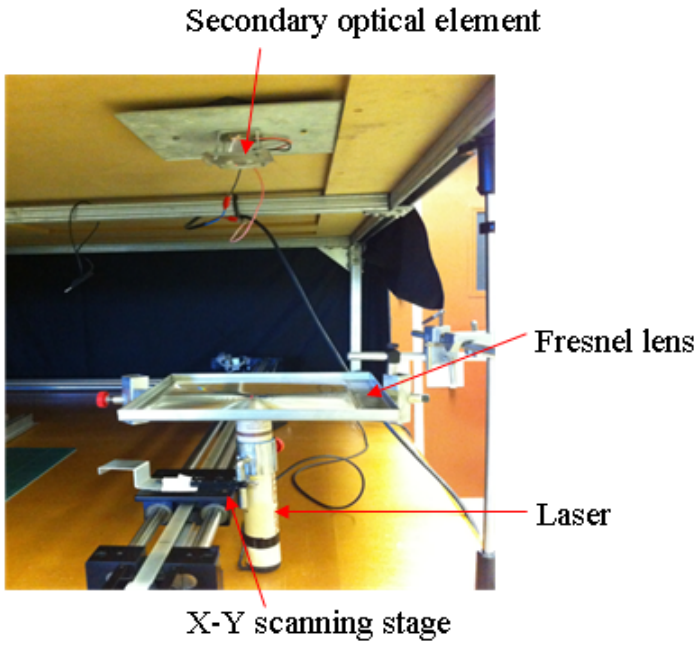

(b)

Figure 7.8: The LA-LBIC system used for CPV Fresnel lens scanning showing (a) the schematic diagram (b) the photograph.

7.6 LA-LBIC scans of CPV module

The CPV module is a unit made up of the POE, SOE and the MJ cell as reviewed previously. The measured photo-current at the MJ cell is therefore dependent on the performance

of the POE and SOE, as well as the MJ cell. It should be noted that since the device operates as a unit, the performance of each constituting element cannot be investigated separately. However, by using different POEs (Fresnel lenses) while the SOE and MJ cell remain unchanged, the LA-LBIC features which are inherent in the Fresnel lenses or have their origin from either the SOE or MJ cell can be revealed. LA-LBIC features which appear different when different Fresnel lenses are used can be attributed to originate from the Fresnel lenses, while features which appear identical may be due to either the SOE or the MJ cell.

In this section, the results obtained by using two Fresnel lenses on the same CPV module are presented and discussed. Both Fresnel lenses have varying facet sizes (1-15 mm), with the facet sizes gradually decreasing from the centre towards the edges. Fresnel lens 1 has been used in a previous CPV system, while Fresnel lens 2 is new. Measurements were performed using laser light of wavelength 448 nm and power of 5 mW. Line scans and area scans were performed to probe the photo-current distribution of the CPV module over the Fresnel lens surface. Line scans were executed on the plane of the Fresnel lens along the x- and y-direction, passing through the centre of the Fresnel lens as illustrated in Figure 7.9.

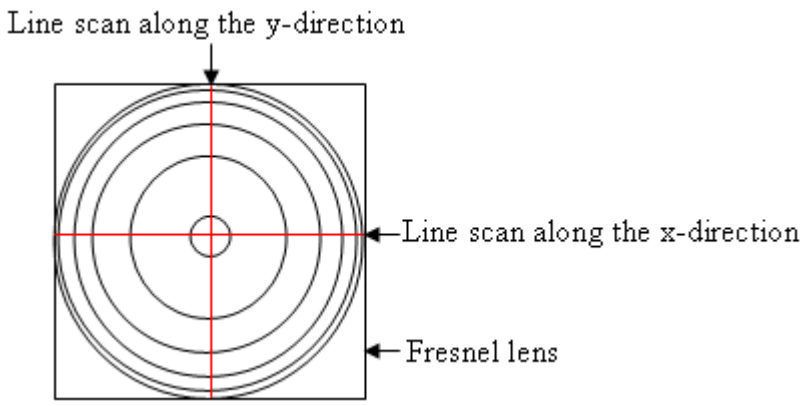

Figure 7.9: Schematic diagram showing how the line scans were performed on the Fresnel lens of a CPV module.

In order to perform the line scan in the x-direction, the light spot is first positioned at the centre of the lens, then moved to the starting point which is half of the distance to be scanned and then the line scan is executed. The light spot is again returned to the centre of the lens before moving it to the starting point for the line scan in the y-direction. Moving the light spot from the centre of the lens to the starting point of each line scan ensures that the two line scans intersect at the centre of the lens and that the scan points along the two axes are equidistant from the centre of the Fresnel lens.

The average values of the two line scans were then used to represent the photo-current

distribution over the Fresnel lens surface.

The line scans for Fresnel lenses 1 and 2 are shown in Figure 7.10 and Figure 7.11 respectively. The dotted circles represent the area, where area scans were performed.

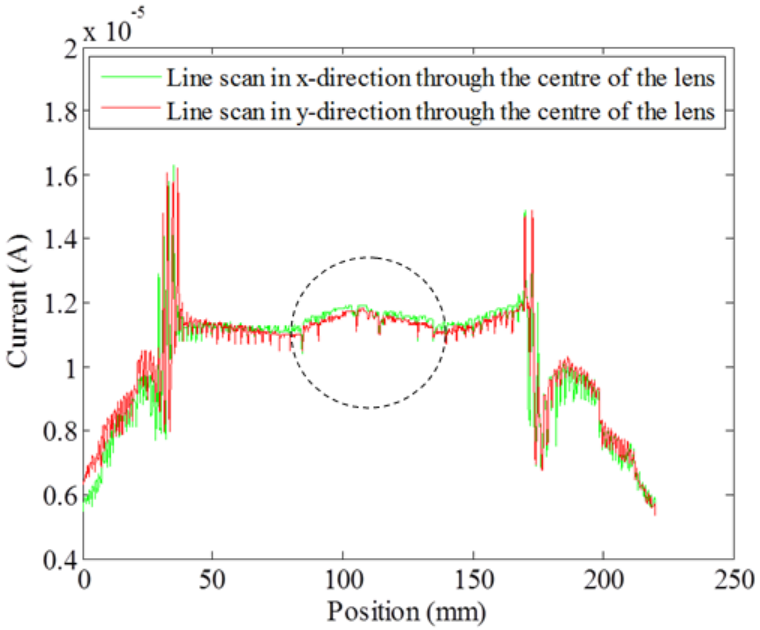

Figure 7.10: Line scans performed on Fresnel lens 1, through the centre of the lens.

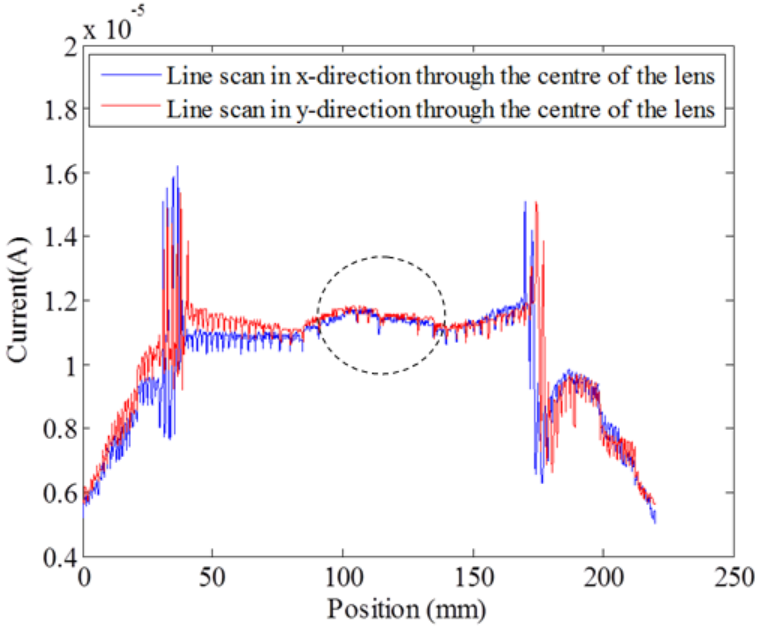

Figure 7.11: Line scans performed on Fresnel lens 2, through the centre of the lens.

In order to extensively investigate the central area (dotted circles) in Figure 7.10 and Figure

7.11 respectively, area scans were performed and the LA-LBIC maps are shown in Figure 7.12 and Figure 7.13 respectively.

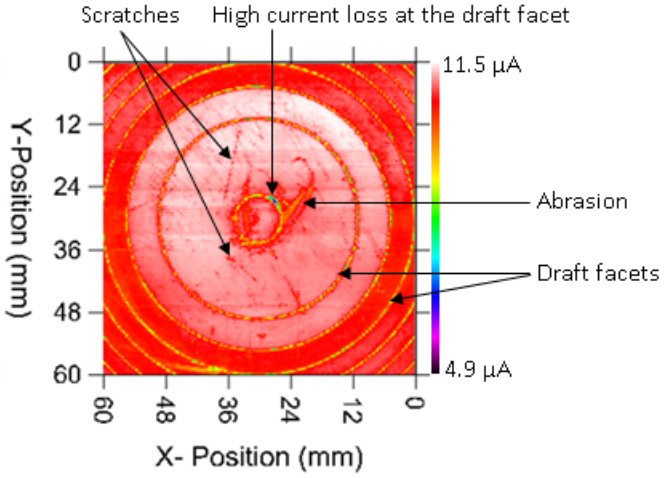

Figure 7.12: LA-LBIC map of the circular area indicated by dotted lines in Figure 7.10.

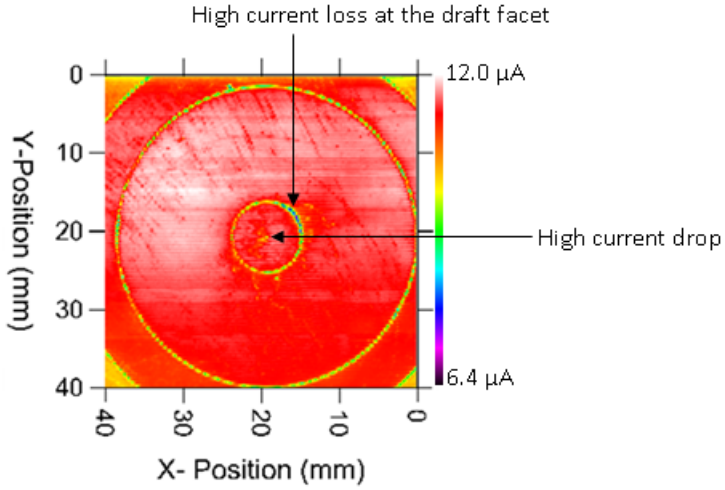

Figure 7.13: LA-LBIC map of the circular area indicated by dotted lines in Figure 7.11.

7.6.1 Variations in photo-generated current

As mentioned earlier, the CPV module operates as a combined system of Fresnel lens, refracting secondary lens and the MJ cell. Therefore, by changing the Fresnel lens while the refracting secondary lens and the MJ cell remain the same facilitates the investigation of the Fresnel lens as well as the combined SOE and MJ cell. Features which appear different in the LA-LBIC maps of the different Fresnel lenses can be attributed to the effect of the lenses

while those which appear alike through both lenses may arise from the refracting secondary lens or the MJ cell. Against this background, the photo-current distribution and the current limiting features in both lenses can be investigated.

7.6.1.1 Across the lens facets

Facets close to the centre of the lens are more effective than those at the edges as seen in the area scans in Figure 7.12 and Figure 7.13. Dielectric reflection loss is inherent in Fresnel lenses and increases from the centre of the lens towards the edges as the angle of the incident light ray on the slope facet increases [141]. Internal reflection losses also increase towards the lens edges where the angle of inclination of the slope facets becomes larger, increasing the angle of incidence of light on the slope facets [142]. Reduced facet spacing (pitch) towards the edges also facilitates diffraction of light where light may spill outside the target [144]. Although in the area maps only small variations in photo-current are observed within individual facets, line scans extracted from the area maps show significant variations.

Figure 7.14(a) shows a line scan extracted from Figure 7.12 at y = 30 mm, while Figure 7.14(b) shows a line scan taken from Figure 7.13 at y = 21 mm. The definite variations in photo-response are clearly observed.

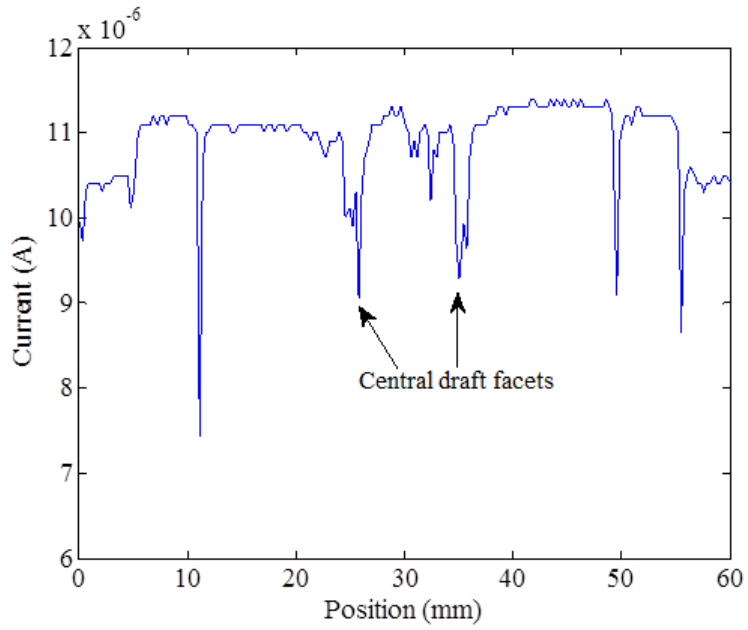

(a)

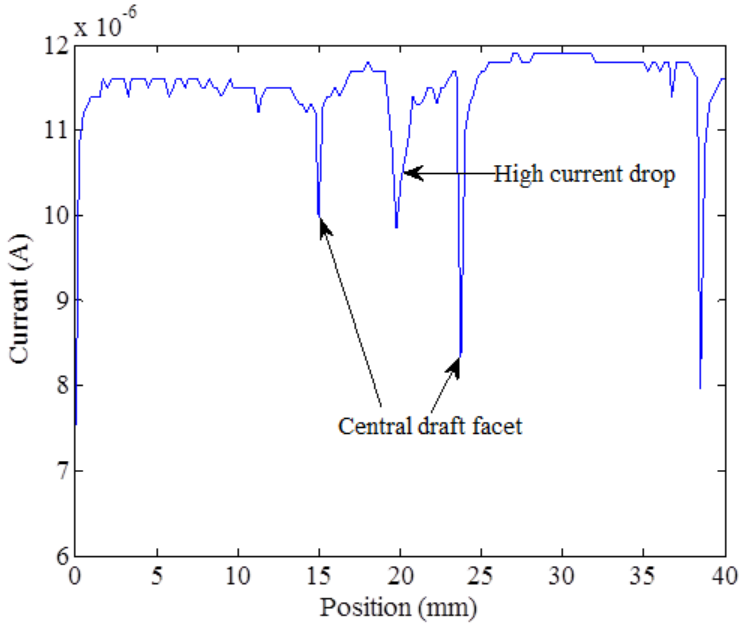

(b)

Figure 7.14: Line scans extracted from (a) Figure 7.12 at position y = 30 mm and (b) Figure 7.13 at position y = 21 mm.

7.6.1.2 At the draft facets

When light is incident at the draft facet, part of it may be scattered and misses the target, leading to a reduction in current. It is observed in Figure 7.13 and Figure 7.14 that some

points on the draft facets experience higher losses than others. This variation is expected because the extent of light scattering at the facets may also vary from point to point. Additionally, dust and dirt collect at the draft facets and since the level of contamination may vary, the consequent optical losses may also differ from point to point. However, it is interesting to note that a high current drop occurs at the same position on the central draft facets of both lenses, as seen in Figure 7.12 and Figure 7.13. The similarity of this current limiting feature in both lenses seems to suggest that its origin could be in either the refracting secondary lens or the MJ cell, since its effect is independent of the Fresnel lens used.

7.6.1.3 Due to scratches and abrasions

Localised low performances are observed at points with scratches and abrasions in Figure 7.12 and Figure 7.13. The refracting ability of a lens depends on its curved surface and therefore any distortion on the surface, such as from scratches and abrasions, reduces the refracting power of the lens. Surface roughness is one of the primary loss mechanisms in Fresnel lenses used in CPV applications [145].

7.6.2 Comparison between Fresnel lens 1 and Fresnel lens 2

In order to compare the photo-current distribution for Fresnel lens 1 and Fresnel lens 2, the average line scans in Figure 7.10 and Figure 7.11 were used. The results are presented in Figure 7.15.

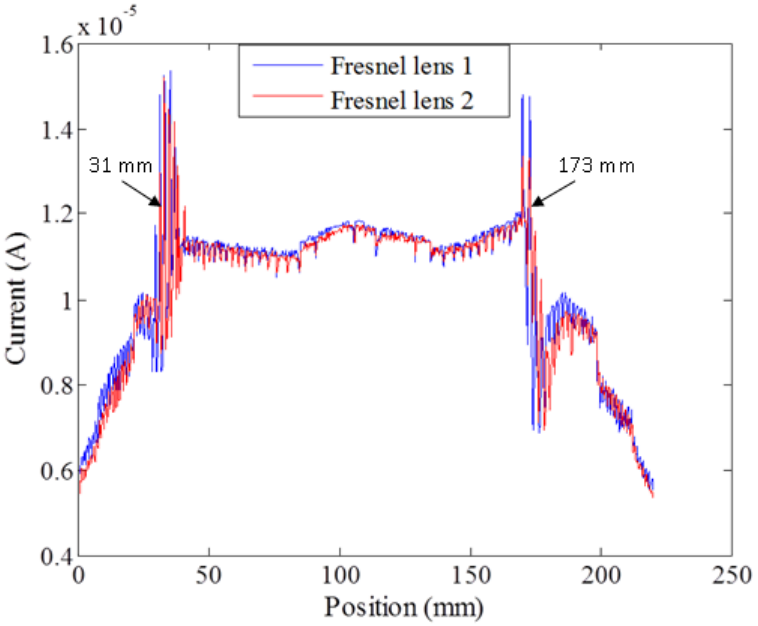

Figure 7.15: Comparison of photo-current distribution in Fresnel lenses 1 and 2 using average values of the line scans in Figure 7.10 and Figure 7.11.

Fresnel lens 1 (used) and Fresnel lens 2 (new) show similar photo-current distribution over their entire surface. It can be noted that both Fresnel lenses have an effective light collection area stretching from 31 mm to 173 mm along one of the sides, translating to 65 % of the total area of the lens. The central facets are observed to generate a higher current than those towards the edges. This could be attributed to dielectric reflection [141], internal reflection [142] and diffraction effects [144], which reduce the photo-current towards the edges. The effects of scratches and abrasions as seen in the area scans seem to not have a significant effect on the photo-current.

7.7 Conclusion

An introduction to CPV technology was given and the current status in terms of cell and module efficiencies, as well as yearly installation capacity, were reviewed. The CPV module design and working principle were described and the optical losses associated with Fresnel lenses were reviewed. The scanning procedure for investigating the combined CPV module was described and the LA-LBIC results presented. Fresnel lens facets close to the centre were found to generate a higher photo-current at the receiver than those towards the edges. About 65% of the area of Fresnel lenses was found to be effective in light collection in terms of the photo-current generated at the receiver. Abrasions and scratches on Fresnel lenses were

identified as some of the current limiting features in CPV modules. The two Fresnel lenses investigated showed insignificant variation in photo-current distribution over their surfaces. The LA-LBIC measurement technique has demonstrated a potential in characterisation of a CPV module.

Chapter 8

Conclusions and Recommendations

8.1 Conclusion

The general objective of this study was to characterise different types of photovoltaic devices using the LA-LBIC measurement technique. The photovoltaic devices investigated were limited to crystalline silicon PV modules (c-Si and mc-Si) thin film PV modules (a-Si and CIS) and finally, CPV modules.

Photovoltaic modules need to exhibit homogeneous electrical properties in order to negate the current mismatch that lowers module performance. Investigation of current uniformity and the different current reducing features in PV modules, which are potential sources of current mismatch, therefore becomes important. In this study, the large area light beam induced current (LA-LBIC) measurement system was used to characterise PV modules.

The LA-LBIC measurement system, with a maximum scanning area of 1.3 m x 1.3 m, has a motorised x-y scanning stage on which a light source is mounted and used to spot-illuminate a PV module point-by-point, while measuring the module output current. The measured photo-current is plotted as a function of position to produce the module's photo-response map. Different forward bias voltages were applied to the module during scanning, allowing for the identification of severely shunted cells in the module.

An equivalent circuit model of a spot-illuminated PV module was used to explain the variation in photo-current in the LA-LBIC maps. Application of the equivalent circuit model of a spot-illuminated PV module to interpret the LA-LBIC maps of crystalline silicon modules, attributed the variation in photo-generated current between cells to current mismatch between series-connected cells. Current mismatch may arise from incorrect cell sorting during the cell stringing and module manufacturing process. Variation in current

within cells was attributed to shunts within individual cells. Application of the model to interpret the LA-LBIC maps of thin film modules attributed the variation in photo-generated current to differences in local cell shunts and series resistances originating from the scribing procedure during cell formation in the manufacturing process. In order to explain the drop in module output current when a module cell was shaded, an equivalent circuit model of a partially shaded PV module was used. The equivalent circuit model of a partially shaded PV module attributed the module current drop due to a shaded cell to the shunt resistance of the shaded cell, and this was found useful in the measurement of the relative strengths of shunt resistances of cells in a PV module.

Different types of LA-LBIC features were detected in the short circuit LA-LBIC maps of the modules investigated. In the c-Si module, striation rings were identified in four cells of the module. A striation ring feature is caused by the presence of oxygen precipitates in the silicon wafers. Oxygen diffuses from the crucible into the molten silicon during the Czochralski manufacturing process. The module point I-V characteristics measured at the striation ring feature under white light illumination revealed a reduction in current of 38%. The LA-LBIC scans of one of the cells with the striation ring feature, using laser light wavelengths of 448 nm, 660 nm and 785 nm, revealed that the feature had no effect on the 448 nm wavelength, and caused a drop in current of 4.8% and 13.4% when the 660 nm and 785 nm wavelengths were used. From this investigation, it was inferred that the striation ring feature is more concentrated in the bulk of the solar cell and is more detrimental to low energy photons. Scans performed under different light intensities showed that the percentage loss in current at the feature is higher at low light intensity and decreased with an increase in light intensity.

In the mc-Si module, cracks were identified and were found to electrically disconnect parts of the cells, leading to current mismatch in the module. Since the mc-Si module cells are wired in series, disconnecting a portion of a module cell leads to current mismatch. These cracks were verified by EL imaging. The module I-V characteristics revealed steps on the vertical leg, confirming the presence of current mismatch in the module. This was attributed to the cracks identified by the LA-LBIC mapping. High current was observed at localised points on the bus bar and cell separation in the LA-LBIC image. This effect is due to diffuse reflection, which leads to multiple reflections between the reflecting surface and the top glass, enabling the light reflected back from the top glass to impinge on the neighbouring active cell material and hence be absorbed.

An electrical disconnection across the cells of a CIS module was identified. Since this module is manufactured by monolithic integration, the disconnection caused the two sections to

operate in parallel. The EL image confirmed the disconnection and the I-V characterisation result revealed a reduction in slope at V_{oc} due to an increase in the module series resistance caused by the disconnection. A closed, triangular-shaped disconnection was also identified in this module, which electrically disconnected the front contact of this area from the module. This unique disconnection configuration was found to cause current in the module to flow in the opposite direction when the light spot was incident within the boundary of the disconnection. In the EL image, this triangular-shaped disconnection appears dark, as for any ordinary current limiting feature. It is recommended that other non-destructive characterisation techniques be used to verify this unique feature.

Module point I-V measurements were used to quantify the photo-generated current at different points on the module. Using photo-generated current data extracted from the module LA-LBIC scans under a fixed module bias voltage was found to be less accurate, as the non-illuminated cells caused the operating point bias voltage of the module cells to shift when scanning from cell to cell. Module point I-V measurements, however, allow photo-generated current at different points of the module to be extracted at a particular bias voltage and this allows different parts of the module to be compared under a similar conditions.

Application of forward bias to the module during scanning was found useful in identification of severely shunted module cells. The current of severely shunted cells increases substantially at a particular forward bias voltage. This is due to the I-V curve of the shunted cell crossing that of the good cell at this forward bias voltage, where the shunted cell generates more current than the good cell, at the same bias voltage. Scanning the module at different light intensities by changing the laser power, was also found useful in identifying highly shunted cells. When a line scan was performed on a module under different light intensities and the percentage drop in current for each module cell computed, severely shunted cells were found to experience a higher percentage drop in current than the good cells.

A method for the measurement of the shunt resistances of cells in an encapsulated module that involved illuminating the module and shading each cell one at a time, while measuring the module I-V characteristics was devised. The method involves measuring the I-V curves of a fully and partially illuminated PV module, from which the module I_{sc} of the shaded portion can be obtained by subtraction. The short circuit current drop obtained by subtracting the short circuit current of the partially shaded module, $I_{sc(P)}$, from that of the fully illuminated module, $I_{sc(F)}$, was found to be directly proportional to the shunt resistance of the shaded cell. By measuring the current drop for all the module cells due to partial shading, the shunt resistances of the cells in the module could be compared. In order to obtain the

shunt resistance of module cell n, the shunt resistance extracted from the I-V curve of the illuminated module with cell n shaded, $R_{sh(n\text{-}shaded)}$, was subtracted from the shunt resistance extracted from the I-V curve of the fully illuminated module, $R_{sh(full\text{-}illum)}$. A strong correlation was found between the different methods investigated. Current drop during cell shading was found to be related to shunt resistances and this was confirmed by dark LBIC measurements.

The LA-LBIC technique was applied to characterise a combined CPV module by scanning the primary optical element (Fresnel lens) while measuring the photo-current at the receiver. Fresnel lens facets close to the centre were found to generate a higher photo-current at the receiver than those towards the edges. The reduced photo-current towards the edges was attributed to diffraction losses due to reduced facet spacing, dielectric reflection loss and internal reflection loss which increased towards the edges. About 65% of the area of the Fresnel lenses investigated was found to be effective in light collection in terms of the photo-current generated at the receiver. Abrasion and scratches on Fresnel lenses were identified as some of the current limiting features in a CPV module.

8.2 Challenges /Limitations

The shift in the voltage of the illuminated cell from the preset module voltage during LBIC scanning in the dark, which results as a consequence of the non-illuminated cells operating in the reverse bias region, complicates the interpretation of LBIC data, since as a result of the differences in cell resistances, the conditions are bound to vary from cell to cell during scanning.

The use of an aperture at the light exit of a laser diode to obtain the desired spot size has a disadvantage in that it blocks part of the light, leading to a reduced power and intensity. Therefore, for high resolution scanning which requires an extremely small spot diameter, focusing optics should be used. However, the scanning of large PV modules can easily be done by moving the scanning light source while the module is stationary, making it difficult to use the focusing optics as moving them would disorganise the settings. To move large PV modules during scanning would also require powerful stepper motors.

Scanning of a large module at a high resolution requires that the light spot diameter should be small and therefore the scanning step size should be even smaller. This means a very large number of scan points and hence a long period of time is required to complete the scan.

8.3 Recommendations for future work

It is proposed that during LA-LBIC measurements, the cell being scanned should be placed under a complete limiting condition to ensure that it is the one responsible for the module output current. This can be achieved by applying background illumination to the whole module while the cell under investigation is covered with a band pass filter that blocks the background light but allows the scanning laser beam's light to pass through.

The LA-LBIC measurement technique should be used to characterise other PV module technologies and defects which are not considered in this work.

References

[1] United Nations. Department of Economic and Social Affairs, Population Division 2015. World Population Prospects: The 2015 Revision, Key Findings and Advance Tables. *Working Paper No. ESA/P/WP.241*, 2015.

[2] International Energy Agency. Renewable energy: Medium-term market report. Technical report, 2015.

[3] N. S. Lewis and D. G. Nocera. Powering the Planet: Chemical Challenges in Solar Energy Utilisation. In *National Academy of Sciences of the United States of America*, volume 103, pages 15729–15735, October 2006.

[4] International Energy Agency. Technology Roadmap: Solar photovoltaic energy, 2014 Edition,OECD/IEA, Paris. Technical report, 2014.

[5] K. Wilson, D. De Ceuster, and R. A. Sinton. Measuring the effect of cell mismatch on module output. *Photovoltaic Energy Conversion, Conference Record of the 2006 IEEE 4th World Conference*, 1:916–919, 2006.

[6] P. Vorasayan, T. R. Betts, and R. Gottschalg. Limited laser beam induced current measurements: a tool for analysing integrated photovoltaic modules. *Measurement Science and Technology*, 22:1–7, 2011.

[7] D. K. Schroder. *Semiconductor material and device characterisation*. John Wiley & Sons, Hoboken, New Jersey, third edition, 2006.

[8] M. Köntges, S. Kajari-Schröder, and I. Kunze. Cell cracks measured by UV fluorescence in the field. In *European Photovoltaic Solar Energy Conference*, pages 1–8, 2012.

[9] J. Haunschild, J. Broisch, I. E. Reis, and S. Rein. Quality control of czochralski grown silicon wafers in solar cell production using photoluminescence imaging. In *European Photovoltaic Solar Energy Conference*, pages 1025–1030, 2011.

[10] P. Chaturvedi, B. Hoex, and T. M. Walsh. Broken metal fingers in silicon wafer solar cells and PV modules. *Solar Energy Materials and Solar Cells*, 108:78–81, 2013.

[11] S. Kajari-Schrsder, I. Kunze, and M. Ksntges. Criticality of cracks in pv modules. *Energy Procedia*, 27:658–663, 2012.

[12] D. E. Sawyer and H. K. Kessler. Laser scanning of solar cells for the display of cell operating characteristics and detection of cell defects. *Electron Devices, IEEE Transactions on*, 27(4):864–872, 1980.

[13] J. F. Hiltner and J. R. Sites. High resolution laser stepping measurements on polycrystalline solar cells. *European Photovoltaic Solar Energy Conference*, 1(3):630–633, 2000.

[14] B. Plunkett and P. G. Lasswell. Laser scanning of experimental solar cells. In *Role of electro-optics in photovoltaic energy conversion*, pages 142–147, 1980.

[15] A. C. Ribes, S. Damaskinos, H. F. Tiedje, A. E. Dixon, and D. E. Brodie. Reflected-light, photoluminescence and OBIC imaging of solar cells using a confocal scanning laser MACROscope/microscope. *Solar Energy Materials and Solar Cells*, 44:439–450, 1996.

[16] J. Carstensen, G. Popkirov, J. Bahr, and H. Foll. CELLO: an advanced LBIC measurement technique for solar cell local characterization. *Solar Energy Materials and Solar Cells*, 76(4):599 – 611, 2003.

[17] F. J. Vorster and E. E. van Dyk. Bias-dependent high saturation solar LBIC scanning of solar cells. *Solar Energy Materials and Solar Cells*, 91(10):871 – 876, 2007.

[18] J. R. Sites and T. J. Nagle. LBIC analysis of thin-film polycrystalline solar cells. In *Photovoltaic Specialists Conference, 2005. Conference Record of the Thirty-first IEEE*, pages 199–204, 2005.

[19] M. B. Rabha, W. Dimassi, M. Bouaicha, H. Ezzaouia, and B. Bessais. Laser-beam-induced current mapping evaluation of porous silicon-based passivation in polycrystalline silicon solar cells. *Solar Energy*, 83:721–725, 2009.

[20] V. Parra, B. Moralejo, M. A. González, J. Jiménez, O. Martínez, J. Gutiérrez, and E. Boillos. LBIC and reflectance mapping of multicrystalline silicon solar cells. *Electronic Materials*, 39(6):663–670, 2010.

[21] M. K. Munji, W. Okullo, E. E. van Dyk, and F. J. Vorster. Local device parameter extraction of a concentrator photovoltaic cell under solar spot illumination. *Solar Energy Materials and Solar Cells*, 94(12):2129–2136, 2010.

[22] G. A. Kulkarni. Laser Beam Induced Current (LBIC) Instrumentation for Semiconductor Research. *International Journal of Engineering and Management Sciences*, 4(2):102–107, 2013.

[23] A. Ibrahim. LBIC measurement scan as a diagnostic tool for silicon solar cell. *Jounal of Basic and Applies Scientific Research*, 1(3):215–221, 2011.

[24] N. Kwarikunda, E. E. van Dyk, F. J. Vorster, W. Okullo, and M. K. Munji. Application of LBIC measurements for characterisation of triple junction solar cells. *Physica B: Condensed Matter*, 439:122–125, 2014.

[25] M. Bolkalic, M. Jankovec, and M. Topic. Solar cell efficiency mapping by LBIC. In *45th International Conference on Microelectronics, Devices and Materials & The Workhop on Advanced Photovoltaic Devices and Technologies*, pages 269–273, 2009.

[26] R. J. Matson, K. A. Emery, I. L. Eisgruber, and L. L. Kazmerski. The large scale laser scanner: millicharacterisation of photovoltaic devices and modules. *European Photovoltaic Solar Energy Conference*, pages 1222–1225, 1994.

[27] T. Michel, R. Gottschalg, and D.G. Infield. Large area laser scanning of amorphous silicon modules. In *European Photovoltaic Solar Energy Conference*, pages 2522–2524, 2004.

[28] D. A. Redfern, E. P. G. Smith, C. A. Musca, J. M. Dell, and L. Faraone. Interpretation of current flow in photodiode structures using laser beam-induced current for characterization and diagnostics. 53(1):23–31, 2006.

[29] G. Micard, S. Seren, and G. Hahn. Quantitative interpretation of light beam induced current contrast profiles for different diffusion lengths on either side of a grain boundary. In *European Photovoltaic Solar Energy Conference*, pages 416–420, 2008.

[30] C. Donolato. Beam induced current characterisation in polycrystalline semiconductors. *Springer Series in Solid-State Sciences*, 57:138–154, 1985.

[31] S. Dongaonkar, S. Loser, E. J. Sheets, K. Zaunbrecher, R. Agrawal, T. J. Marks, and M. A. Alam. Universal statistics of parasitic shunt formation in solar cells, and its implications for cell to module efficiency gap. *Energy Environ. Sci.*, 6:782–787, 2013.

[32] A. Kaminski, O. Breinstentein, J. P. Boyeaux, and P. Rakotoniaina. Light beam induced current and infrared thermography studies of multicrystalline silicon solar cells. *Journal of Physics : Condensed Matter*, 16:S9–S18, 2004.

[33] L. A. Kosyachenko, X. Mathew, P. D. Paulson, V. Ya Lytvynenko, and O. L. Maslyanchuk. Optical and recombination losses in thin-film $Cu(In, Ga)Se_2$ solar cells. *Solar Energy Materials and Solar Cells*, 130:291–302, 2014.

[34] S. M. Dasari, P. Srivastav, R. Shaw, S. Saravanan, and P. Suratkar. Optimization of cell to module conversion loss by reducing the resistive losses. *Renewable Energy*, 50:82–85, 2013.

[35] J. Muller, D. Hinken, S. Blankemeyer, H. Kohlenberg, U. Sonntag, K. Bothe, T. Dullweber, M. Kontges, and R. Brendel. Resistive power loss analysis of PV modules made from halved 15.6 cm x 15.6 cm silicon PERC solar cells with efficiencies up to 20 percent. *IEEE Journal of Photovoltaics*, 5(1):189–194, 2015.

[36] A. Goetzberger, J. Knobloch, and B. Voss. *Crystalline Silicon Solar Cells*. John Wiley & Sons, Chichester, Newyork, 1998.

[37] C. Honsberg and S. Bowden. *PVCDROM, Retrieved: 29/3/2017, at http://pveducation.org/pvcdrom/design/voltage-losses-due-to-recombination*.

[38] S. Yilmaz, A. Yilmaz, M. Gunes, and H. R. Ozcalik. Two diode model performance analysis of photovoltaic panels. *International Journal of EngineeringTrends and Technology*, 4(7), 2013.

[39] N. M. Thantsha. *Spatially resolved opto-electric measurements of photovoltaic materials and devices*. PhD thesis, Nelson Mandela Metropolitan University, 2010.

[40] M. Wolf and H. Rauschenbach. Series resistance effects on solar cell measurements. *Advanced Energy Conversion*, 3:455–479, 1963.

[41] J. L. Gray. *Handbook of Photovoltaic Science and Engineering*. John Wiley & Sons Ltd., Chichester, England, 2003.

[42] K. Ishaque, Z. Salam, and H. Taheri. Simple, fast and accurate two-diode model for photovoltaic modules. *Solar Energy Materials and Solar Cells*, 95(2):586–594, 2011.

[43] J. Sites. Device physics of thin-film polycrystalline cells and modules. Annual Subcontract Report: NREL/TP-451-7709, National Renewable Energy Laboratory, 1994.

[44] J. Reinhardt, P. Apilo, B. Zimmermann, S. Rousu, and U. Würfel. Determining the photocurrent of individual cells within an organic solar module by LBIC and the filtering approach: Experiments and simulations. *Solar Energy Materials and Solar Cells*, 134:157–164, 2015.

[45] PVCDROM. *Shading of a module. Retrieved: 30/04/2016 at www.pveducation.org/pvcdrom/modules/shading.*

[46] M. C. Alonso-García, J. M. Ruiz, and W. Herrmann. Computer simulation of shading effects in photovoltaic arrays. *Renewable Energy*, 31(12):1986–1993, 2006.

[47] E. E. van Dyk and E. L. Meyer. Analysis of the effect of parasitic resistances on the performance of photovoltaic modules. *Renewable Energy*, 29(3):333–344, 2004.

[48] E. L. Meyer and E. E. van Dyk. The effect of reduced shunt resistance and shading on photovoltaic module performance. *Thirty-first IEEE Photovoltaic Specialists Conference, 2005*, pages 1331–1334, 2005.

[49] K. Emery. Nondestructive performance characterisation techniques for module reliability. In *National Center for Photovoltaic and Solar Program Review Meeting*, pages 1–4. National Renewable Energy Laboratory, 2003.

[50] S. W. Glunz, R. Preu, and D. Biro. Crystalline Silicon Solar Cells: State-of-the-Art and Future Developments. *Comprehensive Renewable Energy*, pages 353–387, 2012.

[51] A. Blakers, N. Zin, K. R. McIntosh, and K. Fong. High efficiency silicon solar cells. *Energy Procedia*, 33:1–10, 2013.

[52] M. A. Green. Photovoltaic solar energy conversion. *Brazilian Journal of Physics*, 26(1):137–143, 1996.

[53] C. J. Chen. *Physics of Solar Cells.* John Wiley & Sons, Inc., Hoboken, New Jersey, 2011.

[54] W. Koch, A. L. Endrös, D. Franke, C. Häbler, J. P. Kalejs, and H. J. Möller. *Handbook of Photovoltaic Science and Engineering.* John Wiley & Sons Ltd., Chichester, England, 2003.

[55] M. Kontges, S. Kurtz, C. Packard, U. Jahn, K. A. Berger, K Kato, T. Friesen, H. Liu, and M. Van Iseghen. Review of failure of photovoltaic modules. IEA-PVPS T13-01:2014, International Energy Agency, 2014.

[56] J. Käsewieter, F. Haase, M. H. Larrodé, and M. Köntges. Cracks in solar cell metallization leading to module power loss under mechanical loads. *Energy Procedia*, 55:469–477, 2014.

[57] J. Wendt, M. Trager, M. Mette, A. Pfennig, and B. Jackel. The link between mechanical stress induced by soldering and micro damages in silicon solar cells. In *European Photovoltaic Solar Energy Conference*, pages 3420–3423, 2009.

[58] M. Abdelhamid, R. Singh, and M. Omar. Review of microcrack detection technique for silicon solar cells. *IEEE Journal of Photovoltaics*, 4(1):514–524, 2014.

[59] K. Lin, Y. Lee, W. Huang, G. Chen, Y. Kuo, L. Wang, and S. Yang. Detection of soldering induced damages on crystalline silicon solar modules fabricated by hot-air soldering method. *Renewable Energy*, 83:749–758, 2015.

[60] R. Jonoch, A. Anselmo, and H. Field. Solar panel design factors to reduce the impact of cracked cells and tendency for crack propagation. In *NREL PV Module Reliability Workshop*, pages 1–11, 2015.

[61] M. Sander, S. Dietrich, M. Pander, S. Schweizer, M. Ebert, and J Bagdahn. Investigations on crack development and crack growth in embedded solar cells. *Proc. SPIE 8112, Reliability of Photovoltaic Cells. Modules, Components and Systems IV*, 2011.

[62] J. Barredo, L. Hermanns, A. Fraile, J. C. Jimeno, and E. Alarcon. Study of the edge and surface crack influence in the mechanical strength of silicon wafers. In *European Photovoltaic Solar Energy Conference*, pages 2116–2119, 2009.

[63] S. Kajari-Schröder, I. Kunze, U. Eitner, and M. Köntges. Spatial and orientational distribution of cracks in crystalline photovoltaic modules generated by mechanical load tests. *Solar Energy Materials and Solar Cells*, 95(11):3054–3059, 2011.

[64] Y. Wang, H. Zhao, D. Song, and A. Cai. Research to the typical defects of crystalline silicon photovoltaic cells based on EL images. *International Journal of energy science*, 3(3):200–204, 2013.

[65] J. L. Crozier, E. E. van Dyk, and F. J. Vorster. Characterization of cell mismatch in a multi-crystalline silicon photovoltaic module. *Physica B: Condensed Matter*, 407(10):1578–1581, 2012.

[66] A. Mansouri, M. Zettl, O. Mayer, M. Lynass, M. Bucher, O. Stern, and R. Burhenne. Defect detection in photovoltaic modules using electroluminescence imaging. *European Photovoltaic Solar Energy Conference*, pages 3374–3378, 2012.

[67] J. I. van Mölken, U. A. Yusufoglu, A. Safiei, H. Windgassen, R. Khandelwal, T. M. Pletzer, and H. Kurz. Impact of micro-cracks on the degradation of solar cell performance based on two-diode model parameters. *Energy Procedia*, 27:167–172, 2012.

[68] L. A. Vidhya and K. Vasudevan. Crack detection in solar cell panel using IR reflectance imaging. *International Journal of Innovative Research in Advanced Engineering*, 2(10):84–88, 2015.

[69] T. Wen and C. Yin. Crack detection in photovoltaic cells by interferometric analysis of electronic speckle patterns. *Solar Energy Materials and Solar Cells*, 98:216–223, 2012.

[70] C. L. Zhou, W. J. Wang, H. L. Li, L. Zhao, H. W. Diao, and X. D. Li. Influence of ring oxidation-induced stack faults on efficiency in silicon solar cells. *Chinese Physics Letters*, 25(8):3005–3008, 2008.

[71] J. D. Murphy, R. E. McGuire, K. Bothe, V. V. Voronkov, and R. J. Falster. Minority carrier lifetime in silicon photovoltaics: The effect of oxygen precipitation. *Solar Energy Materials and Solar Cells*, 120:402–411, 2014.

[72] J. Adey, R. Jones, and D. W. Palmer. Degradation of boron-doped czochralski grown silicon solar cells. *Physical Review Letters*, 93(5):1–4, 2004.

[73] H. S. Reehal, M. P. Lesniak, and A. E Hughes. Application of DLTS to silicon solar cell processing. *Journal of Physics D: Applied Physics*, 29:934–938, 1996.

[74] O. von Roos and K. L. Luke. Analysis of the electron beam induced current of a polycrystalline pn junction when the diffusion lengths of the material on either side of a grain boundary differ. *Journal of Applied Physics*, 55(12):4275–4279, 1984.

[75] J. L. Gray. *Handbook of Photovoltaic Science and Engineering*. John Wiley & Sons Ltd., 2003.

[76] H. Y. Zhang, W. G. Wang, H. Liu, R. Wang, Y. M. Chen, and Z. W. Wang. Effects of TiO_2 film thickness on photovoltaic properties of dye-sensitized solar cell and its enhanced performance by graphene combination. *Materials Research Bulletin*, 49:126–131, 2014.

[77] J. Jaus, A. W. Bett, H. Reinecke, and E. R. Weber. Reflective secondary optical elements for fresnel lens based concentrator modules. *Progress in Photovoltaics: Research and Applications*, 19(5):580–590, 2011.

[78] L. Li, D. E. Zhao, D. S. Jiang, Z. S. Liu, P. Chen, L. L. Wu, L. C. Le, H. Wang, and H. Yang. The effects of InGaN layer thickness on the performance of InGaN/p-i-n solar cells. *Chinese Physics B*, 22(6):1–4, 2013.

[79] E. Q. B. Macabebe, C. J. Sheppard, and E. E. van Dyk. Device and performance parameters of $Cu(In,Ga)(Se,S)_2$-based solar cells with varying i-ZnO layer thickness. *Physica B: Condensed Matter*, 404(22):4466–4469, 2009.

[80] C. Tsai. Development of amorphous/microcrystalline silicon tandem thin-film solar modules with low output voltage, high energy yield, low light-induced degradation, and high damp-heat reliability. *Journal of Nanomaterials*, 2014:10, 2014.

[81] A. D. Compaan, I. Matulionis, and S. Nakade. Laser scribing of polycrystalline thin films. *Optics and Lasers in Engineering*, 34(1):15–45, 2000.

[82] R. Crandoll and W. Luft. The future of amorphous silicon technology. Technical report, National Renewable Energy Laboratory, 1995.

[83] B. Burger, K. Keifer, C. Kost, S. Nold, S. Phillipps, R. Preu, T. Schlegl, G. Willeke, H. Wirth, I. Brucker, A. Haberle, V. Schacht, and W. Warmuth. Photovoltaics report. Technical report, Fraunhofer Institute of Solar Energy, 2015.

[84] D. E. Carlson and C. R. Wronski. Amorphous silicon solar cell. *Applied Physics Letters*, 28(11):671–673, 1976.

[85] T. Matsui, A. Bidiville, K. Maejima, H. Sai, T. Koida, T. Suezaki, M. Matsumoto, K. Saito, I. Yoshida, and M. Kondo. High-efficiency amorphous silicon solar cells: Impact of deposition rate on metastability. *Applied Physics Letters*, 106(5):1–5, 2015.

[86] K. Zweibel. Thin Films: Past, Present, Future. *Progress in Photovoltaics: Research and Applications*, 3(5):279–293, 1995.

[87] M. Powalla, G. Voorwinden, D. Hariskos, P. Jackson, and R. Kniese. Highly efficient CIS solar cells and modules made by the co-evaporation process. *Thin Solid Films*, 517(7):2111–2114, 2009.

[88] M. Nakamura, Y. Kouji, Y. Chiba, H. Hakuma, T. Kobayashi, and T. Nakada. Achievement of 19.7 percent efficiency with a small-sized $Cu(InGa)(SeS)_2$ solar cells prepared by sulfurization after selenizaion process with Zn-based buffer. *Photovoltaic Specialists Conference (PVSC), 2013 IEEE 39th*, pages 0849–0852, 2013.

[89] M. Nakamura, N. Yoneyama, K. Horiguchi, Y. Iwata, K. Yamaguchi, H. Sugimoto, and T. Kato. Recent R&D Progress in Solar Frontier's Small-sized $Cu(InGa)(SeS)_2$ Solar Cells. *Photovoltaic Specialist Conference (PVSC), 2014 IEEE 40th*, pages 0107–0110, 2014.

[90] M. A. Green, K. Emery, Y. Hishikawa, W. Warta, and E. D. Dunlop. Solar cell efficiency tables (version 45). *Progress in Photovoltaics: Research and Applications*, 23:1–9, 2015.

[91] M. A. Green, K. Emery, Y. Hishikawa, W. Warta, and E. D. Dunlop. Solar cell efficiency tables (version 47). *Progress in Photovoltaics: Research and Applications*, 24:3–11, 2016.

[92] A. Bonucci, S. Rondena, A. Gallitognotta, P. Gallina, O. Salomon, W. Wischmann, and S. Hiss. Thin-film CIGS PV modules with more than 3000 h damp heat stability: Breakthrough time property of the B-Dry edge sealant and its characterization. *Solar Energy Materials and Solar Cells*, 98:398–403, 2012.

[93] D. J. Coyle. Life prediction for CIGS solar modules part 1: modeling moisture ingress and degradation. *Progress in Photovoltaics: Research and Applications*, 21:150–172, 2013.

[94] F.A. Lindholm, J.G. Fossum, and E.L. Burgess. Application of the superposition principle to solar cell analysis. *IEEE Transactions on Electronic Devices*, 26(3):165–171, 1979.

[95] A. M. Humada, M. Hojabri, S. Mekhilef, and H. M. Hamada. Solar cell parameters extraction based on single and double-diode models: A review. *Renewable and Sustainable Energy Reviews*, 56:494–509, 2016.

[96] A. N. Celik and N. Acikgoz. Modelling and experimental verification of the operating current of monocrystalline photovoltaic modules using four and five parameter models. *Applied Energy*, 84(1):1–15, 2007.

[97] V. Lo Brano, A. Orioli, G. Ciulla, and A. Di Gangi. An improved five parameter model for photovoltaic modules. *Solar Energy Materials and Solar Cells*, 94(8):1358–1370, 2010.

[98] W. Han, H. Wang, and L. Chen. Parameters Identification for Photovoltaic Module Based on an Improved Artificial Fish Swarm Algorithm. *The Scientific World Journal*, pages 1–12, 2014.

[99] M. Haouari-Merbah, M. Belhamel, I. Tobías, and J. M. Ruiz. Extraction and analysis of solar cell parameters from the illuminated current voltage curve. *Solar Energy Materials and Solar Cells*, 87(1-4):225–233, 2005.

[100] A. Q. Malik and S. Damit. Outdoor testing of single crystal silicon solar cells. *Renewable Energy*, 28(8):1433–1445, 2003.

[101] I. M. Mahmoud, S. O. Abdellatif, T. S. Abdel-salam, A. Bayoumi, A. Sahbel, and O. E. Abdellatif. Experimental characterization for a PV module using low cost method. In *Engineering and Technology (ICET), 2014 International Conference on*, pages 1–4, 2014.

[102] C. Salame, G. Khoury, M. Aillerie, A. Sahbel, N. Hassan, M. M. Abdelhameed, and A. Zekry. Experimental performance characterization of photovoltaic modules using DAQ. *Energy Procedia*, 36:323–332, 2013.

[103] E. M. Brito, A. S. Antonio, A. F. Cupertino, and H. A. Pereire. Characterisation of solar panel using capacitive load. *IEEE Journal of Photovoltaics*, pages 1–7, 2014.

[104] PV-Engineering GmbH. *Peak power measuring device and I-V curve tracer for PV modules and generators. Users Manual*, 2014.

[105] Solometric. *Guide to Interpretating I-V curve Measurements of PV Arrays. Application Note PVA-600-1. Retrieved: 27/5/2016 at http//www.resources.solometric/get/Guides to Interpreting I-V Curves.pdf.*

[106] O. Breitenstein, M. Langenkamp, O. Lang, and A. Schirrmacher. Shunts due to laser scribing of solar cells evaluated by highly sensitive lock-in thermography. *Solar Energy Materials and Solar Cells*, 65(1-4):55–62, 2001.

[107] B. Sopori, P. Rupnowski, V. Mehta, V. Budhraja, S. Johnston, N. Call, H. Moutinho, and M. Al-Jassim. Performance limitation of mc-Si solar cells caused by defect

clusters. In *Semicon China*, number NREL/CP-520-45012. National Renewable Energy Laboratory, 2009.

[108] Y. Wang and P. Hsu. An investigation on partial shading of PV modules with different connection configurations of PV cells. *Energy*, 36(5):3069–3078, 2011.

[109] C. Schill, S. Brachmann, and M. Koehl. Impact of soiling on IV-curves and efficiency of PV-modules. *Solar Energy*, 112:259–262, 2015.

[110] T. Fuyuki, H. Kondo, T. Yamazaki, Y. Takahashi, and Y Uraoka. Photographic surveying of minority carrier diffusion length in polycrystalline silicon solar cells by electroluminescence. *Applied Physics Letters*, 86:1–3, 2005.

[111] E.F. Schubert. *Light-Emitting Diodes*. E. Fred Schubert, Second edition, 2006.

[112] T. Potthoff, K. Bothe, U. Eitner, D. Hinken, and M. Köntges. Detection of the voltage distribution in photovoltaic modules by electroluminescence imaging. *Progress in Photovoltaics: Research and Applications*, 18:100–106, 2010.

[113] W. Xiaofeng. *Fast spatially-resolved electrical modelling and quantitative characterisation of photovoltaic devices*. PhD thesis, Loughborough University, 2015.

[114] A. Helbig, T. Kirchartz, R. Schaeffler, J. H. Werner, and U. Rau. Quantitative electroluminescence analysis of resistive losses in cigs thin-film modules. *Solar Energy Materials and Solar Cells*, 94(6):979–984, 2010.

[115] R. Ebner, B. Kubicek, G. Ujvari, and K. Berger. Optical characterisation of different module technologies. *Japanese Journal of Applied Physics*, 54:1–4, 2015.

[116] J. L. Crozier. *Characterisation of performance limiting defects in photovoltaic devices using electroluminescence and related techniques*. PhD thesis, Nelson Mandela Metropolitan University, 2014.

[117] O. Breitenstein, J. P. Rakotoniaina, M. H. Al Rifai, and M Werner. Shunt types in crystalline silicon solar cells. *Progress in Photovoltaics: Research and Applications*, 12:529–538, 2004.

[118] C. S. Solanki. *Solar Photovoltaics: Fundamentals, Technologies and Applications*. PHI Learning Private Limited, Delhi, India, Third edition, 2015.

[119] J. M. Hwang and D. K. Schroder. Recombination properties of oxygen precipitated silicon. *Journal of Applied Physics*, 59(7):2476–2487, 1986.

[120] J. E. Cotter, J. H. Guo, P. J. Cousins, M. D. Abbott, F. W. Chen, and K. C. Fishe. p-Type Versus n-Type Silicon Wafers: Prospects for High-Efficiency Commercial Silicon Solar Cells. *IEEE Transactions on Electron Devices*, 53(8):1893–1901, 2006.

[121] A. Rehman and S. H. Lee. Advancements in n-type base crystalline silicon solar cells and their emergence in the photovoltaic industry. *The Scientific World Journal*, pages 1–13, 2013.

[122] D. Macdonald and L. J. Geerligs. Recombination activity of interstitial iron and other transition metal point defects in p- and n-type crystalline silicon. *Applied Physics Letters*, 85(18):4061–4063, 2004.

[123] S. Martinuzzi and M. Stemmer. Mapping of defects and their recombination strength by a light-beam-induced current in silicon wafers. *Materials Science and Engineering:*, 24(1):152–158, 1994.

[124] S. Chander, A. Purohit, A. Nehra, S. P. Nehra, and M. S. Dhaka. A study on spectral response and external quantum efficiency of mono-crystalline silicon solar cell. *International Journal of Renewable Energy Research*, 5(1):41–44, 2015.

[125] A. K. Sharma, S. K. Agarwal, and S. N. Singh. Determination of front surface recombination velocity of silicon solar cells using the short-wavelength spectral response. *Solar Energy Materials and Solar Cells*, 91(15-16):1515–1520, 2007.

[126] W. Okullo, M. K. Munji, F. J. Vorster, and E. E. van Dyk. Effects of spectral variation on the device performance of copper indium diselenide and multi-crystalline silicon photovoltaic modules. *Solar Energy Materials and Solar Cells*, 95(2):759–764, 2011.

[127] P. Vorasayan, T. R. Betts, A. N. Tiwari, and R. Gottschalg. Multi-laser LBIC system for thin film PV module characterisation. *Solar Energy Materials and Solar Cells*, 93:917–921, 2009.

[128] H. Booth. Laser processing in industrial solar module manufacturing. *Journal of Laser Micro/Nanoengineering*, 5(3):183–191, 2010.

[129] J. J. García-Ballesteros, S. Lauzurica, C. Molpeceres, I. Torres, D. Canteli, and J. J. Gandía. Electrical losses induced by laser scribing during monolithic interconnection of devices based on a-Si:H. *Physics Procedia*, 5, Part A:293–300, 2010.

[130] M. M. Islam, S. Ishizuka, A. Yamada, K. Matsubara, S. Niki, T. Sakurai, and K. Akimoto. Thickness study of Al:ZnO film for application as a window layer in

$Cu(In_{1-x}Ga_x)Se_2$ thin film solar cell. *Applied Surface Science*, 257(9):4026–4030, 2011.

[131] E. L. Meyer and E. E. van Dyk. Characterization of degradation in thin-film photovoltaic module performance parameters. *Renewable Energy*, 28(9):1455–1469, 2003.

[132] C. Honsberg and S. Bowden. *PVCDROM, Retrieved: 6/1/2016 at http://www.pveducation.org/pvcdrom/pn-junction/absorption-coefficient*.

[133] L. M. Edson and E. E. van Dyk. The effect of reduced shunt resistance and shading on photovoltaic module performance. In *31st IEEE Photovoltaics Specialists Conference*, pages 1–4, 2005.

[134] S. M. Ali, A. Pradhan, P. K. Dash, and B. K. Rao. Analysis of colour spectrum on the performance of photovoltaic cell. *International Journal of Renewable Energy*, 8(1):26–30, 2013.

[135] A. S. Blazev. *Photovoltaics for Commercial and Utilities Power Generation*. The Fairmont Press, Inc. Lilburn, Georgia, 2012.

[136] Z. Xing, R. Jia, W. Ding, Y. Meng, Z. Jin, and X. Liu. Improving poor fill factors for solar cells via light-induced plating. *Journal of Semiconductors*, 33(9):1–4, 2012.

[137] C. Honsberg and S. Bowden. *PVCDPVC, Retrieved: 12/6/2015, at http://www.pveducation.org/pvcdrom/solar-cell-operation/series-resistance*.

[138] W. Herrmann, W. Wiesner, and W. Vaassen. Hot spot investigations on PV modules new concepts for a test standard and consequences for module design with respect to bypass diodes. In *Conference Record of the Twenty Sixth IEEE Photovoltaic Specialists Conference*, pages 1129–1132, 1997.

[139] M. A. Green, K. Emery, Y. Hishikawa, W. Warta, and E. D. Dunlop. Solar cell efficiency tables (version 48). *Progress in Photovoltaics: Research and Applications*, 24(7):905–913, 2016.

[140] S. Phillipps, A. W. Bett, K. Horowitz, and S. Kurtz. Current status of concentrator photovoltaic (CPV) technology. *Fraunhofer ISE and NREL*, pages 1–26, 2016.

[141] W. J. Smith. *Modern Optical Engineering*. McGraw-Hill, New York, U.S.A., Third edition, 2000.

[142] I. Wallhead, T. M. Jimenez, J. V. G. Ortiz, I. G. Toledo, and C. G. Toledo. Design of an efficient Fresnel-type lens utilising double total internal reflection for solar energy collection. *Optics Express*, 20(S6):A1005–A1010, 2012.

[143] T. Hornung and P. Nitz. Light diffraction by concentrator Fresnel lenses. *Optics Express*, 22:A686–A704, 2014.

[144] T. Hornung and P. Nitz. Optical loss due to diffraction by concentrator Fresnel lenses. *AIP Conference Proceedings*, 1616(63):63–66, 2014.

[145] A. Nayak, G. S. Kinsey, M. Liu, W. Bagienski, and V. Garboushian. Comparison of primary optics in amonix CPV arrays. *AIP Conference Proceedings*, 1477(1):77–80, 2012.

APPENDIX A

A.1 Publications

M. Okullo, F. J. Vorster, E. E. van Dyk and J. L. Crozier. Analysis of homogeneity in thin film photovoltaic modules using large area light beam induced current (LA-LBIC) measurements, in: South African Institute of Physics, 2015, pp. 463-468

A.2 Conference and Workshop attended

60^{th} Annual Conference of South African Institute of Physics, Boardwalk Convention Centre, Port Elizabeth, "Analysis of homogeneity in thin film photovoltaic modules using large area light beam induced current (LA-LBIC) measurements", 29 June - 3 July 2015

8^{th} African Laser Centre Student Workshop, Zevenwacht, Stellenbosch, RSA, "Characterisation of thin film photovoltaic modules using large area light beam induced current measurements", 2 - 6 December 2015

APPENDIX B

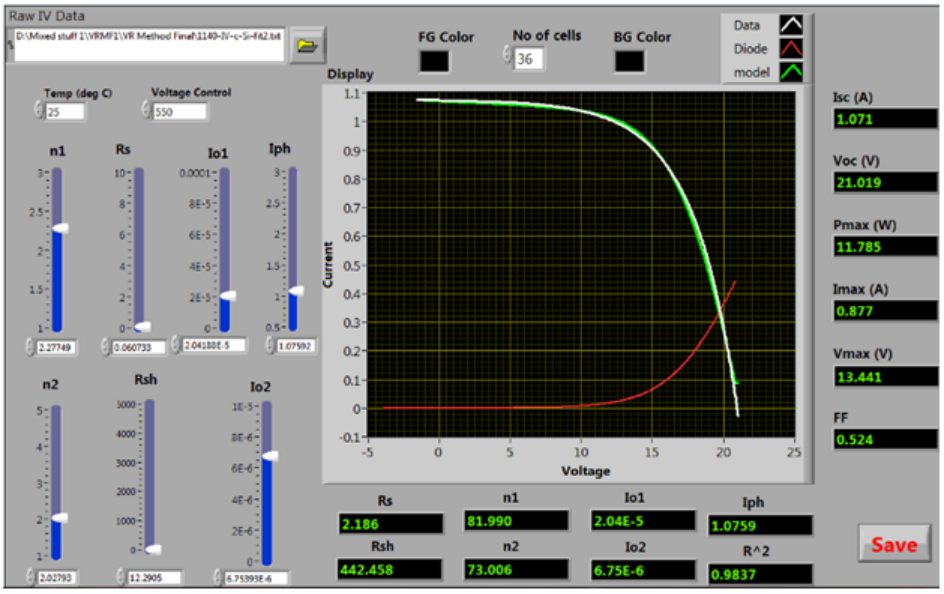

Figure 8.1: User interface Labview front panel screenshot for I-V curve fitting

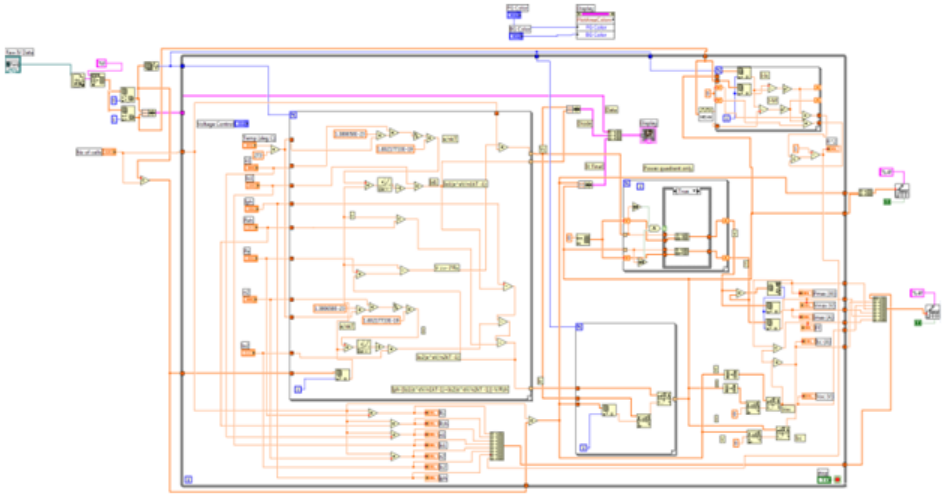

Figure 8.2: User interface Labview block diagram screenshot for I-V curve fitting